



U N I V E R S I T Y   O F  

---

L I V E R P O O L

# **THE LOW VELOCITY IMPACT RESPONSE OF SANDWICH STRUCTURES**

Thesis submitted in accordance with the requirement of

The University *of* Liverpool for the degree of

Doctor in Philosophy by

**Mohamad Zaki Hassan**

School of Engineering

September 2012

## ACKNOWLEDGEMENTS

I would especially like to take this opportunity to acknowledge the invaluable assistance of my supervisor Professor W.J Cantwell for the patient guidance, encouragement and advise throughout my PhD studies. I have been extremely lucky to have a supervisor who cared so much about my work.

I am deeply indebted to the following institutions; the Ministry of Higher Education of Malaysia and Universiti Teknologi Malaysia for give me the fund for my study. I am also would like to express my gratitude to all the staff in the Department of Engineering who provided me with assistance with samples preparation and testing, especially Mr Stephen Pennington, Mr Jijimon Mathew and Mr Dave Atkinson.

I would like to extend my thanks to all my colleagues in the Composite Group for their encouragement, support and friendship.

A special thanks is also dedicated to my wife, Zarini, for her patience and support throughout the project until completion of this thesis. My love and thanks also goes to my children, Noralyaa and Alif who give me strength and courage to go on. Lastly but not the least, I owe deep gratitude towards my family especially my beloved mum, dad and grandmother for their endless support, patience and encouragement throughout this research work. To my mum, this thesis is truly a present for you for bringing me up and who made me what I am today. Not to forget, my appreciation goes to all my family members.

## LIST OF PUBLICATIONS

1. Hassan MZ, Cantwell WJ. An investigation into the fracture properties of all-polypropylene sandwich structures. In: Torre L, editor. SEICO 09 Conférence de SAMPE Europe; Paris Porte de Versailles 2009.
2. Hassan MZ, Cantwell WJ. The impact response of fully-recyclable sandwich structures. In: Beral B, editor. SEICO 10 Conférence de SAMPE Europe; Paris Porte de Versailles 2010.
3. Hassan MZ, Cantwell WJ. Strain rate effects in the mechanical properties of polymer foams. *International Journal of Polymers and Technologies*. 2011;3(1):27-34.
4. Hassan MZ, Cantwell WJ. Strain rate effects in the indentation behavior of foam-based sandwich structures. *Journal of Composite Materials*. 2012;46(10):1191-9.
5. Zhou J, Hassan MZ, Guan Z, Cantwell WJ. The low velocity impact response of foam-based sandwich panels. *Composites Science and Technology*. 2012;72(14):1781-90
6. Hassan MZ, Cantwell WJ. The influence of core properties on the perforation resistance of sandwich structures – An experimental study. *Composites Part B: Engineering*. 2012 (In Press, Accepted Manuscript).
7. Hassan MZ, Guan ZW, Cantwell WJ, Langdon GS, Nurick GN. The influence of core density on the blast resistance of foam-based sandwich structures. *International Journal of Impact Engineering*. 2012 (In Press, Accepted Manuscript).
8. Yang FJ, Hassan MZ, Cantwell WJ, Jones N. Scaling effects in the low velocity impact response of sandwich structures. *Composite Structures*. 2012 (In Press, Accepted Manuscript).

9. Langdon GS, Hassan MZ, Cantwell WJ, Nurick GN. Response of blast loaded foam core sandwich panels. In: Ferreira A, editor. International Conference on Mechanics of Nano, Micro and Macro Composite Structures Politecnico di Torino Italy 2012.
10. Hassan MZ, Cantwell WJ. The impact response of environmentally-friendly sandwich structures. To be published in the Journal Composite Materials.

## ABSTRACT

In this study, the mechanical properties and fracture behaviour of a range of core materials have been investigated in order to elucidate the impact properties of sandwich structures. Initially, the compression properties of the core have been evaluated at quasi-static and impact rates of strain. It has been shown that the plastic collapse strength of the cores is highly rate-sensitive, increasing by up to one hundred percent in passing from quasi-static to dynamic rates of loading. Subsequently, the SENB (Mode I) and shear (Mode II) fracture properties of the polymer foams were evaluated. Mode I tests have shown that the crosslinked PVC foams and the PET foams fail in a brittle manner, however, the linear PVC foams fail in a ductile mode. Here, it has been shown that the Mode II shear toughnesses of the crosslinked PVC foams were up to thirty-five times greater than their corresponding Mode I values. Following this, a series of indentation tests were conducted on polymer-foam sandwich structures and their response was characterised using a Meyer indentation law of the form  $P = C\alpha^n$ . It has been shown that the value of the exponent parameter,  $n$ , does not vary significantly with the properties of the core or the skin, typically being close to unity for all tests. The contact stiffness,  $C$ , was found to depend on the plastic collapse strength of the foam, the indenter radius and the properties of the skin. It has been shown that a plot of contact stiffness against plastic collapse strength, containing all of the quasi-static and dynamic data, appears to yield a unique curve. Subsequently, the perforation resistances of a range of foam-based sandwich structures were investigated. The influence of the plastic collapse stress of the foam in determining the failure thresholds of the front and rear composite skins has been established. Here, a simple model has been used to successfully predict failure of the top surface composite skin in the sandwich structures. In addition, the force associated with perforating the lightweight core has been shown to be strongly dependent on the shear strength of the polymer foam.

The perforation response of sandwich structures based on fully-recyclable materials has also been investigated. The design of the SRPP skin has a significant effect on the energy-absorbing characteristics of the sandwich structure, with the performance of systems based on multiple layer skins greatly exceeding that associated with a monolithic skin. It has been shown that when normalised by the areal density of the panels, those sandwich structures with multiple layer skins out-perform systems with monolithic skins as well as conventional GFRP/aluminium honeycomb sandwich structures.

## TABLE OF CONTENTS

Title Page	i
Acknowledgement	ii
List of Publications	iii
Abstract	v
Table of Contents	vi
List of Figures	xiv
List of Tables	xxvii

### CHAPTER I INTRODUCTION

1.1	Preface	2
1.2	Fibre-reinforced Polymer (FRP)	3
1.2.1	Glass Fibres	4
1.2.2	Carbon Fibres	5
1.2.3	Boron Fibres	6
1.2.4	Aramid Fibres	6
1.3	Matrices	8
1.3.1	Thermosetting Resins	9
1.3.2	Thermoplastic Resins	9
1.4	Interface	11
1.5	Sandwich Structures	11
1.5.1	Skin Materials	12

1.5.2.	Core Materials	12
1.5.2.1	Polymer Foam	13
1.5.2.2	Honeycomb Cores	15
1.5.2.3	Corrugated Cores	15
1.6	Adhesive	16
1.7	Composites Applications	17
1.8	Major Contribution of Thesis	22
1.9	Thesis Organisation	23
1.10	References	24

## **CHAPTER II LITERATURE REVIEW**

2.1	Classification of Impact Response	27
2.2	Contact Mechanics	29
2.2.1	Indentation of Composite Laminates	30
2.2.2	Indentation Response of Sandwich Structures	33
2.3	Low Velocity Impact Response of Composite Laminate	35
2.3.1	Effect of Impactor Diameter and Geometry	36
2.3.2	The Effect of Impact Velocity	37
2.3.3	Effect of Loading Rate on the Fracture Toughness of Composite Laminates	38

2.3.4	Effect of Specimen Thickness	45
2.3.5	Influence of Constituents of the Composite Laminate	47
2.3.5.1	The Effect of Fibre Properties	47
2.3.5.2	The Effect of Matrix Properties	50
2.3.5.3	The Effect of Fibre-Matrix Interface	53
2.4	Failure Modes in Composite Laminates Subjected to Low Velocity Impact	55
2.4.1	Matrix Damage	55
2.4.2	Delamination	56
2.4.3	Fibre Failure	59
2.5	Low Velocity Impact Response of Sandwich Structures	60
2.5.1	Effect of Impactor Geometry	60
2.5.2	Effect of Impact Velocity	61
2.5.3	Effect of Skin Type, Thickness and Stacking Sequence	62
2.5.4	Effect of the Core	65
2.6	Failure Modes in Sandwich Structures	66
2.7	The Analytical Perforation Model	70
2.8	Summary	72

## **CHAPTER III                      EXPERIMENTAL PROCEDURE**

3.1	The Core Materials	89
-----	--------------------	----



3.1.1	Polypropylene (PP) Honeycomb	89
3.1.2	Corrugated Paperboard	89
3.1.3	Polymer Foam	90
3.1.3.1	Crosslinked (H 130) and linear (HD 130) PVC Foams	90
3.1.3.2	Linear-styreneacrylonitrile (SAN) Foam	90
3.1.3.3	Polymethacrylimide (PMI) Foam	91
3.1.3.4	Crosslinked PVC (C70) Foams	92
3.1.3.5	Linear PVC (R63) Foams	92
3.1.3.6	Polyethyleneterephthalate (T92) Foams	94
3.2	The Skin Materials	94
3.2.1	Glass Fibre Reinforced Epoxy (GFRP)	95
3.2.2	Self-reinforced Polypropylene (SRPP) (Curv)	95
3.2.3	Woven Glass Fibre-Reinforced Polymer (GFRP)	95
3.2.4	Woven Glass Fibre-reinforced Polyamide 6,6 (GFPA)	95
3.3	Manufacture of the Sandwich Structures	96
3.3.1	Manufacture of Honeycomb and Corrugated Paperboard Sandwich Structures	96
3.3.2	Manufacture of Polymer-foam Based Sandwich Structures	97
3.4	Determination of the Mechanical Properties of the Composites	99
3.4.1	Compression Tests	99

3.4.1.1	Quasi-static Compression Testing	99
3.4.1.2	Dynamic Compression Testing	100
3.4.2	Single End Notch Bend Test (SENB)	101
3.4.2.1	Quasi-static SENB Tests	101
3.4.2.2	Dynamic Single End Notch Bending Tests	102
3.4.3	Mode II (Shear) Test	103
3.4.4	Indentation Test	104
3.4.4.1	Quasi-static Indentation Tests	104
3.4.4.2	Dynamic Indentation Tests	106
3.4.5	Low Velocity Impact Testing	107
3.5	References	110

## **CHAPTER IV                      MECHANICAL BEHAVIOUR OF THE CORE**

4.1	Compression Tests	112
4.1.1	The Quasi-static Compressive Behaviour of the Cores	112
4.1.1.1	Compression Behaviour of the Crosslinked PVC (C70), Linear PVC (R63) and PET (T92) Foams	112
4.1.1.2	Compression Behaviour of the Linear PVC (HD 130), Crosslinked PVC (H 130), SAN (A500) and PMI (WF 71) Foams	122

4.1.1.3	Compression Behaviour of the PP Honeycomb, the Paperboard and the Aluminium Honeycomb Sandwich Structures	123
4.1.2	The Compression Behaviour of the Foams at Higher Strain Rates	126
4.3	Single End Notch Bend Test – Mode I	130
4.3.1	The Effect of Foam Density on the Toughness of the Foams	131
4.3.2	The Effect of Crosslinking on Foam Toughness	134
4.3.3	The Effect of Loading Rate on the Toughness	135
4.4	Shear Tests – Mode II	142
4.4.1	The Effect of Foam Density of the Mode II Work of Fracture Properties	143
4.4.2	The Effect of Crosslinking on the Mode II Properties of The Foams	144
4.5	Relationship between the Mode I and Mode II Toughness	146
4.6	Conclusions	148
4.6	References	149

## **CHAPTER V    LOW VELOCITY IMPACT TEST ON SANDWICH STRUCTURES**

5.1	Indentation Testing	152
5.1.1	Quasi-static and Dynamic Indentation Tests on the Sandwich Structures	152

5.1.2	The Effect of Loading Rate on the Indentation Response of the Sandwich Structures	154
5.1.3	The Effect of Indentor Diameter on Indentation Response of the Sandwich Structures	159
5.1.4	The Effect of Skin Thickness on Indentation Behaviour	161
5.2	Perforation Resistance of the Sandwich Structures	163
5.2.1	Perforation Properties of the Plain Foams	163
5.2.2	Impact Perforation of Sandwich Structures	170
5.2.2.1	Perforation Behaviour of the Sandwich Structures	170
5.2.2.2	Failure of the Core	178
5.2.2.3	Failure of the Lower Skin	178
5.2.2.4	Perforation of the Sandwich Structures	182
5.3	Impact Response of the Fully Recyclable Sandwich Structures	185
5.3.1	Skin Configuration and Thickness	189
5.3.2	Effect of the Skin on the Impact Response of the Paperboard Core Sandwich Structures	194
5.3.3	Specific Perforation Energy of Sandwich Structures	197
5.4	Conclusions	198
5.5	References	200

## **CHAPTER VI CONCLUSIONS**

6.1	Mechanical Properties of Polymer Foams	203
6.2	Indentation Behaviour of Foam-based Sandwich Structures	204
6.3	Perforation Resistance of the Composite Structures	205
6.4	Suggestions for Further Work	206

## LIST OF FIGURES

Figure 1.1	Classification of composite material systems.	3
Figure 1.2	Stress-strain curves for some typical fibres.	8
Figure 1.3	Variation of delaminated area following drop-weight impact on carbon/epoxy and carbon/PEEK laminates with a $[\pm 45, 0_3, \pm 45, 0_2]_s$ lay-up.	10
Figure 1.4	Typical types of sandwich constructions.	12
Figure 1.5	Typical stress strain curve for PMI foam.	14
Figure 1.6	Typical stress-time history of the CFRP corrugated core at a different impact velocities.	16
Figure 1.7	Composite applications on the Dreamliner 787.	19
Figure 1.8	The growth of composite structures in major aircraft programs (1975-2010) as a percentage of weight.	19
Figure 1.9	Prototype of a BMW engine mounting bracket manufactured by LKR Ranshofen (Austria).  From left to right: empty casting, entire composite part consisting of aluminium foam core and cast shell, section through composite part.	20
Figure 1.10	Crash energy absorber made from rubber, polymer	

	and aluminium foam for a tram built for the Combino vehicle system.	21
Figure 2.1	Comparison between boundary-controlled and wave-controlled impact.	29
Figure 2.2	The variation of the power law contact stiffness with indenter radius following quasi-static indentation tests.	32
Figure 2.3	Typical load-displacement traces following quasi-static and impact tests on cross-ply glass/epoxy laminates.	32
Figure 2.4	The variation of the indentation parameter with the crosshead displacement rate.	35
Figure 2.5	Comparison of Mode I interlaminar fracture toughness data as a function of strain rate.	39
Figure 2.6	Rate dependence of Mode I interlaminar fracture toughness for two carbon fibre/epoxy composites.	40
Figure 2.7	Influence of the loading rate on the crack-initiation values of $G_{Ic}$ .	40
Figure 2.8	Summary of the variation of the Mode II fracture toughness with strain rate for carbon/epoxy and carbon/PEEK laminates.	42
Figure 2.9	The variation of $G_{IIc}$ with crosshead displacement rate for tests at temperatures between 20 and 150°C.	43
Figure 2.10	Comparison of the published data for the Mode II interlaminar fracture toughness of carbon /PEEK laminates as a	

	function of the reduced displacement rate.	44
Figure 2.11	Strain rate effects on Mode II fracture toughness.	45
Figure 2.12	Schematic diagram of damage progression for a) thin and b) thick CRFP laminates.	46
Figure 2.13	Development of damage as a function of impact energy for two ( $\pm 45^\circ$ ) of CFRP laminates.	47
Figure 2.14	The variation of residual compression strength after impact with impact energy following low velocity impact tests.	51
Figure 2.15	The variation of impact damage area with incident impact energy for carbon/PEEK and carbon/PPS laminates.	52
Figure 2.16	Transverse section of a carbon/epoxy.	55
Figure 2.17	Variation of the first damage threshold with beam length for (0% $\pm 45^\circ$ ) CFRP laminates.	56
Figure 2.18	Delamination patterns through the thickness of a carbon/epoxy laminate following low velocity impact loading.	57
Figure 2.19	The variation of damage area with impact energy for honeycomb core sandwich structure (a) carbon/epoxy and glass/epoxy skins with incident impact energy.	62
Figure 2.20	Load versus indenter displacement for specimens having different skin thicknesses, all of these specimens had	



	25 mm thick PVC foam cores.	63
Figure 2.21	Summary of the variation of the maximum peak load with impact energy for four sandwich structures.	64
Figure 2.22	Damage progression in PVC core sandwich structures following three point bend testing with (a) varying skin thickness and (b) varying core density.	67
Figure 2.23	Typical load-displacement traces for aluminium honeycomb sandwich structures following quasi-static loading.	68
Figure 2.24	Three-stage perforation process in a honeycomb sandwich panel.	69
Figure 3.1	The Meyer hot press used for manufacturing the composite skins.	97
Figure 3.2	Schematic of the stacking sequence for a 4-ply of unidirectional GFRP composite.	98
Figure 3.3	Photo of the dynamic compression test geometry.	101
Figure 3.4	Schematic diagram of the quasi-static SENB test geometry.	102
Figure 3.5	Schematic diagram of the dynamic SENB test geometry.	103
Figure 3.6	(a) Schematic diagram and (b) photo of the Mode II test geometry.	104
Figure 3.7	Photo of the hemispherical indentors used during the indentation test.	105
Figure 3.8	Schematic diagram of the indentation test.	105
Figure 3.9	Typical plot of $\log P$ versus $\log \alpha$ for the indentation tests.	106
Figure 3.10	Photo of the dynamic indentation test.	107

Figure 3.11	The low velocity impact tower.	108
Figure 3.12	The high speed video camera set-up used for drop-weight impact testing.	109
Figure 4.1	A typical stress-strain trace following quasi-static testing on a crosslinked PVC C70.90 foam.	113
Figure 4.2	Energy absorption efficiency-strain plot following quasi-static tests on a crosslinked PVC C70.90 foam.	114
Figure 4.3	Typical stress-strain traces following quasi-static tests on the crosslinked PVC foams (C70.55), (C70.75), (C70.90), (C70.130) and (C70.200).	116
Figure 4.4	Photos of the surfaces of typical crosslinked PVC (C75 55), (C70.90) and (C70.200) foams.	117
Figure 4.5	Typical stress-strain curves following quasi-static tests on the linear PVC R63.80 and R63.140 foams.	118
Figure 4.6	Typical stress-strain plots following quasi-static tests on the PET T92.100 and PET T92.130 foams.	119
Figure 4.7	The variation of plastic collapse stress with density for different foams.	120
Figure 4.8	The variation of compressive modulus with density for different foams.	120
Figure 4.9	The variation of steady state stress with density for different foams.	121
Figure 4.10	Typical stress-strain plots following quasi-static tests	

	on a crosslinked (H 130), a linear (HD 130), a SAN (A500) and a	
	PMI (WF 71) foams.	122
Figure 4.11	Quasi-static compression tests on the 44 and 86 kg/m <sup>3</sup>	
	PP honeycombs and the 88 kg/m <sup>3</sup> paperboard.	123
Figure 4.12	A compressive stress-strain curve for an aluminium	
	honeycomb sandwich structure.	125
Figure 4.13	Dynamic and quasi-static stress-strain curves for the	
	(a) crosslinked PVC C70.90 and (b) linear PVC R63.80 foams.	127
Figure 4.14	Typical load-displacement traces for corrugated paperboard	
	following dynamic and quasi-static tests.	128
Figure 4.15	Summary of the quasi-static and dynamic plastic collapse	
	stress values of (a) the crosslinked PVC (C70), the linear	
	PVC (R63) and the PET (T92) and (b) the SAN (A500), the linear	
	PVC (H 130), the crosslinked PVC (HD 130) foams, the 40 and	
	80 kg/m <sup>3</sup> PP honeycomb and the paperboard.	130
Figure 4.16	Typical load-displacement traces following Mode I SENB	
	test on crosslinked PVC (a) C70.200 and C70.90 (b) C70.55, C70.75	
	and C70.130 foams.	132
Figure 4.17	Typical load-displacement traces following Mode I SENB tests on	
	the PET T92.100 and T92.130 foams.	133

Figure 4.18	Summary of foam density on the work of fracture of the crosslinked PVC, the linear PVC and the PET foams.	134
Figure 4.19	Typical load-displacement traces following Mode I SENB tests on the crosslinked PVC C70.90 and the linear PVC R63.80 foams.	135
Figure 4.20	Typical load displacement traces following Mode I testing of the linear PVC foam (R63.140).	135
Figure 4.21	Typical load displacement traces following Mode I testing of the crosslinked PVC (C70.75) and PET (T92.130) foams.	137
Figure 4.22	Photos of typical failed SENB samples following quasi-static testing on the (a) 130 kg/m <sup>3</sup> crosslinked PVC, (c) 135 kg/m <sup>3</sup> PET, (e) 140 kg/m <sup>3</sup> linear PVC foams and dynamic testing on the (b) 130 kg/m <sup>3</sup> crosslinked PVC, (d) 135 kg/m <sup>3</sup> PET (f) 140 kg/m <sup>3</sup> linear PVC foams.	139
Figure 4.23	Mode I work of fracture values for the linear and crosslinked PVC foams as well as the PET tested in quasi-static and dynamic loading.	140
Figure 4.24	Comparison of the measured work of fracture values of the foams with published data.	141
Figure 4.25	Typical load-displacement traces following Mode II SENB tests on (a) the crosslinked C70.200, C70.130,	

	C70.55 PVC foams and (b) the T92.130, T92.100 PET foams.	144
Figure 4.26	Typical load-displacement traces following Mode II tests on the crosslinked PVC C70.90 and the linear PVC R63.80 foams.	145
Figure 4.27	Side views of (a) the linear PVC R63.80 and (b) the crosslinked PVC C70.90 foams following Mode II testing.	146
Figure 4.28	Summary of the variation work of fracture (Mode II) with density for the crosslinked PVC, linear PVC and PET foams.	147
Figure 4.29	Comparison of the Mode II work of fracture values of the foams with their corresponding Mode I values.	148
Figure 5.1	Quasi-static and impact force-indentation curves for (a) the linear PVC foam R63.80 (b) the crosslinked PVC foam C70.130. The diameter of the indenter was 10 mm.	153
Figure 5.2	A plot of $\log P$ versus $\log \alpha$ showing the curve-fitting method for calculating indentation constants $n$ and $C$ for the GFPA sandwich structure based on C70.130 foam. The test was undertaken at 1 mm/min.	155
Figure 5.3	Comparison of the quasi-static and dynamic values of the indentation exponent parameter ' $n$ '. The indenter diameter was 10 mm.	155

Figure 5.4	Comparison of the quasi-static and dynamic values of the contact stiffness parameter 'C'. The indenter diameter was 10 mm.	156
Figure 5.5	The variation of the contact stiffness with the plastic yield stress for the quasi-static and impact tests.	157
Figure 5.6	The variation of 'C' with plastic collapse stress for the sandwich structures with foam cores (SAN A500, crosslinked H 130 and crosslinked C70.130) and glass fibre/epoxy skins. The tests were conducted at quasi-static (closed triangles) and dynamic (open triangles) rates of strain. The data from the tests on the glass/nylon sandwich structures (circles) are included for comparison.	158
Figure 5.7	Summary of indentation coefficient values as a function of indenter diameter for the six foams.	159
Figure 5.8	Summary of contact stiffness values as a function of indenter diameter for sandwich structures based on the six foams.	160
Figure 5.9	The variation of the contact stiffness with the square root of the indenter radius for six different sandwich structures.	161
Figure 5.10	The influence of skin thickness on the indentation constant of the C70.130 and A500 sandwich structures. The 0/90 laminates are based on GFRP skins and the woven	

	laminate refers to the GFPA skin.	162
Figure 5.11	Typical load-displacement histories following drop-weight impact test on the plain crosslinked PVC foams.	164
Figure 5.12	Typical load-displacement histories following drop-weight impact test on the plain linear PVC foams.	165
Figure 5.13	Typical load-displacement curves following drop-weight impact tests on the PET foams.	166
Figure 5.14	Cross-sections of the perforated, (a) from top to bottom crosslinked PVC (C70.55), (C70.75), (C70.90), (C70.130), (C70.200) and (b) linear PVC (R63.80), (R63.140) (c) PET (T92.100), (T92.130) foams.	167
Figure 5.15	Summary of the perforation energy of the plain cores as a function of core density.	168
Figure 5.16	Summary of the average perforation force of the plain core as a function of shear stress strength of the foam.	169
Figure 5.17	Typical load displacement histories following drop-weight impact test on the sandwich structures based on crosslinked PVC (a) (C70.130) and (C70.200) (b) (C70.55), (C70.75) and (C70.90) foams.	172
Figure 5.18	Typical load displacement histories following drop-weight	

	impact test on the sandwich structures of (a) the linear PVC	
	and (b) the PET foams.	173
Figure 5.19	Cross-sections of the perforated sandwich panels:  (a) Crosslinked PVC (C70.55), (b) Crosslinked PVC (C70.130),  (c) Crosslinked PVC (C70.200), (d) Linear PVC (R63.140),  (e) PET (T92.100) foams.	175
Figure 5.20	The variation of the force required to fracture the top skin  as a function of dynamic plastic collapse stress of the foam core.	177
Figure 5.21	The variation of the force required to fracture the top skin  as a function of dynamic plastic collapse stress of the foam  core for sandwich fully-supported on a steel base.  The data from Figure 5.21 are included for comparison.	178
Figure 5.22	Plot of the measured perforation force during core failure against  the predicted value. The figure includes the data for the  sandwich structures based on both 0.25 and 0.5 mm thick skins.	180
Figure 5.23	The variation of the force required to fracture the lower  skin as a function of the plastic collapse stress of the foam core.	181
Figure 5.24	The variation of the perforation energy of the sandwich  structure as a function of the Mode II (shear) work of fracture.	184
Figure 5.25	Load-displacement traces following impact on (a) the 0.66 mm	



	multiple-layer SRPP-PP honeycomb sandwich structure	
	and (b) the 0.6 mm GFRP/aluminium honeycomb structure.	186
Figure 5.26	Cross-section of the sandwich structures following impact	
	(a) 0.66 mm multi-layers (b) 1.02 mm multi-layers	
	(c) 3 mm monolithic SRPP skins-PP honeycomb sandwich structures	
	(d) 0.6 mm GFRP/aluminium honeycomb structure.	188
Figure 5.27	The variation of perforation energy with skin thickness	
	for PP sandwich structures based on multi-layer skins	
	and cores of density 44 and 86 kg/m <sup>3</sup> . The figure includes	
	the data point for the aluminium sandwich structure.	189
Figure 5.28	The variation of perforation energy with skin thickness for	
	sandwich structures based on both multi-layers and	
	monolithic skins.	190
Figure 5.29	Typical load-displacement traces for panels based on	
	(a) multi-layers and (b) monolithic skins.	191
Figure 5.30	The variation of perforation energy with composite thickness	
	for panels based on multi-layers and monolithic skins.	192
Figure 5.31	Typical perforation zone in 0.9 mm thick (a) monolithic skin	
	and (b) multiple- layer skin.	193
Figure 5.32	Load-displacement traces following low velocity impact	

	on the paperboard sandwich structures based on monolithic SRPP skins.	194
Figure 5.33	The variation of perforation energy with skin thickness for PP honeycomb and paperboard sandwich structures based on monolithic skins. The figure includes the value for the aluminium sandwich structure.	195
Figure 5.34	Cross-sections of sandwich structures following impact on panels based on 0.9 mm monolithic SRPP skins with (a) a PP honeycomb and (b) a paperboard cores.	196
Figure 5.35	Variation of the specific perforation energy with skin thickness for monolithic SRPP-(paperboard and PP honeycomb), multiple SRPP-PP honeycomb (44 and 86 kg/m <sup>3</sup> ) and GFRP/aluminium honeycomb sandwich structures.	197

## LIST OF TABLES

Table 1.1	Typical mechanical properties of glass fibres.	4
Table 1.2	Typical mechanical properties of unidirectional carbon fibre properties.	5
Table 1.3	Typical mechanical properties of boron fibres.	6
Table 1.4	Typical mechanical properties of the Kevlar, the Nomex and Twaron fibres.	7
Table 2.1	The effect of matrix on the interlaminar fracture toughness and specific energy absorption of carbon/PAS, carbon/PI, carbon/PEI and carbon/PEEK.	52
Table 2.2	The effect of the stacking sequence of glass/epoxy and carbon/epoxy laminates on the delamination initiation load.	58
Table 2.3	The effect of thickness and stacking sequence on the load to introduce fibre failure in carbon/epoxy laminates.	59
Table 3.1	Summary of the mechanical properties of the corrugated cardboard.	89
Table 3.2	Summary of the properties of the linear PVC (HD 130) and crosslinked PVC (H 130) foams investigated in this study.	90
Table 3.3	Summary of the mechanical properties of the A500 foam.	91
Table 3.4	Summary of mechanical properties of the	

	polymethacrylimide (WF-71) foam.	92
Table 3.5	Material properties of the crosslinked PVC (C70) and linear PVC (R63) foams.	93
Table 3.6	Properties of the PET foams investigated in this study.	94
Table 3.7	Summary of the mechanical properties of the composite skins	96
Table 3.8	Summary of the configurations and thicknesses of the unidirectional and woven GFRP skins.	99
Table 4.1	Average mechanical properties of the crosslinked (C70), linear (R63) and PET (T92) foams.	115
Table 4.2	Summary of the average mechanical properties of the linear HD 130, the crosslinked H 130, the A500 and the WF 71 foams.	123
Table 4.3	Summary of the average mechanical properties of the 40 and 80 kg/m <sup>3</sup> PP honeycomb, the paperboard and the aluminium honeycomb sandwich structures.	125
Table 4.4	Comparison of the fracture properties for various foams.	142
Table 5.1	Summary of the fracture properties and perforation energies of the nine foams tested in this study.	183

## **CHAPTER I**

### **INTRODUCTION**

---

This chapter presents an overview of polymer composite materials and a brief summary of the fibres, matrices and interfaces used in the production of composite laminates. Following this, details of sandwich constructions based on polymer composites will be presented. Finally, the applications of the composites and sandwich structures will be outlined.

## 1.1 Preface

Composite materials consist of two or more distinct materials bonded to each other with significantly different physical or chemical properties in order to form a new material utilising the properties of each constituent for structural improvement. Composite materials are used not only for their structural properties, but also in electrical, insulation, thermal and environmental applications. The advantages demonstrated by composites are a high stiffness and strength to weight ratio, a low density, corrosion and thermal resistance and the ability to form complex shapes, making them potential candidates for many applications. In recent year, composite materials have been increasing replacing conventional metallic materials in the aerospace, marine, automotive and civil industries.

Composites are commonly classified into two distinct levels (1). The first level of classification is usually made with respect to the matrix constituent. The major composite classes include polymer-matrix, metal-matrix, ceramic-matrix and carbon-carbon matrix composites. The second level of classification refers to the reinforcement used: particulate reinforcements, discontinuous reinforcements, continuous fibres and woven composites (braided and knitted fibres are included in this category) as illustrated in **Figure 1.1** (2).

**Particulate-reinforced** composites include those reinforced by spheres, flakes or many other shapes with roughly the same size and dimensions. **Discontinuous composite** consist of randomly oriented of fibre, typically used in metal-matrix composites for control of shrinkage, increased thermal or electrical conductivity (1). **Continuous fibre-reinforced composites** contain reinforcement having lengths much greater than their cross sectional dimensions. Each ply of continuous fibre typically has a specific fibre orientation, **Figure 1.1**. The final category to consider is that of **weaving and braiding**. Here, the fibre bundles or tows create interlocking fibres that often have an orientation orthogonal to the primary structural plane.

The composite's properties are mainly influenced by the choices of fibre orientations, stacking sequence and the matrix. Both of the fibre and matrix phase retain their own properties. With a varying matrix phase and fibre orientations, that can be combine of two or more of above categories, make composites are more flexible.

This text box is where the unabridged thesis included the following third party copyright material:

Zweben C. Composite materials and mechanical design. Mechanical Engineer's Handbook. 1998.

**Figure 1.1** *Classification of composite material systems (2).*

## **1.2 Fibre-reinforced Polymer (FRP)**

FRP composite is defined as a polymer that is reinforced by a fibrous phase. The primary function of fibre reinforcement is to carry load along the length of the fibre and to provide strength and stiffness in one direction. FRPs represent a class of materials that falls into a category referred to as composite materials. FRP composites are different from traditional construction materials like steel or aluminium. FRP composites are anisotropic, while steel and aluminium is isotropic. Therefore FRP composites properties are directional, meaning that the best mechanical properties are in the direction of the fibre reinforcement. Nowadays, the most common fibres are glass, carbon, boron and aramid fibres

### 1.2.1 Glass Fibres

Glass wool, which is commonly known as "fibreglass" was invented in 1938 by Russell Games Slayter as an insulation material. It is marketed under the trade name Fibreglas. Glass fibres are widely used in the marine industry due to its low cost, ease of fabrication, low maintenance and corrosion resistance. The basis of textile-grade glass fibres is silica and the most commonly used fibre is known as E-glass. The letter E is used because it was originally for electrical applications. Glass fibres offer a high chemical resistance, good mechanical and electrical properties. However, E-glass suffers degradation in environments which are highly acidic or alkaline. For this reason a number of more resistant glasses have been developed namely AR- glass (alkali resistance-glass) and C-glass (chemical-glass). AR-glass is a special glass fibre with a high percentage of zirconia to increase its corrosion resistance. In contrast, C-glass grade is contains a high percentage of calcium borosilicate to give it chemical stability in corrosive acid environments. Other types of glass fibre include S-glass based on silica oxide, aluminium oxide and magnesium oxide. This glass fibre has a higher stiffness and strength than E-glass, however, it is more expensive. Typical mechanical properties of glass fibres are given in **Table 1.1**.

	E-glass	S-glass	AR-glass	C-glass
Density (kg/m <sup>3</sup> )	2580	2490	2700	2520
Tensile strength (MPa)	3445	4750	3241	1533
Young Modulus (GPa)	72	89	73	69
Tensile failure strain (%)	4.8	5.4	4.4	4.8

**Table 1.1** *Typical mechanical properties of glass fibres (3).*



### 1.2.2 Carbon Fibres

In 1958, Roger Bacon developed a high-performance carbon fibre at the Union Carbide Parma Technical Center, Ohio. Those fibres were manufactured by heating strands of rayon until they carbonised. This process proved to be inefficient, as the resulting fibres contained only about 20% carbon and had low strength and stiffness properties. In the early 1960s, a new process was developed by Dr. Akio Shindo at the Agency of Industrial Science and Technology of Japan, by using polyacrylonitrile (PAN) as a raw material. This process was produced a carbon fibre that contained approximately 55% carbon. Since 1970, carbon fibre reinforced plastics (CFRP) have been extensively used in civil aircraft because of their superior specific strength and specific modulus compared with most other engineering materials. The mechanical properties of a unidirectional CFRP composite with approximately 60 % of fibres by volume in an epoxy matrix are given in **Table 1.2**.

Density (kg/m <sup>3</sup> )	1790
0° Young's modulus (GPa)	141
90° Tensile strength (MPa)	81
0° Tensile strength (MPa)	2205
0° Tensile failure strain (%)	1.55
0° Compressive strength (MPa)	1530

**Table 1.2** *Typical mechanical properties of a AS4 carbon fibre reinforced epoxy (4).*

### 1.2.3 Boron Fibres

Boron fibres were developed and first marketed in early 1960. These high strength and high modulus fibres were found application in composite structural components on the U.S Air Force F-15 and the US Navy F-14 aircraft. Boron fibres are being produced as a monofilament of wire by chemical vapour deposition (CVD) of boron onto tungsten substrate. The diameters of the fibres are in a range from 0.05 to 0.4 mm, resulting these materials having extremely high compressive strength. However, boron fibres cannot be expected to compete with the carbon fibres in-term of production cost. Typical mechanical properties of boron fibres are given in **Table 1.3**.

Density (kg/m <sup>3</sup> )	2650
Tensile strength (MPa)	3500
Young Modulus (GPa)	420
Tensile failure strain (%)	0.8

**Table 1.3** *Typical mechanical properties of boron fibres (5).*

### 1.2.4 Aramid Fibres

Aramid is a generic term for aromatic polyamide fibres and was first introduced in commercial applications in the early 1960. These high performances of fibres are marketed by DuPont and called Kevlar. This high strength material was first used in early 1970 as a replacement for steel in racing tyres. There are various types of Kevlar fibres available on the market and most commonly used are Kevlar-29. Kevlar-29, with a modulus higher than S-glass, is used in cables, brake linings, and body or vehicle armour. However, it also displays a far lower compression strength than carbon and relatively poor adhesion to the matrix resin.

In the mid-1960s, DuPont was produced the meta-aramid also known as Nomex. In 1967, this flame-resistant materials were commercially used in the aircraft industry. In 1987, a similar fibre called Twaron, with roughly the same chemical structure as Kevlar, was introduced by Teijin. Some typical mechanical properties of aramid fibres are summarised in **Table 1.4**.

	Kevlar 29*	Kevlar 49*	Nomex*	Twaron**
Density (kg/m <sup>3</sup> )	1430	1450	1380	1440
Tensile strength (MPa)	2900	2900	3300	3000
Young Modulus (GPa)	70	130	17	67
Tensile failure strain (%)	3.6	2.8	22	3.3

**Table 1.4** *Typical mechanical properties of the Kevlar\* (6), the Nomex \*(6) and Twaron \*\* (7) fibres.*

The basic properties of a composite depend on the fibre, the matrix and the interface between the fibre and the matrix. **Figure 1.2** shows stress-strain curves for typical fibres used in structural industries. From the figure, most of the fibres are brittle. Recently, these various fibres can be combined to form a new **hybrid composite**.

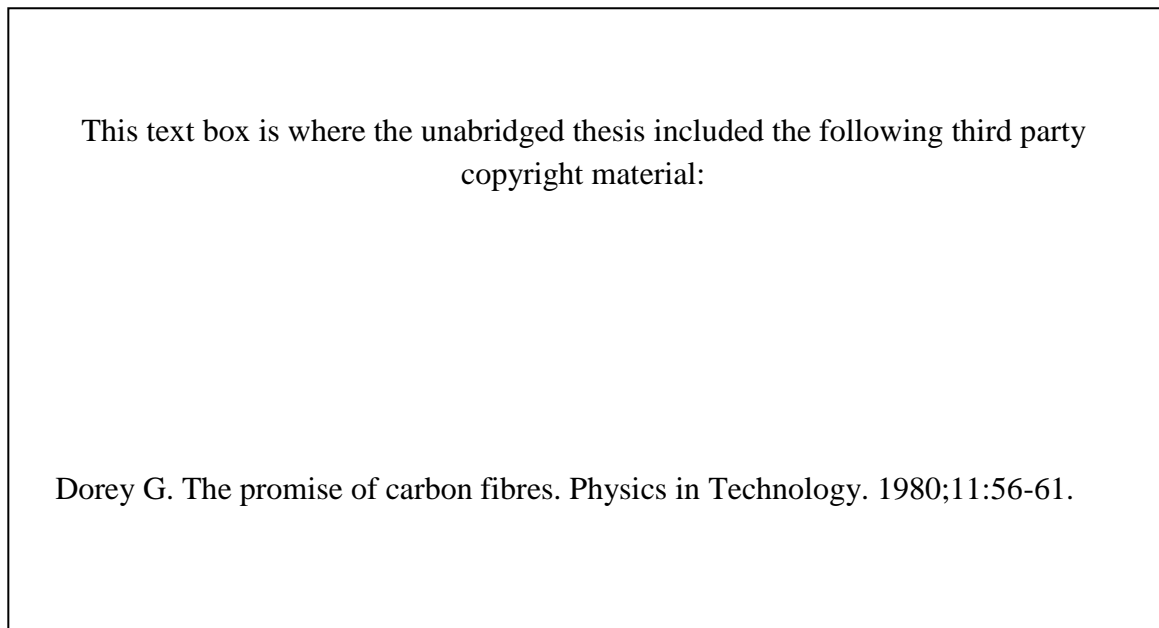


**Figure 1.2** *Stress-strain curves for some typical fibres (8).*

### 1.3 Matrices

The main purpose of the matrix is to support the reinforcement, to protect the fibre from the environment effect of corrosion and to transfer load between the reinforcement. Typically, the fibre is stronger and stiffer than the matrix. In addition, the matrix therefore controls the transverse properties and the interlaminar strength of the composite. The matrix holds the reinforcement in the desired position so that they can effectively carry the load. For the composites subjected to impact, delamination is a common failure mechanism occurring predominantly in the matrix. In general, polymeric matrices can be classified into thermosetting and thermoplastic resins.

### **1.3.1 Thermosetting Resins**

It has been estimated that over-three quarters of all matrices of polymer matrix composites are thermosetting polymers. Epoxy resins are presently used far more than all other matrices in composite materials. Epoxies are generally superior to polyesters in resisting moisture and other environmental influences. It also offers a lower cure shrinkage and better mechanical properties. However, the elongation-to-failure of most cured epoxies is relatively low. For many applications, epoxies provide an almost unbeatable combination of handling characteristics, processing flexibility and mechanical properties. Another widely used thermosetting matrix is polyester resin. The development of highly effective silane coupling agents for glass-fibres allowed the fabrication of glass-fibre reinforced polyesters with excellent mechanical properties and an acceptable environmental durability. However, the lower degree of adhesion to carbon and aramid fibres have reduced the use of polyester as a matrix in composite laminates. In addition, bismaleimide resins possess many of the same desirable features as do epoxies, include excellent properties and a relative ease of processing. However, they are quite brittle and a low elongation to failure.

### **1.3.2 Thermoplastic Resins**

Thermoplastic materials represent the widest variety and the largest percentage of plastics in use. Thermoplastics can be melted and reformed with heat, making them ideal for multiple reuse. Commodity thermoplastics such as polyethylene, polyvinyl chloride and polystyrene are commonly used as in the manufacture of plastic bags, plastic bottles and plastic tableware. These well-established polymers exhibit a poor resistance to elevated temperatures and easily degrade. In contrast, high-performance thermoplastics are used in specialised applications that require a combination of extraordinary properties. They have superior thermal stability, chemical and radiation resistance, resistance to burning and excellent mechanical properties. These resins include polyetheretherketone (PEEK), polyphenylene

sulphide (PPS), polyetherimide (PEI), polyimide (PI) and polyarylsulfone (PAS). Under impact conditions, Dorey *et. al.* (9) reported that PEEK exhibits a higher impact resistance than that of epoxy resin matrices, as shown in **Figure 1.3**.

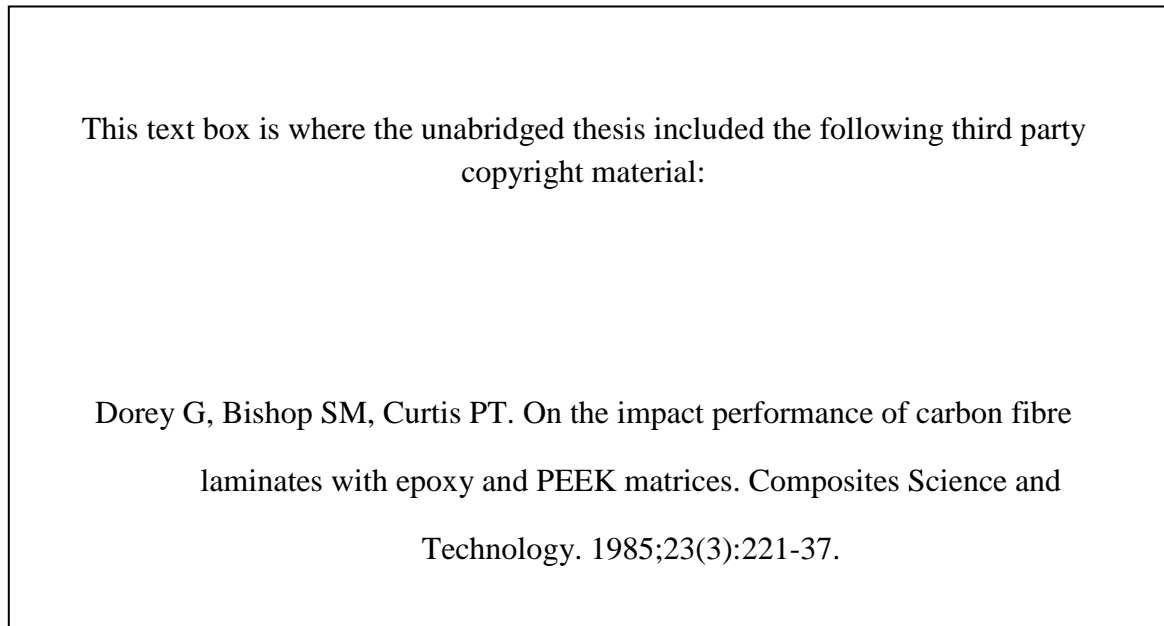


**Figure 1.3** *Variation of delaminated area following drop-weight impact on carbon/epoxy and carbon/PEEK laminates with a  $[\pm 45, 0_3, \pm 45, 0_2]_s$  lay-up (9).*

## 1.4 Interface

The load acting on the matrix in a composite has to be transferred to the fibre via the interface. The interface can be viewed as a planar region of only a few atoms in thickness across in which there is a change in the properties of composite. The fracture behaviour is also dependent on the strength of the interface. A weak interface results in a low stiffness and strength but a high resistance to fracture, however materials with a high stiffness and strength are often very brittle (10). Other characteristic of a composite including the resistance to fatigue, creep and environmental degradation are also influenced by the properties of the interface.

Many attempts have been made to improve the degree of bonding, including coating the fibres with polymers, electrolytic oxidation as well as vapour deposition of other compounds onto the fibres surface. The electrolytic oxidation treatment became the established method for carbon fibres, while silane coupling agents are used for glass fibres. In many cases, a perfect bond between the fibre and the matrix, forcing them to deform as one, often results in a lower tensile strength than expected.

## 1.5 Sandwich Structures

The basic concept of a sandwich structure is that the skins carry the bending and buckling loads while the core withstands the shear loads in the transverse direction. The skins are strong and stiff in tension and compression compared to the core material, whose primary purpose is to keep the facesheets separated in order to maintain a high second moment (11). Generally, sandwich structures are divided into two categories, homogenous and non-homogenous, as shown in **Figure 1.4**. The core materials are divided into four categories. These are foam, honeycomb, corrugated and textile cores.

This text box is where the unabridged thesis included the following third party copyright material:

Herrmann A, Zahlen P, Zuardy I. Sandwich structures technology in commercial aviation. *Sandwich Structures 7: Advancing with Sandwich Structures and Materials*. 2005:13-26.

**Figure 1.4** *Typical types of sandwich constructions (12).*

### **1.5.1 Skin Materials**

In a sandwich structure, the facesheets can be made of many different materials for example from isotropic, anisotropic or composite materials. Steel, aluminium, glass, carbon and aramid are the commonly used as the skins material in sandwich structures. However, in order to reduce the weight of the structure fibre reinforced composite facesheets are more preferable.

### **1.5.2. Core Materials**

The other main component of a sandwich structure is the core material. The core has a relatively low density, giving a result in high flexural strength and stiffness properties relative to the overall panel density. To maintain the effectiveness of the sandwich structure the core



must be strong enough to withstand the compressive or crushing loads placed on the panel. The core also must resist the shear forces involved. If the core collapses, the mechanical stiffness advantage is lost. The following section will briefly discuss the various core materials that are investigated in this study.

### **1.5.2.1 Polymer Foam**

Polystyrene (PS) foams were first made in 1931. However, polyurethane (PU) was invented by Dr. Otto Bayer at the beginning of the Second World War. It was first used as a replacement for rubber and also used as a coating to protect other common materials, such as metals and wood.

A few years after the war, flexible PU foam was invented and used for cushioning in furniture and in the automotive industry. Nowadays, common polymer foams include polymethacrylimide (PMI), polyethylene terephthalate (PET), styreneacrylonitrile (SAN) and polyvinyl chloride (PVC) foams.

The mechanical response of polymeric foams depends on the geometric characteristics of the cell, such as the cell wall thickness, density, shape and size distributions, and on the intrinsic properties of the polymer in the cell wall (11). Typical compression load-displacement traces for PMI foam with increasing density are shown in **Figure 1.5**.

This text box is where the unabridged thesis included the following third party copyright material:

Matthews FL, Rawlings RD. Composite Materials: Engineering and Science:  
Woodhead Publishing; 1999.

**Figure 1.5** *Typical stress strain curve for PMI foam (11).*

It shows an initial linear increase in stress and a plateau regime of nearly constant stress in the middle region, which is followed by a steep increase in flow stress at the end of the test. In general, this trend is similar for most polymer foams based on both open and closed cells. From **Figure 1.5**, the large plateau stress is common to polymer foam, indicating that the foam can be compressed to very large strains at a constant force. They have great potential to absorb large amounts of energy at relatively low stresses. To this extent, polymer foams are usually employed to improve the energy absorption capabilities of the structures. However, significant degradation of the properties of the polymer foam occurs at lower temperatures and environmental effects such as moisture and humidity where a complete loss of stiffness and strength are experienced.

### **1.5.2.2 Honeycomb Cores**

Honeycombs are based on series of cells, nested together to form structures similar in appearance to the cross-sectional slice of a beehive. In its expanded form, a honeycomb is 90-99 percent open space structure. Honeycomb structures are produced by using a variety of different materials, depending on their end application. For example honeycomb cores made from polypropylene are used for low strength and stiffness load applications, while aluminium honeycomb cores with high strength and stiffness are used in high-performance applications. In addition, aluminium honeycombs are fire-retardant and have a good impact resistance. They offer the best strength to weight ratio of the core materials used in aircraft industries. However, aluminium honeycomb is more expensive and difficult to use in complex shapes. In general, the mechanical properties of honeycombs are highly anisotropic. In sandwich construction with foam or honeycomb as a core, the primary loads are carried by the facesheets, however, in textiles or truss-cored structures, a portion of the primary load is carried by the core.

### **1.5.2.3 Corrugated Cores**

Corrugated core, especially cardboard, is well known for its low cost. Corrugated paper was patented in England in 1856, and used as a liner for tall hats. The single-sided corrugated board patent was awarded to Albert Jones (13) in 1871. Jones used the corrugated board for wrapping bottles and glass lantern chimneys. The first machine for producing large quantities of corrugated board was built in 1874 by G. Smyth, and in the same year, Oliver Long (14) improved a design proposed by Jones and invented corrugated board with liner sheets on both sides.

During the past decade, many attempts have been made to study the effect of dynamic loading on corrugated core sandwich structures. Fleck and Deshpande (15) found that

corrugated cores offer a higher blast resistance than pyramidal lattice cores. In addition, the dynamic compressive behaviour of corrugated sandwich structure is considerably different from their response under quasi-static conditions. Kazemahvazi *et. al.* (16) reported that when corrugated structures are loaded quasi-statically, they typically fail through plastic buckling with a sharp drop in load after the initial peak. However, it was shown that the buckling response of the core decreased significantly with increasing loading rate, resulting in an increased peak load in the structures. **Figure 1.6** shows a typical stress-time history for a CFRP corrugated core following dynamic testing.

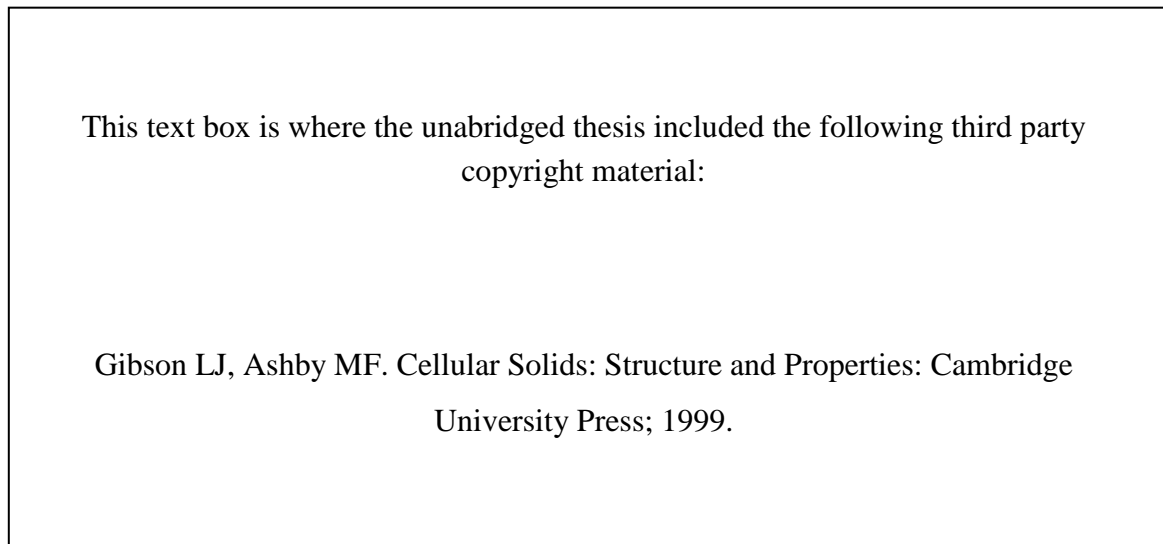


**Figure 1.6** Typical stress-time history of the CFRP corrugated core at a different impact velocities (16).

## 1.6 Adhesive

Adhesive systems are formulated to bond any combination of core materials and rigid layers. The quality of the final panel depends on the choice of adhesive, efficient application of the adhesive and a surface pre-treatment. Production cycle times and output are also dependent on the type of adhesive used and its thin film reactivity. In general, the most commonly-used

adhesive systems are based on epoxy resins, due to their higher ability to bond to the core, their resistance to fatigue and their good mechanical properties.

## **1.7 Composites Applications**

Composites are used in a wide range of applications, including aerospace, transportation, construction, marine, and sporting goods. In general high-performance, but more costly carbon-fibre composites, are used where high strength and stiffness, along with light weight are required. However, much lower-cost fibreglass composites are used in less demanding applications, where weight is not as critical.

Wind power is one of the world's fastest growing green energy sources. Recently, the blades for large wind turbines have been made from composites. The blades can be as long as 37 metres with a weight up to 5200 kg. In 2007, nearly 50,000 blades for 17,000 turbines were manufactured. The blades used approximately 180 million kg of composites (17). The main material is glass fibres, manufactured by either hand lay-up or resin infusion. Currently, the use of composites for electrical towers and light poles, typically made from pultruded or filament-wound of glass fibre is greatly increasing.

Composite laminates are not new in the aircraft industry. Since the first glass fibre-reinforced aircraft entered production in 1957, composites have been used extensively in military applications. In recent years, manufacturers have started to use lightweight composites in their designs, without having to compromise strength and durability for almost every component of their aircraft. For example, rotor blades in helicopters are based on glass fibre-reinforced epoxies for improved fatigue resistance, while their airframes have been built largely from carbon-fibre composites.

In 1985, the Airbus A310 and A300-600 aircraft were the first airliners to use fibre composites for a major structural component. The vertical fins of these aircraft were

fabricated from carbon-fibre, with other components, such as the wing leading edge, control surfaces and fairings, also made from composites. The use of composite empennages was also carried across into the highly successful A320, A330 and A340 aircraft, allowing optimisation of the vertical fin to improve the aerodynamics and hence the flying characteristics, of the aircraft (18).

Boeing began using composites in 737 spoilers over 35 years ago. Composite laminates have been now replaced alloy structures to create significantly lighter and lower cost of maintenance for the Boeing 737 family of aircraft as well as the 757, 767 and 777 product lines. The Boeing 787 Dreamliner is approximately 50% composite material by weight, with much of that being carbon fibre laminates or sandwiches. It will be the first airliner that is primarily composite, with a fully composite skin, fuselage, wing box and empennage. **Figure 1.7** highlights the key fibre composite components used in the Dreamliner 787. **Figure 1.8** shows the growth of composite structures in major aircraft programmes between 1975 and 2010.

This text box is where the unabridged thesis included the following third party copyright material:

Nelson T. 787 Systems and Performance. The Boeing Company. 2005.

**Figure 1.7** *Composite applications on the Dreamliner 787 (19).*

This text box is where the unabridged thesis included the following third party copyright material:

Taylor RP. Fibre composite aircraft – capability and safety, Australian Transport Safety Bureau. AR-2007-021. 2008.

**Figure 1.8** *The growth of composite structures in major aircraft programs (1975-2010) as a percentage of weight (20).*

The automotive industry is increasingly turning to composites to achieve improved performance, including high mechanical properties and weight requirements. The increasing cost of steel after World War 2 resulted in General Motors introducing fibreglass in the manufacture of the Corvette sports car. In 2002 the Ferrari Enzo was the first car to be all-carbon in its structure and bodywork (21). Currently, there is a growing interest to use other high-energy absorbed characteristic material including metal foams, as shown in **Figure 1.9** and **Figure 1.10**. In addition, in Formula 1 racing cars, most of the chassis including the monocoque, suspension, wings, and engine cover are made from carbon fibre composites.

This text box is where the unabridged thesis included the following third party copyright material:

Banhart J. Aluminium foams for lighter vehicles. International Journal of Vehicle Design. 2005;37(2):114-25.

**Figure 1.9** *Prototype of a BMW engine mounting bracket manufactured by LKR Ranshofen (Austria). From left to right: empty casting, entire composite part consisting of aluminium foam core and cast shell, section through composite part (22).*



This text box is where the unabridged thesis included the following third party copyright material:

Banhart J. Aluminium foams for lighter vehicles. International Journal of Vehicle Design. 2005;37(2):114-25.

**Figure 1.10** *Crash energy absorber made from rubber, polymer and aluminium foam for a tram built for the Combino vehicle system (22).*

Corrosion is a major problem and expense for the marine industry. Composites help minimise these problems, primarily because they do not corrode like metals or rot like wood. Kayaks and boats have long used glass fibres, mostly for their durability and weight saving capability over metal. The hulls of boats, ranging from small fishing boats to large racing yachts are commonly made of glass fibres and polyester resins. Masts are frequently fabricated from carbon fibre composites. Jet skis and boat trailers often contain glass composites to help minimise weight and reduce corrosion. More recently, the topside structures of many naval ships have been fabricated from composites.

Using composites to improve the infrastructure of roads and bridges is a relatively new and exciting application. Many of the world's roads and bridges are badly corroded and in need of continuous maintenance and replacement. In construction, pultruded fibre-glass is used to strengthen concrete.

In sporting goods, tennis racquets for years have been made of glass, while many golf club shafts are made of carbon.

## 1.8 Major Contribution of Thesis

As stated above, composites offer many advantages over metallic materials when specific strength properties are considered. The use of composite laminates as skins and low density cellular materials as cores in sandwich constructions yields structural components with a high stiffness and strength-to-weight ratios. In sandwich constructions, polymer foams are the popular core materials in high-performance applications due to their superior mechanical properties including an excellent to shear strength. However, because of the low stiffness of the core, sandwich structures are susceptible to indentation effect. Hence, the aims of this research are to investigate and understand the effect of the loading rate on the indentation resistance of the polymer-foam based sandwich structures. Part of this work investigates strain-rate effects in a wide range of mechanical properties of polymer foams. Initial attention focuses on the compression response. This is subsequently extended to consider the Mode I and Mode II fracture response of the foams. Following this, the effect of varying the skin, indenter radius and core properties on the indentation behaviour of sandwich structures based on a range of polymer foams will be investigated.

Another fundamental aim of the present work is to investigate and understand the perforation response of sandwich structures under low velocity loading. The perforation resistance of a range of glass fibre/epoxy sandwich structures will be investigated. A simple model will be used to predict the impact perforation resistance of the polymer foam-core sandwich structures. This study will also investigate the perforation response of sandwich structure by varying the properties of the polymeric foam, the skin thickness and support condition. Particular attention will also be given to investigating the energy-absorbing characteristics of fully recyclable sandwich structures. The perforation resistances of a range of all-polypropylene sandwich structures will also be investigated. Attention will centre on the investigating effect of key parameters, such as the design of the composite skins, on the perforation resistant of these sandwich structures. Comparative studies with the corrugated

paperboard and on more traditional sandwich structures GFRP/aluminium honeycomb sandwich structure will be discussed.

## **1.9 Thesis Organisation**

This thesis is divided into six chapters, describe as follow:

- Chapter I presents an overview of composite materials and their applications, highlighting the objectives of this research.
- Chapter II presents a literature survey on the subject of the impact resistance of the composite structures.
- Chapter III describes the experimental work performed in this study.
- Chapter IV presents and discusses the mechanical properties obtained from tests on the core materials.
- Chapter V presents discusses the low velocity impact response following tests on the sandwich structures.
- Chapter VI presents the conclusions and recommendation for future work.

## 1.10 References

1. Miracle DB, Donaldson SL, editors. Composites, vol. 21. Materials Park: ASM International; 2001; 3–17.
2. Zweben C. Composite materials and mechanical design. Mechanical Engineer's Handbook. 1998.
3. Wallenberger FT, Watson JC, Li H. Glass fibers. ASM Handbook. 2001;21:27-34.
4. <http://www.hexcel.com/resources/datasheets/carbon-fiber-data-sheets/as4.pdf>
5. Lubin G. Handbook of Composites: Springer; 1998.
6. [http://www2.dupont.com/Kevlar/en\\_US/assets/downloads/KEVLAR\\_Technical\\_Guide .pdf](http://www2.dupont.com/Kevlar/en_US/assets/downloads/KEVLAR_Technical_Guide.pdf).
7. <http://www.teijinaramid.com/aramids/twaron/>.
8. Dorey G. The promise of carbon fibres. Physics in Technology. 1980;11:56-61.
9. Dorey G, Bishop SM, Curtis PT. On the impact performance of carbon fibre laminates with epoxy and PEEK matrices. Composites Science and Technology. 1985;23(3):221-37.
10. Matthews FL, Rawlings RD. Composite Materials: Engineering and Science: Woodhead Publishing; 1999.
11. Gibson LJ, Ashby MF. Cellular Solids: Structure and Properties: Cambridge University Press; 1999.
12. Herrmann A, Zahlen P, Zuardy I. Sandwich structures technology in commercial aviation. Sandwich Structures 7: Advancing with Sandwich Structures and Materials. 2005:13-26.

13. Jones AL, inventor; Improvement in paper for packing, US patent 122,023; December 19,1874.
14. Long O, inventor; Packings for bottles, jars & c; US patent 150,588; May 5, 1874.
15. Fleck NA, Deshpande VS. The resistance of clamped sandwich beams to shock loading. *Journal of Applied Mechanics*. 2004;71:386-401.
16. Kazemahvazi S, Russell BP, Zenkert D. Impact of carbon fibre/epoxy corrugated cores. *Composite Structures*. 2012;94(11):3300-8.
17. Campbell FC. *Manufacturing Technology for Aerospace Structural Materials*: Elsevier Science; 2006.
18. Middleton D. *Composite Materials in Aircraft Structures*: Halsted Press; 1990.
19. Nelson T. *787 Systems and Performance*. The Boeing Company. 2005.
20. Taylor RP. Fibre composite aircraft – capability and safety, Australian Transport Safety Bureau. AR-2007-021. 2008.
21. <http://www.roadandtrack.com/special-report/structural-composites-in-cars>.
22. Banhart J. Aluminium foams for lighter vehicles. *International Journal of Vehicle Design*. 2005;37(2):114-25.

## **CHAPTER II**

### **LITERATURE REVIEW**

---

In this section, an overview of the literature relating to the impact response of composite materials will be presented. Firstly, the chapter discusses the general issues around the topic, including classification of impact loading conditions and contact mechanics. Following this, the literature review will focus on those of factors that influence the impact performance of composite materials and structures. This particular section is divided into two parts, the first dealing with composite laminates and the second with sandwich structures. Finally, the relevant perforation models will be briefly discussed.

## 2.1 Classification of Impact Response

The impact response of composite materials can be classified into two different categories to distinguish between low velocity and high velocity impact. Currently, there are two fundamental responses that can be used to categorise the impact phenomenon. One is based on structural deformation and the other on the structural response which depend on the velocity, mass and duration of impact. Shivakumar *et. al.* (1) and Sjoblom *et. al.* (2) proposed that low velocity impact events can generally be treated as quasi-static, whereas the high velocity impact response of a structure is dominated by stress wave propagation through the material. Under conditions of high velocity impact loading, the structure does not have time to respond, leading to localised damage. Cantwell and Morton (3) suggested that high velocity impact loading induces a localised form of target response, where most of the energy is dissipated over a very small zone immediate to the point of impact. In contrast, low velocity impact loading generates an overall mode of target deformation whereby energy can be dissipated away from the point of contact. Liu and Malvern (4) and Joshi *et. al.* (5) noted that low velocity impact damage is dominated by delamination and matrix cracking, whereas high velocity impact is characterised by perforation and fibre breakage.

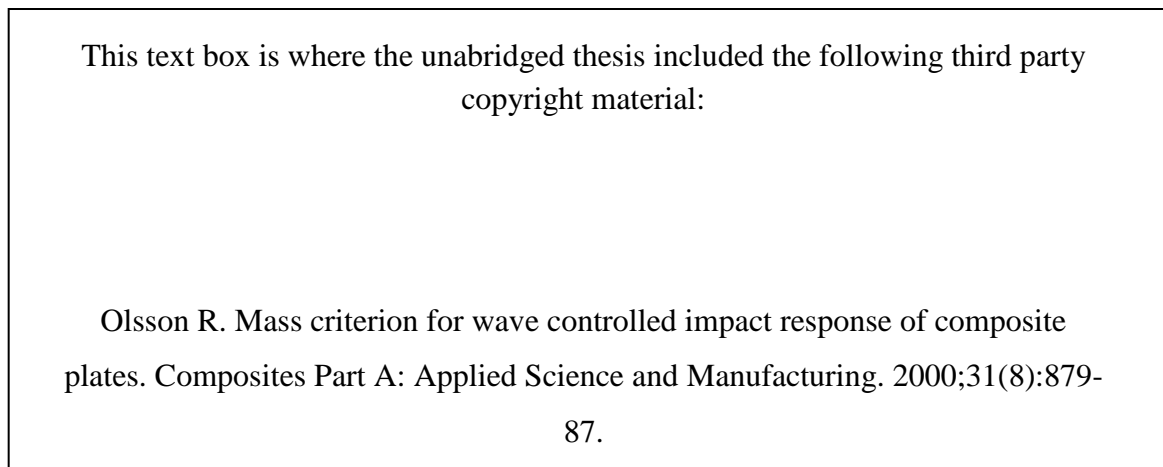
Zukas (6) characterised the impact response of structures as a function of impact velocity and strain-rate. He classified the impact regime into a low ( $>250$  m/s), medium (250 – 2000 m/s), ballistic (2000 – 12 000 m/s) and ultra-high ( $>12\ 000$  m/s) velocity impact conditions. In their review article on the impact resistance of composite materials, Cantwell and Morton (7) considered an impact velocity less than 10 m/s as low velocity loading, while Abrate (8) defined less than 100 m/s as inducing a low velocity impact response. Most workers (9, 10) have reported that the range of velocities between 1 and 5 m/s represent low velocity impact events. In contrast, Chen *et. al.* (11) defined a velocity range of 60 to 203 m/s for low velocity impact loading, which does not appear consistent with other workers.

Most researchers (7, 12) classified high velocity impacts as events such as those associated with runway debris, small arms fire, broken engine parts, broken turbine blades and fragments from a bomb. Abrate (8) stated an impact resulting in complete perforation of the composite as a ballistic impact. Here, it is important to determine the initial projectile velocity that will result in complete perforation of the composite, which is called the ballistic limit. Since several complex failure modes are involved in the perforation process, the generally accepted definition of the ballistic limit is the minimum velocity required to achieve a 50 % likelihood of perforation of the composite (8). There have been number of experimental studies conducted to investigate the ballistic limit of a variety of composite laminates and sandwich structures (13-22). The majority of these investigations have focused on five factors these being projectile density (13, 14), stacking sequence (15), laminate thickness (16, 17), projectile diameter and geometry (18-21) and obliquity of projectile (22). The majority of these experimental works (13-17, 22) have been conducted using a gas gun over a range of velocities between 20 and 750 m/s.

In addition to impact velocity, impact mass is also a key parameter to be considered when modelling the impact response of a composite structure. Swanson (23) pointed out that for composite plates subjected to an impact load, a quasi-static solution is only valid when the impactor mass is greater than ten times the lumped mass. Olsson (24, 25) considered the impact response of a composite in terms of boundary-controlled and wave-controlled impact. For boundary-controlled impact, the entire plate is deformed during the impact event and the contact force and plate response are in phase, as shown in **Figure 2.1(a)**. However, for wave-controlled impact, plate deformation is localised to the region around the point of impact, and the contact force and resulting displacement are never in phase, as shown in **Figure 2.1(b)**. Generally, boundary-controlled and wave-controlled impacts are associated with large-mass and small-mass impact responses. An impactor to plate mass ratio based criterion, governing a boundary-controlled impact response, has been derived in detail by Olsson (25). He



concluded that small-mass and large-mass impact occurs when the impactor-plate mass ratio is less than one-fifth and more than two respectively.



(a)

(b)

**Figure 2.1** *Comparison between boundary-controlled and wave-controlled impact*  
(24).

Although, Olsson's (24, 25) approach for categorising the impact phenomenon is reasonable, as it considers the energy associated with impact and the contact time, the popular view that considers less than 10 m/s as a low velocity impact as suggested by Cantwell and Morton (7) is generally accepted for simplicity.

## 2.2 Contact Mechanics

When a composite structure is impacted by a mass, the resulting contact force and structural deformation need to be analysed. The evaluation of the contact force and deformation of the structure depends on a contact law. Abrate (8) defined a contact law as a relationship between the contact force and the resulting indentation, with the latter defined as the relative displacement between the indenter and the target. A more general form for the contact law was proposed by Meyer (26):

$$P = C\alpha^n \quad [2.1]$$

where  $P$  is the contact force,  $C$  is a contact stiffness,  $\alpha$  is the indentation and  $n$  is the contact coefficient. According to Hertz's theory of contact, the exponent  $n$  is equal to 1.5 for contact between two isotropic homogenous linear elastic bodies. Recently, Yang and Sun (27) proposed a power law based on a static indentation test using a steel ball and agreed that the value of  $n$  is equal to 1.5 for a laminated target.

### 2.2.1 Indentation of Composite Laminates

Tan and Sun (28) investigated the impact response of carbon/epoxy laminates under quasi-static indentation and again the contact coefficient,  $n$ , was shown to be equal to 1.5 during loading, and a modified power law was applied for the unloading curves. They proposed the following:

Loading;

$$P = C\alpha^{1.5} \quad [2.2]$$

Unloading

$$P = P_m \left[ \frac{\alpha - \alpha_o}{\alpha_m - \alpha_o} \right]^q \quad [2.3]$$

where  $\alpha_m$  and  $P_m$  are the maximum indentation during loading and the maximum contact force at the beginning of unloading,  $\alpha_o$  is the permanent indentation. The indentation coefficient,  $q$  equalled 2.5 and 2.0 respectively for indenter diameters of 12.7 and 19.1 mm, respectively. Here, the contact stiffness can be expressed as:

$$C = \frac{4}{3} \left[ \frac{\sqrt{R}}{\frac{1-\nu_r^2}{E_r} + \frac{1}{E_p}} \right] \quad [2.4]$$

where  $R$  is the radius of indenter,  $\nu_r$  is the Poisson's ratio of the indenter and  $E_r$  and  $E_p$  are the Young's modulus of the indenter and plate, respectively.

Wu and Yen (29) considered the effects of stacking sequence, span and thickness and size on the contact force-indentation relationships in a number of carbon/epoxy laminates. They suggested that changing the stacking sequence and span of the laminated plates has a insignificant effect on the force-indentation relationship. They also showed that the modified Hertz contact law under-estimates the contact force for a large panel with a small indenter.

Wu and Shyu (30) investigated the effect of stacking sequence, indenter diameter, thickness and size on the indentation response of a carbon/epoxy laminate under quasi-static and dynamic loading. They stated that a modified Hertz contact law is not suitable for a thin laminate indented by a large indenter. They also reported that a simple contact law was not applicable if fibre splitting and delamination occurred in laminate. In addition, the delamination thresholds and contact histories for both quasi-static and dynamic loading condition were similar.

Sutherland and Soares (31) conducted an experimental study on the quasi-static indentation response of marine composites, based on woven rovings (WR) and chopped strand mat (CSM) composites. They found that a contact law worked well at smaller loads, while significant deviation was observed as extensive damage occurred at higher loads. On average, the measured contact coefficients,  $n$ , were 1.59 and 1.41 for the woven roving and chopped strand mat composites, respectively. **Figure 2.2** shows the variation of contact stiffness,  $C$ , with indenter radius following quasi-static testing. They suggested that the value of  $C^2$  tends to increase with projectile diameter in a non-linear fashion, as predicted by equation [2.4].

Lee and Liu (32) tested cross-ply glass/epoxy laminates under quasi-static and dynamic loading to investigate the effect of loading rate on the indentation response of composite laminates. **Figure 2.3** shows typical results from the resulting load-displacement traces following quasi-static and impact tests. They found that the static indentation data fit with the

indentation law proposed by Tan and Sun (28) when using a contact exponent  $n = 1.5$ . In contrast, during impact, the level of indentation decreases with impact velocity. They suggested that curve-fitting with a contact exponent  $n = 1.5$  did not give the best fit to the data.

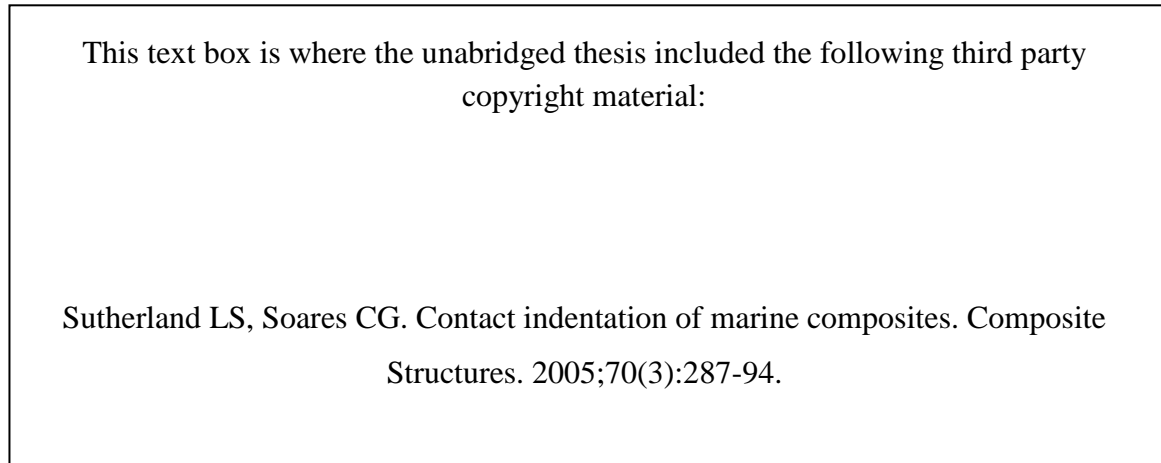


**Figure 2.2** *The variation of the power law contact stiffness with indenter radius following quasi-static indentation tests (31).*

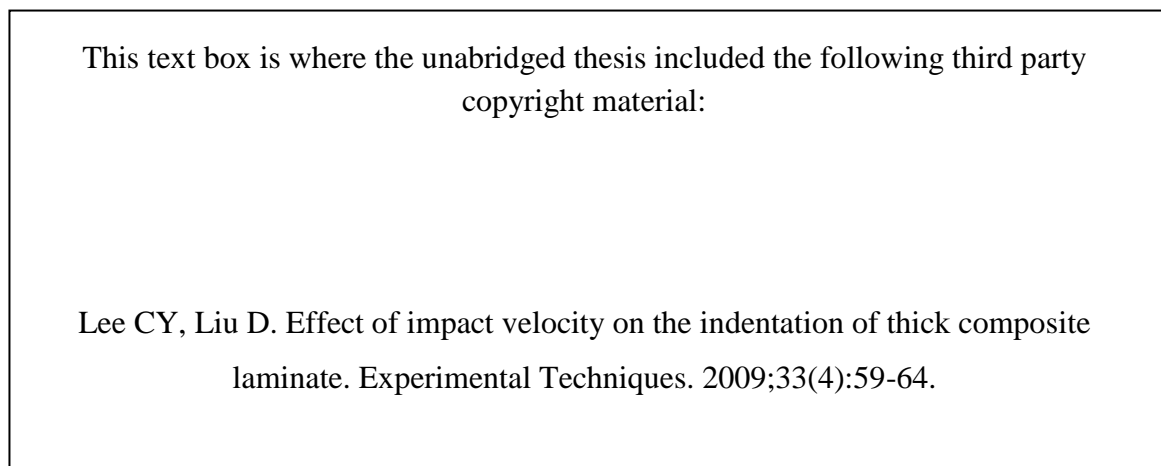


**Figure 2.3** *Typical load-displacement traces following quasi-static and impact tests on cross-ply glass/epoxy laminates (32).*

### 2.2.2 Indentation Response of Sandwich Structures

In general, the indentation response of a sandwich structure is determined by: (1) localised deformation in the region immediately adjacent to the impact site and (2) large elastic deformation of the surrounding panel (33). Localised indentation of a sandwich structure has been investigated extensively. Koller (34) showed that the Hertz law is inappropriate for sandwich panels containing a lightweight core. This is due to the fact that for sandwich structures consisting of high stiffness facesheets and a flexible core, deformation predominately occurs by crushing of the core. Lee *et. al.* (35) performed similar indentation tests to those conducted by Yang and Sun (27) to establish the contact law for a 12.7 mm spherical diameter steel indenter on a sandwich structure. The sandwich composite was made of [0<sub>2</sub>/90<sub>2</sub>/0<sub>2</sub>] carbon/epoxy skins and a polyurethane foam core. They found that the values of the contact coefficient for loading and unloading were 0.8 and 1.35 respectively. They also suggested that for sandwich structures with core materials other than polyurethane foam, the contact coefficients might be different.

Sburlati (36) investigated the force-indentation response associated with a rigid particle impacting a sandwich structure with carbon/epoxy skins and a PMI core. It was concluded that, whereas a Hertzian contact pressure distribution is appropriate for describing sandwich structures based on high-density core materials, it is not suitable for low-density systems. Zhou and Stronge (33) developed a contact law for indentation involving local deformation in a HSSA (hybrid stainless steel assembly) sandwich structure.

Here the contact force,  $P$ , is related to the indentation,  $\alpha$  through:

$$P = \frac{16\pi}{3} \sqrt{D\sigma_c \alpha \left( 1 + 0.488 \frac{\alpha^2}{h^2} \right)} \quad [2.5]$$

where

$$D = \frac{Eh^3}{12(1-\nu^3)} \quad [2.6]$$

$D$  is the bending stiffness of the facesheet,  $\sigma_c$  is the yield stress of the core, and  $h$  is the thickness of the skin. The first term on the right-hand side of equation [2.6] relates to bending of the facesheet and the second term considers local membrane stretching.

Soden (37) modelled a sandwich structure as a linear elastic composite beam on a rigid perfectly-plastic foundation. Theoretical fracture loads were found to be in good agreement with experimental data from tests on glass fibre/polyester polyvinyl chloride (PVC) sandwich beams. Akil (38) studied the indentation behaviour of foam-based sandwich structures with woven glass fibre/cynate ester resin facings with PUR/PVC and linear PVC foam cores. He showed that the contact parameter ' $n$ ' does not vary with loading rate and average value being close to 1.2. **Figure 2.4** summaries the indentation parameter with crosshead displacement rate.

Kiratisaevee and Cantwell (39) conducted indentation and dynamic tests on aluminium foam sandwich structures and fiber-metal laminate [FML] sandwich structures. They found that the parameter  $n$  for aluminium foam-based sandwich structures varied between 0.9 and 1.2 and between 0.7 and 0.9 for the FML sandwich structures. The average value of  $C$  for dynamic loading was significantly higher than that for the quasi-static data.

Rizov and co-workers (40-42) characterised the elasto-plastic response of closed-cell foams subjected to point and line loads. A finite element model, using a crushable foam hardening material model, was used to successfully predict the indentation response of the crosslinked foams. Results from residual indentation tests highlighted significant relaxation following unloading of the test samples. Rizov (42) investigated the quasi-static indentation response of a closed cell PVC foam with different thicknesses of GFRP skin. Here, it was shown that the

panels generally exhibited a non-linear load-indentation response, due to local foam crushing under the indenter.

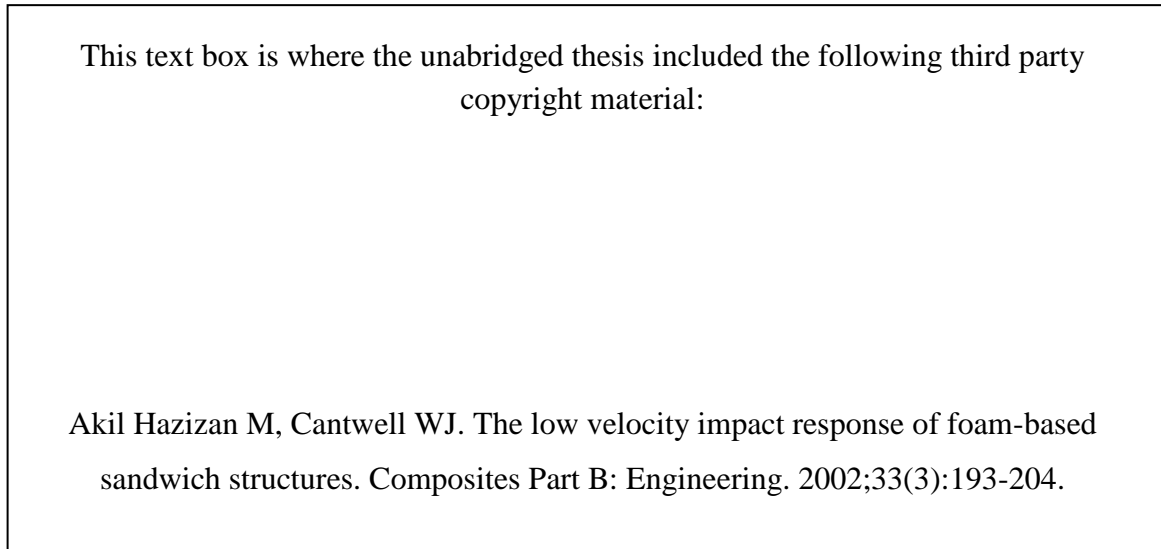


**Figure 2.4** *The variation of the indentation parameter with the crosshead displacement rate* (38).

### **2.3 Low Velocity Impact Response of Composite Laminate**

The impact response of composite laminate subjected to low velocity impact is influenced by both the test and specimen parameters. Test parameters include the impactor diameter and geometry, impact velocity and strain rate effect. The test specimen factors including specimen thickness, fibre, matrix and interface of the laminate. The following section will focus on many of those parameters that influence the impact behaviour of composite materials.

### 2.3.1 Effect of Impactor Diameter and Geometry

Abrate (8) stated that the critical contact force,  $P$ , is proportional to impactor diameter,  $d$ , and panel thickness,  $h$  according the equation:

$$P = \frac{(2\pi h \tau_{\max})^{\frac{3}{2}} d^{\frac{3}{4}}}{\sqrt{C}} \quad [2.7]$$

where  $\tau_{\max}$  refers to the maximum shear stress. The law assumes a Herztian pressure distribution that is high at the centre and zero at the edge. Experimental results by Whisler and Kim (43) showed that the peak contact force increased gradually with impactor radius. They conducted tests on a glass/epoxy with hemispherical indenter radius values of 12.7, 50 and 152 mm. Kim and Goo (44) used a finite element model to analyse the effect of varying the ratio between the impactor nose length and the impactor radius in a glass fibre reinforced plastic (GFRP) laminate. The ratios considered were 0.1, 1 and 10, where a ratio of 1 represents a hemispherical impactor. It was found that as the ratio decreased (i.e the projectile become more blunt), the peak force increased and the impact duration decreased.

Different impactor diameters and geometries will produce different damage mechanisms and areas in a composite laminate. A number of workers (30, 43, 45, 46) used different sized indentors to study damage initiation in composite laminates. Fin *et. al.* (45) reported that there was almost no correlation between the indenter radius and the delamination area for a carbon/PEEK composite plate. These tests were performed using steel hemispherical indentors with diameters of 6.35 and 12.7 mm. However, Wu and Shyu (30) showed that the influence of impactor diameter is significant when the contact load becomes very large. They showed that the delamination area increased with increasing impactor radius. Similar results were obtained by Amaro *et. al.*(46). They conducted low velocity impact tests on fully-clamped and supported circular CFRP laminates using hemispherical impactors with diameters of 12.7 and 20 mm. The impact test results showed that both the impactor diameter and the plate boundary conditions influenced the delaminated area. Under clamped



conditions, the delamination area increased by more than 17% when the impactor radius increased from 12.7 to 20 mm. Under quasi-static loading, Mines *et. al.* (47) reported that hemispherical and flat impactors produced larger delamination areas than conical projectiles in both woven and z-stitched laminates of varying thickness. Mitrevski *et. al.* (48) tested GFRP specimens using flat, hemispherical, ogival and conical impactors to study the effect of impactor shape under low velocity impact conditions. At an initial impact energy of 4 Joules, they stated that the damage induced by a flat impactor was very difficult to detect, however, damage for an ogival impactor was significantly smaller compared to both conical and hemispherical impactors.

### 2.3.2 The Effect of Impact Velocity

Mili (49) studied the impact behaviour of fully-clamped E-glass/epoxy laminates structures from velocities of 0.54 to 3.1 m/s using a drop-weight impact carriage. A Hertzian contact law was used to model the maximum impact force by using a spring-mass model approximation. It was found that the impact force and central deflections were proportional to the impactor velocity. Aggour and Sun (50) also conducted low velocity impact tests on E-glass/epoxy laminates at different impact velocities and reported that transverse deformation increases with increasing projectile velocity. However, the period of response decreases with increasing laminate thickness. Breen *et. al.* (51) investigated the low velocity impact response and developed a finite element simulation in order to investigate the effect of impact velocity on thick CFRP laminates. They found that higher velocity impacts induced a more localised response with high strains developing near the point of loading. They also showed that an impacted panel offered a 20% lower residual strength tensile compared to the statically-loaded condition. This indicates that the reduction in strength comes mainly from the stress concentrating effect of the damage.

### 2.3.3 Effect of Loading Rate on the Fracture Toughness of Composite Laminates

A number of workers (52-57) have used the double-centilever beam (DCB) geometry to study the effect of loading rate on the Mode I fracture toughness of composite laminates. Aliyu and Daniel (52) used the DCB specimen to investigate the Mode I fracture behaviour for carbon/epoxy composites. They found that the strain rate energy release rate,  $G_{Ic}$ , increased by 28% when the speed of loading increased from 0.0085 mm/sec to 8.47 mm/sec. In contrast, Smiley and Pipes (53) reported that the value of  $G_{Ic}$  remain constant for loading rates from  $10^{-11}$  to  $7 \times 10^{-7}$  m/s and decreased by up to 70 % over the next decade of loading rate. Both carbon/polyetheretherketone (PEEK) and carbon/epoxy composites were tested for comparison. Gillespie *et. al.* (54) used a similar specimen and test method to that proposed in (53) to study the viscoelastic effects at the process zone around the crack tip. They observed that the value of  $G_{Ic}$  decreased with rate of loading and attributed this to a ductile to brittle transition in the polymer in the process zone. This resulted in a 'stick-slip' phenomenon in at the load-displacement traces. A comparative study into the effect of loading rate on the Mode I interlaminar fracture toughness of carbon/PEEK laminate was conducted by Mall (55). **Figure 2.5** shows a comparison of published data for Mode I interlaminar fracture toughness as a function of strain rate. They observed a rapid reduction in fracture toughness of carbon/PEEK over five decades of loading rate. However, they did not give any reason why the data does not agree with that reported by Smiley and Pipes (53).

This text box is where the unabridged thesis included the following third party copyright material:

Mall S, Law GE, Katouzian M. Loading rate effect on interlaminar fracture toughness of a thermoplastic composite. Journal of Composite Materials. 1987;21(6):569-79.

**Figure 2.5** Comparison of Mode I interlaminar fracture toughness data as a function of strain rate (55).

The effect of loading rate on the Mode I fracture toughness of a carbon/epoxy composite using DCB and wedge-insert fracture specimens was investigated by Kusaka *et. al.* (56). They found that the value of fracture toughness decreased in a stepwise fashion with increasing loading rate. They divided the resulting fracture toughness graph into three distinct rate-sensitive regions, as shown in **Figure 2.6**. They used a simple kinetic model to explain the trends in this study. The DCB test geometry was also used by Hug *et. al.* (57) to investigate rate effects in the Mode I interlaminar fracture toughness of carbon/epoxy composites over a range at crosshead velocities between 0.004 and 1.6 m/s. They found the dynamic value of  $G_{Ic}$  was in a good agreement with that quoted in the previous study by Kusaka *et. al.* (56). These findings are shown in **Figure 2.7**.

This text box is where the unabridged thesis included the following third party copyright material:

Kusaka T, Hojo M, Mai YW, Kurokawa T, Nojima T, Ochiai S. Rate dependence of mode I fracture behaviour in carbon-fibre/epoxy composite laminates. Composites Science and Technology. 1998;58(3):591-602.

**Figure 2.6** *Rate dependence of Mode I interlaminar fracture toughness for two carbon fibre/epoxy composites (56).*

This text box is where the unabridged thesis included the following third party copyright material:

Hug G, Thevenet P, Fitoussi J, Baptiste D. Effect of the loading rate on mode I interlaminar fracture toughness of laminated composites. Engineering Fracture Mechanics. 2006;73(16):2456-62.

**Figure 2.7** *Influence of the loading rate on the crack-initiation values of  $G_{Ic}$  (57).*

A large number of studies have been focused on studying the effect of loading rate on the Mode II fracture toughness of composite materials (58-63). The end notch flexure [ENF] specimen geometry was used by Smiley and Pipes (58) to investigate the effect loading of rate on the shear strain energy release rate,  $G_{IIc}$ , of carbon/epoxy and carbon/PEEK composites. The fracture toughness for both materials remained constant at loading rates between  $10^{-5} - 10^{-8}$  m/s and decreased by approximately 85% at high loading rates. The decrease in the value of  $G_{IIc}$  was attributed to a decrease in the development of plastic deformation during loading. Maikuma *et. al.* (59) studied the effect of loading rate on the Mode II fracture toughness of carbon/epoxy and carbon /PEEK composites using the centre notch specimen (CNF) geometry. They reported that the initiation toughness under dynamic conditions was approximately 20 and 28% lower for carbon/PEEK and carbon/epoxy than their corresponding static values respectively. In addition, a comparative study into specimen geometry (ENF vs CNF) on the Mode II fracture toughness take from refs. (58, 60) is shown in **Figure 2.8**. It was suggested that the decrease in the value of  $G_{IIc}$  could be attributed to a transition from ductile to brittle matrix-dominated failure with increasing loading rate. Compston *et. al.* (61) reported higher values for the  $G_{IIc}$  of carbon/PEEK composites than for their brittle epoxy-matrix counterparts, this being in agreement with the observations by Smiley and Pipes (58) and Maikuma *et. al.*(59, 60). Similar conclusions were also made for glass fibre composites based on a range of brittle thermosetting matrices (61).

This text box is where the unabridged thesis included the following third party copyright material:

Maikuma H, Gillespie JW, Wilkins DJ. Mode II interlaminar fracture of the center notch flexural specimen under impact loading. *Journal of Composite Materials*. 1990;24(2):124-49.

**Figure 2.8** *Summary of the variation of the Mode II fracture toughness with strain rate for carbon/epoxy and carbon/PEEK laminates (59).*

The aforementioned studies (58-61) were carried out by using a standard universal testing machine to study the effect of varying loading rate on the value of  $G_{IIc}$ . In most practical situations, the rate at which a composite structure is loaded is difficult to determine. Cantwell (64, 65) used a screw-driven universal testing machine and a drop-weight impact test in order to examine the rate dependence of the Mode II fracture toughness of a carbon/PEEK composite. He found that the value of  $G_{IIc}$  of the composite laminate increased with increasing loading rate. The presence of fibre bridging was suggested as influencing the fracture toughness properties of the carbon/PEEK composite. Similar conclusions were also reported by Berger and Cantwell (66), where the value of  $G_{IIc}$  for a carbon/PEEK composite increased over three decades of loading rate. However, the Mode II interlaminar fracture toughness of the system decreases with increasing temperature, as shown in **Figure 2.9**. They

believed that the value of  $G_{IIc}$  for this material is strongly influenced by the yield stress of the thermoplastic matrix. In contrast, Compston *et. al.* (67) reported that there is no significant effect of loading rate on the fracture toughness of a glass/vinyl ester composite. They investigated the effect of loading rate using ENF specimens at loading rates ranging from 1 mm/min to 3 m/s using a universal testing machine and a drop-weight impact rig.

This text box is where the unabridged thesis included the following third party copyright material:

Berger L, Cantwell WJ. Temperature and loading rate effects in the mode II interlaminar fracture behavior of carbon fiber reinforced PEEK. *Polymer Composites*. 2001;22(2):271-81.

**Figure 2.9** *The variation of  $G_{IIc}$  with crosshead displacement rate for tests at temperatures between 20 and 150°C (66).*

A comparative study into the effect of loading rate on the Mode II interlaminar fracture toughness of carbon/PEEK and carbon/epoxy composite laminates was presented by Fracasso *et. al.* (68) and Kusaka *et. al.* (69). Fracasso *et. al.* (68) while investigating the effect of loading rate on the fracture toughness of a carbon/PEEK composite material, found that the value of the Mode II toughness remains invariant of strain rate. These findings are shown in **Figure 2.10**. Shear plastic deformation in the matrix of the fibre reinforced plastic was suggested to be responsible for the small variation in fracture toughness.

This text box is where the unabridged thesis included the following third party copyright material:

Fracasso RR, M. Pavan, A. Frassine, R. The effects of strain-rate and temperature on the interlaminar fracture toughness of interleaved PEEK/CF composites. Composites Science and Technology. 2001;61(1):57-63.

**Figure 2.10** *Comparison of the published data for the Mode II interlaminar fracture toughness of carbon /PEEK laminates as a function of the reduced displacement rate (68).*

The split Hopkinson pressure bar [SHPB] technique has also been employed to carry out dynamic ENF tests and to assess the strain-rate dependence of the Mode II interlaminar fracture toughness of two types of carbon/epoxy composite with yield stresses 100 and 140 MPa (69). Here, it was shown that the fracture toughness decreased by 20 % over eight decades of loading rate, as shown in **Figure 2.11**. Smooth fracture surfaces, due to debonding at the interface between fibres and matrix, were observed at high strain-rates. In contrast, hackle-like fracture surfaces, due to brittle fracture were observed in the low strain-rate specimens.



This text box is where the unabridged thesis included the following third party copyright material:

Kusaka T, Yamauchi Y, Kurokawa T. Effects of strain rate on mode II interlaminar fracture toughness in carbon-fibre/epoxy laminated composites. *Le Journal de Physique IV*. 1994;4(C8):671-6.

**Figure 2.11** *Strain rate effects on Mode II fracture toughness (69).*

#### **2.3.4 Effect of Specimen Thickness**

The thickness of a composite structure has been recognised as an important factor in determining the targets response. Studies by Cantwell (70) on impacted of CFRP laminates with different thicknesses, concluded that changes in the target thicknesses influenced the mode of fracture in the laminate. He observed that for a thin plate, the impact event generated large tensile stresses in the lowest ply, resulting in delamination at the fibre-matrix interface. For thick targets, damage initiated due to the high contact stresses generated by the impactor. The cracks propagated downwards to form delamination. A schematic diagram of this type of damage progression is shown in **Figure 2.12**. This observation agrees with the findings of Takeda *et. al.* (71).

This text box is where the unabridged thesis included the following third party copyright material:

Cantwell WJ. The influence of target geometry on the high velocity impact response of CFRP. *Composite Structures*. 1988;10(3):247-65.

**Figure 2.12** *Schematic diagram of damage progression for a) thin and b) thick CRFP laminates (70).*

Many attempts have been made to study the effect of thickness on the delamination area in glass/epoxy laminates. Extensive studies by Liu (4) concluded that the delamination areas of thin plates are smaller than those in the thick plates. They conducted low velocity impact tests on cross-ply  $[0_3/90_3/0_3]$  and  $[0_5/90_5/0_5]$  laminates using a drop-weight impact test rig. Similar results were also reported by Cantwell and Morton (72). Also, the development of damage in the thin laminate is more rapid than in thicker plates. The test results are shown in **Figure 2.13**. The effect of target thickness on damage initiation in a carbon/epoxy composite was studied by Hitchen and Kemp (73). They showed that placing  $\pm 45^\circ$  plies on the outside of a laminate obviously increased the thickness of the laminate and resulted in an increase in damage initiation energy. Caprino *et. al.* (74) investigated the effect of thickness on the load required to introduce delamination in a carbon/epoxy composite using a drop-weight impact rig. They found that the force required to initiate delamination increases according to a power law of the order of 1.5. They also reported that the delamination energy in the impact region increases with increasing thickness.

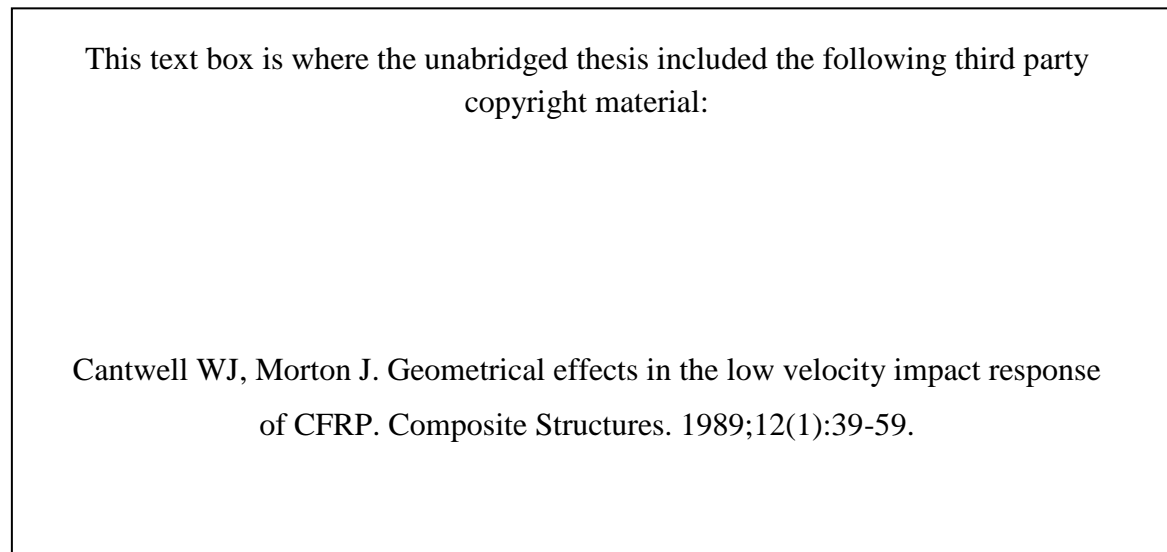


**Figure 2.13** *Development of damage as a function of impact energy for two (+/-45 °) of CFRP laminates (72).*

### 2.3.5 Influence of Constituents of the Composite Laminate

The properties of the constituent elements, including the fibre, matrix and the interface have a distinct effect on the impact behaviour of a composite material. The influence of the composite's constituent on its the impact behaviour will be discussed in the following sections.

#### 2.3.5.1 The Effect of Fibre Properties

Fibres, being the principal load-bearing element of a composite structure, contribute significantly to its strength and stiffness. Fibre properties, particularly the strain energy to failure, have a significant effect on the impact properties. Glass fibres have a lower strength and stiffness than carbon fibres; however they offer a superior impact resistance than carbon fibres, due to their higher strain to failure (75). Following Charpy impact tests, Adams and

Miller (76) showed that the impact resistance of S-glass and Kevlar fibre reinforced composites was over five times greater than that of a carbon/epoxy laminate. Dorey *et. al.* (77) showed that Kevlar/epoxy composites offer better impact properties than carbon/epoxy composite where threshold energies for the onset of damage were up to five times higher. They found that the fracture energy and residual strength of Kevlar/epoxy laminates were higher than those of a carbon/epoxy of most of the incident impact energies. Liu (78) showed that for laminates with a configuration of  $[0/90]_s$ , Kevlar/epoxy panels exhibit a larger delamination area than carbon/epoxy while glass/epoxy displayed the smallest area. This is probably due to the low interfacial shear strength in the Kevlar/epoxy plates. In other words, the low interfacial bond strength associated with Kevlar/epoxy laminates dramatically reduced their delamination resistance.

Several researchers have used hybridization approaches to improve the damage resistance of composites (75, 79-84). Short and Summerscales (75, 80) reviewed the fabrication techniques, as well as the design and physical properties of hybrid composites plates. Hybridisation studies showed that Kevlar/carbon epoxy composites offer a higher impact resistance than plain laminates, where the damage threshold energies were up to four times higher than that for a carbon/epoxy composite (80). A numerical analysis using the finite element method, was employed to predict the response of hybrid laminated composite plates subjected to low velocity impact by Lee *et. al.* (81). They showed that, a carbon/Kevlar/carbon plate has over three times absorbed energy compared to a Kevlar/carbon/Kevlar composite. They conclude that fibres with a lower modulus should be used on the composite surface to enhance the impact resistance of the hybrid composite (81). Imeilinska *et. al.* (82) used C-scan and X radiography techniques to detect impact damage in carbon, carbon/E-glass, Kevlar/carbon and Kevlar/glass composites following low velocity impact. They showed Kevlar/carbon hybrids exhibited the smallest damage areas. However, this hybrid offered a lower damage tolerance than the other laminates. This is due to high level of deformation and fibre breakage at point of impact. Hosur *et. al.* (84) conducted drop-

weight impact tests to study the impact behaviour of hybrid carbon/glass and carbon/epoxy composites. They observed that an improvement in the load carrying capability of hybrid composites as compared to S2-glass/epoxy and carbon/epoxy laminates. They also stated that placing glass fabric layers at the top and bottom surfaces of carbon/epoxy laminates can delay penetration of projectile and prevent splitting damage. Novak and DeCrescente (79) used Charpy specimens to characterise the impact properties of hybrid glass/carbon and glass/boron composites. They stated that the addition of glass fibres to carbon/epoxy and boron/epoxy composites increased the impact strength by a between three and five times compared to unhybridised laminates.

The stacking sequence of a composite influences not only its impact performance but also its post-impact residual strength and delamination area (7). Hong and Liu (85) investigated the effect of fibre orientation in  $[0_5/\theta_5/0_5]$  in GFRP laminates using a gas gun. They concluded that the delamination area increases significantly with increasing value of  $\theta$ . Finn *et. al.* (45) studied fibre orientation effects on delamination size in a carbon/epoxy composite. Tests were performed on 16-ply plates with  $[0_4/\theta_4]_s$  layups, by varying the angle from  $20^\circ$  to  $90^\circ$ . They found that the delamination lengths and widths were nearly independent of the mismatch angle,  $\theta$ , for values of  $\theta$  larger than  $40^\circ$ . The importance of the stacking sequence on the impact response of carbon/epoxy laminates was reported by Wu and Springer (86). They concluded that in a unidirectional laminate,  $[0_{16}]$ , no delamination occurs. Liu (78) showed that delamination area increased as the angle between two-ply increases, due to bending stiffness mismatch. He conducted low velocity impact tests on  $[0_4/15_4]$ ,  $[0_4/30_4]$ ,  $[0_4/45_4]$ ,  $[0_4/60_4]$ ,  $[0_4/75_4]$  and  $[0_4/90_4]$  glass/epoxy, carbon/epoxy and Kevlar/epoxy laminates. Strait *et. al.* (87) compared damage areas in various carbon/epoxy  $[0^\circ/\pm 45^\circ]$  laminates and found that quasi-isotropic laminates offer a better impact resistance than cross-play and  $[0^\circ/\pm 45^\circ]$  lay-ups. Cantwell (88) examined the effect of laminate stacking sequence of the high velocity impact response of CFRP. He showed that mixed-woven laminates offered the lowest resistance to ballistic perforation. Aktas and co-authors (89) performed

low velocity impact test to study the perforation resistance of GFRP composites. Two different stacking sequences,  $[0/90/0/90]_s$  and  $[0/90/+45/-45]_s$ , were chosen. The penetration threshold for the stacking sequence  $[0/90/+45/-45]_s$  was found to be smaller than that of a  $[0/90/0/90]_s$  laminate.

### 2.3.5.2 The Effect of Matrix Properties

The polymeric matrix in a fibre reinforced composite serves to protect, bond and align the fibrous structure. The stiff fibres support the stresses and the matrix serves to prevent fibre buckling under compressive loads (7). Relative to thermoplastics, thermosets offer advantages such as a high thermal stability, superior chemical and creep resistances (90). However they require a longer processing time, are unrecyclable and have a lower interlaminar fracture toughness (91). A comparative study by Pinnell and Sjoblom (92) investigating low energy impact damage in both thermoset (carbon/epoxy) and thermoplastic (carbon/PEEK) fibre reinforced composites highlighted the superior damage tolerance of thermoplastic matrices over thermosetting systems. This is in agreement with previous studies that have shown that delamination is more dominant in thermoset matrix materials (93-95). Carbon/PEEK offers an outstanding impact performance compared to the equivalent carbon/epoxy laminate (96). Prichard and Hogg (96) found the compression after impact (CAI) properties was significantly higher for thermoplastics compared to thermoset matrices, as shown in **Figure 2.14**. They concluded that the superior residual compression strength of carbon/PEEK is almost entirely due to its superior resistance to the initiation and propagation of impact damage. The reduced level of damage in thermoplastics may be explained by the materials higher values of  $G_{Ic}$  and  $G_{IIc}$  (53, 54, 58-60). Maikuma *et. al.* (59) reported that thermoplastic matrix composites absorb significantly more energy during crack propagation.

This text box is where the unabridged thesis included the following third party copyright material:

Prichard JC, Hogg PJ. The role of impact damage in post-impact compression testing. *Composites*. 1990;21(6):503-11.

**Figure 2.14** *The variation of residual compression strength after impact with impact energy following low velocity impact tests (96).*

In addition, differences have been observed within the thermoplastic family. Srinivasan *et. al.* (95) conducted low velocity impact tests on carbon/PEEK(AS-4) and carbon/PEEK(IM-7) panels to quantify the damage tolerance and resistance of composite materials using a drop-weight impact test. They found that the damage area for carbon/PEEK(IM-7) higher than for carbon/PEEK(AS-4) and suggested that the damage resistance of composite is a strong function of the matrix material. They observed that delamination in both laminates showed characteristic hackle marks associated with Mode II shear delaminations. Nejhad and Majidi (97) identified the influence dependence of the matrix following low velocity perforating impacts on carbon/PEEK and carbon/polyphenylene sulphide (PPS). They found that the perforation energy for carbon/PPS was significantly higher than for a carbon/PEEK composite, as shown in **Figure 2.15**. In-terms of specific energy absorption capability and interlaminar fracture toughness, carbon/PEEK laminates offered the highest specific energy compared to carbon/polyetherimide (PEI), carbon/polyimide (PI), and carbon/polyarylsulfone

(PAS) laminates (98, 99). The specific energy absorption and interlaminar fracture toughness of these materials are shown in **Table 2.1**. From data in the table, it was concluded that the higher energy absorption capability of the thermoplastic matrix increases the interlaminar fracture toughness of the composite laminate.

This text box is where the unabridged thesis included the following third party copyright material:

Nejhad G, Parvizi-Majidi A. Impact behaviour and damage tolerance of woven carbon fibre-reinforced thermoplastic composites. *Composites*. 1990;21(2):155-68.

**Figure 2.15** *The variation of impact damage area with incident impact energy for carbon/PEEK and carbon/PPS laminates (97).*

Fibre/Thermoplastic matrix	Interlaminar Fracture Toughness (kJ/m <sup>2</sup> )*	Specific Energy Absorption (kJ/kg)**
Carbon/PAS	0.4	128
Carbon/PI	0.9	131
Carbon/PEI	1.2	155
Carbon/PEEK	1.6	194

**Table 2.1** *The effect of matrix on the interlaminar fracture toughness \*(98) and specific energy absorption \*\*(99) of carbon/PAS, carbon/PI, carbon/PEI and carbon/PEEK.*



The effect of varying the matrix in a GFRP laminate subjected to low velocity impact loading using a Hopkinson bar was investigated by Al-Habak (100). He showed that polyester laminates offer an outstanding impact resistance compared to vinyl ester and epoxy laminates. He also suggested the level of fibre treatment plays an important role in determining the load and absorbed energy to perforation, while the matrix has little influence. Sutherland and Soares (101) conducted low velocity impact tests to investigate the effect of two types of thermosetting matrix in GFRP composites. GFRP/epoxy and GFRP/polyester composites were used in this study. They found that the polyester laminate absorbed a higher impact energy than the epoxy-based composite. Further, back-face fibre damage and front-face delamination were more severe in the GFRP/epoxy than in the GFRP/polyester composites, which could be due to the brittleness of the epoxy resin.

It is clear that matrix properties play an important role in determining the impact performance of a composite laminate. Thermoplastics are more resistant to impact damage than most thermosetting matrix composites.

### **2.3.5.3 The Effect of Fibre-Matrix Interface**

A number of studies have shown that the interface between the fibre and matrix can significantly affect the mechanical properties and energy absorption-capability of a composite. Yeung and Broutman (102) studied the effect of varying the glass-resin interfacial strength on the impact resistance of glass fibre reinforced epoxy and polyester laminates using a Charpy impact test. It was found that the initiation energy for both the epoxy and polyester laminates increased with increasing interlaminar shear strength (ILSS). The maximum energy absorbed for the epoxy and the polyester laminates was nearly identical. Kevlar fibre reinforced composites show a poor level of interfacial adhesion between the Kevlar fibre and the matrix resin (103). Park *et. al.* (103) conducted low velocity impact tests

using a drop-weight impact tower to study the effect of fibre treatment. The chemical treatment used was a phosphoric ( $\text{H}_3\text{PO}_4$ ) acid solution. The interfacial properties of the treated composites were studied by determining the shear strength, the critical stress intensity ( $K_{Ic}$ ) and the fracture energy ( $G_{Ic}$ ). They found that a chemical treatment with a  $\text{H}_3\text{PO}_4$  solution significantly increased the degree of interfacial adhesion between the fibre and the matrix, resulting in an improved interfacial strength and fracture energy. Kessler and Bledzki (104) investigated the influence of fibre/matrix adhesion on the impact behaviour of cross-ply glass/epoxy laminates. Glass fibres with two different treatments, silane and polyethylene dispersions, embedded in epoxy matrix systems and subjected to low velocity impacts were investigated. They found that the laminate with a silane fiber/matrix treatment was three times more damage resistant than one with a polyethylene treatment. Instrumented impact tests were employed by Hirai *et. al.* (105) to study the impact response of vinyl-ester-matrix composites reinforced with a woven E-glass fabric following a silane surface treatment. They showed that the silane concentration improved the damage resistance and damage tolerance of the laminates. Cantwell *et. al.* (106) conducted low velocity impact tests to investigate the effect of adding a low molecular weight modifying agent to a glass fibre reinforced polypropylene in order to improve its interfacial strength. Significant improvements in the drop-weight impact resistance of the material were also observed following the addition of a modifying agent (106).

In this section, the influence of the fibre matrix interface on the low velocity impact response of composite materials has been elaborated. A stronger interface between the fibre and the matrix leads to an improved interfacial strength, fracture energy and impact performance under low velocity impact loading.

## 2.4 Failure Modes in Composite Laminates Subjected to Low Velocity Impact

The mode of failure in a composite following low velocity impact is important in which it influences not only the impact resistance but also the residual strength. Matrix damage, delamination and fibre failure are common damage mechanisms in composite laminates. The failure mechanisms observed in composites subjected to low velocity impact will be discussed in the following sections.

### 2.4.1 Matrix Damage

Matrix failure occurs parallel to the fibres due to tension, compression and shear loads. Joshi and Sun (5) observed matrix cracking and delamination between the plies of a carbon/epoxy, as shown in **Figure 2.16**. They reported that shear crack initiation at the edge of the point of contact with the crack being inclined at approximately  $45^\circ$ . These cracks are due to large transverse shear stresses through the composite. The crack in the bottom layer was termed a bending crack, initiated by the locally-high bending stresses.

This text box is where the unabridged thesis included the following third party copyright material:

Joshi SP, Sun CT. Impact induced fracture in a laminated composite. Journal of Composite Materials. 1985;19(1):51-66.

**Figure 2.16** Transverse section of a carbon/epoxy (5).

Cantwell and Morton (72) reported that increasing the effective size of the target by varying the specimen length resulted in a change in the initial mode of failure. Shorter and stiffer beams failed initially as a result of the higher contact stresses induced by shear cracks under

the impactor. In addition, longer and more flexible specimens failed in a bending mode between the lowermost fibres. **Figure 2.17** shows the variation of the first damage threshold with beam length for CFRP laminates. Greater detail concerning the mechanisms of matrix cracking in glass/epoxy and carbon/epoxy laminates were presented by Liu and Malvern (4) and Wu and Springer (86) respectively.

This text box is where the unabridged thesis included the following third party copyright material:

Cantwell WJ, Morton J. Geometrical effects in the low velocity impact response of CFRP. *Composite Structures*. 1989;12(1):39-59.

**Figure 2.17** *Variation of the first damage threshold with beam length for ( $0^\circ, \pm 45^\circ$ ) CFRP laminates (72).*

### 2.4.2 Delamination

A delamination is a crack that runs between plies having different fibre orientations (5, 86) as shown in **Figure 2.18**. Delamination can dramatically reduce the post-impact compressive strength of the laminate (96). Joshi and Sun (5) found that for  $[0^\circ/90^\circ/0^\circ]$  laminates, the delaminated zone had the shape of a peanut. They argued that delamination was a result of the bending stiffness mismatch between adjacent layers. Similar results were reported by Wu and Springer (86). The change in fibre orientation between the layers introduced an oblong-shaped delamination region, with the major axis of delamination being nearly parallel to the

fibre direction in the lowest ply (86). These results agree with those made by Davies *et al* (107) who observed a series of peanut-shaped overlapping delaminations aligned in the fibre direction of a  $[0/+45/-45]_s$  carbon/epoxy composite, as shown in **Figure 2.18**.

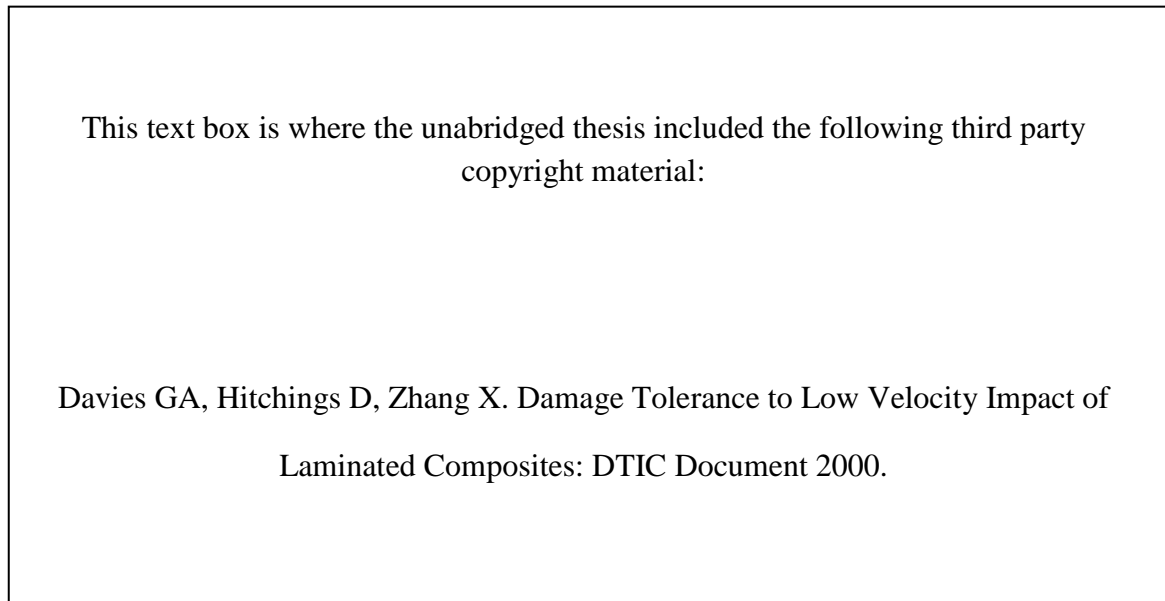


**Figure 2.18** *Delamination patterns through the thickness of a carbon/epoxy laminate following low velocity impact loading (107).*

A number of attempts have been made to experimentally determine the delamination initiation load. **Table 2.2** shows the results from two experimental investigations to evaluate the delamination initiation load for five types of glass/epoxy and three carbon/epoxy laminates. From **Table 2.2**, it is clear that placing the  $90^0$  ply on the outer surface of the laminate reduced the load to initiate delamination.

Composite laminate	Stacking Sequence	Delamination Initiation Load (N)	Reference
Glass/epoxy	[0 <sub>4</sub> /15 <sub>4</sub> /0 <sub>4</sub> ]	5300	(108)
Glass/epoxy	[0 <sub>3</sub> /15 <sub>6</sub> /0 <sub>3</sub> ]	5711	(108)
Glass/epoxy	[0 <sub>3</sub> /15 <sub>8</sub> /0 <sub>3</sub> ]	5914	(108)
Glass/epoxy	[0 <sub>2</sub> /15 <sub>2</sub> /0/15] <sub>s</sub>	6368	(108)
Glass/epoxy	[[0/15 <sub>3</sub> ]] <sub>s</sub>	6696	(108)
Carbon/epoxy	[0/90 <sub>12</sub> /0]	5115	(109)
Carbon/epoxy	[90 <sub>6</sub> /0 <sub>2</sub> /90 <sub>6</sub> ]	2113	(109)
Carbon/epoxy	[90 <sub>2</sub> /0 <sub>2</sub> /90 <sub>2</sub> ]	5339	(109)

**Table 2.2** *The effect of the stacking sequence of glass/epoxy and carbon/epoxy laminates on the delamination initiation load.*

One of the simplest methods for predicting the onset of impact-induced delamination was proposed by Davies *et. al.* (110). They concluded that the onset of delamination in composite laminates occurred at a critical threshold force, dependent on the thickness of the specimen, this is given by the following equation:

$$P_m^2 = \frac{8\pi^2 E h^2}{9(1-\nu^2)} G_{IIc} \quad [2.8]$$

where  $P_m$  is the threshold load,  $E$  and  $\nu$  are the in-plane modulus and the Poisson's ratio for the laminate,  $h$  is the thickness and  $G_{IIc}$  is Mode II interlaminar fracture toughness. Above the threshold force, the size of the delamination area increases suddenly with increasing impact energy.

### 2.4.3 Fibre Failure

Splitting, fibre pull-out and fibre fracture are the most common fibre-related failure mechanisms under low velocity impact testing (7). Fibre failure occurs under the impactor due to the high stress field and indentation effects. It is governed by the shear force induced by the impactor and the high bending stresses in the non-impacted face. Fibre failure loads in laminates reported in various investigations is tabulated in **Table 2.3**. From the table, it can be seen that increasing the thickness of a unidirectional laminate decreases the load to induce failure. In contrast, increasing the number of  $90^\circ$  plies of surface layers decreased the failure load. Sun and Jen (111) observed that transverse matrix cracking in cross-ply laminates can significantly reduce the laminate strength. They noted that thicker  $90^\circ$  plies containing larger transverse matrix cracks could cause higher stress concentrations on the  $0^\circ$  plies, resulting in further reductions in the laminate strength.

Composite laminate	Stacking Sequence	Average Thickness (mm)	Failure load (kN)	Reference
Carbon/epoxy	$[0_2]$	0.25	16	(111)
Carbon/epoxy	$[0_4]$	0.51	29	(111)
Carbon/epoxy	$[0_6]$	0.76	43	(111)
Carbon/epoxy	$[90_2/0_2/90_2]$	0.76	14	(109)
Carbon/epoxy	$[90_4/0_2/90_4]$	1.27	11	(109)
Carbon/epoxy	$[90_6/0_2/90_6]$	1.78	10	(109)

**Table 2.3** *The effect of thickness and stacking sequence on the load to introduce fibre failure in carbon/epoxy laminates.*

## 2.5 Low Velocity Impact Response of Sandwich Structures

Lightweight sandwich panels generally consist of strong, stiff and thin composite skins and a soft and thick core. Low velocity impact on a sandwich structure can often result in damage to the skins, the core material and the skin-core interface. Such damage is very difficult to detect by the naked eye and cause a significant reduction in the strength and stiffness of the material. This section discusses the various factors that have a significant influence on the impact response of sandwich structures.

### 2.5.1 Effect of Impactor Geometry

The effect of the impactor shape and diameter on the low velocity impact response of sandwich structures has been investigated experimentally using both flat and hemispherical indentors (112-114). Raju and co-authors (113) investigated the damage characteristics of carbon/epoxy/aluminium honeycomb sandwich structures using a drop-weight impact tower. They showed that a smaller diameter impactor produced damage in the form of matrix cracking and fibre fracture, while larger diameter impactors produced large amounts of core crushing until the onset of fracture in the skin. The peak force was found to be independent of impactor size and facesheet type. Bernard and Lagace (114) studied the influence of impactor diameter on the damage resistance of aluminium honeycomb, aramid/phenolic honeycomb and polymethacrylimide (PMI) foam core panels with carbon/epoxy facesheets using both steel and acrylic projectiles. They concluded that the damage size was a function of the impactor diameter and observed that damage never exceeded twice the impactor diameter. The indentation failure behaviour of honeycomb core sandwich panels was studied by Tsotsis and Lee (115) by examining the effect of indenter size on load transfer from the top skin to the core. Panels with different GFRP/epoxy skins and aramid cores were used. They showed that doubling the indenter diameter from 6.35 to 12.7 mm almost doubled the initial threshold load. Extensive experimental work to study the effect of indenter nose shape during quasi-static loading was conducted by Zhou and Mall (116). The damage characteristics of



aluminium honeycomb sandwich panels in bending were investigated using both hemispherical and flat-ended indentors. The threshold and ultimate load, as well as the initial slope, increased when the indenter nose shape was changed from hemispherical to flat-ended, due to a greater stress concentration around the edge of the impactor (116). Johnson and Li (117) examined the quasi-static indentation response of sandwich structures with five different densities of PMI foam core under loading from a conical, truncated, flat-face and hemispherical indenter. They reported that the diameter of the indenter has little influence on the stiffness of the sandwich panels; in contrast, the diameter has a significant effect on the ultimate failure of the face. The largest damage areas were observed for flat and truncated indentors, while the smallest damage areas were observed for conical indentors (117). Sadhigi and Pouriaeyali (118) reported that increasing the indenter diameter increases the contact stiffness of the composite laminate. They conducted quasi-static and low velocity impact tests on GFRP/epoxy laminates with polyurethane (PU) and PVC cores using 10 and 20 mm hemispherical indenter.

### 2.5.2 Effect of Impact Velocity

For low velocity impact loading, the magnitude of the impact velocity influences the contact force and deflection of the sandwich structure. Lee *et. al.* (35) showed that the peak force increased with increasing impact velocity. However, the impact force for sandwich structures was not sensitive to the contact duration. Mines *et. al.* (119) conducted static and dynamic perforation tests on sandwich structures with woven glass vinylester skins and a Coremat core as well as GFRP with a honeycomb core. They used a standard servo-hydraulic test machine and a drop-weight impact tower. They suggested using high density and multiple layer skins for improving the perforation resistance of sandwich structures.

### 2.5.3 Effect of Skin Type, Thickness and Stacking Sequence

The impact resistance of sandwich structures is greatly influenced by the facesheet type, thickness and stacking configuration. Mohan *et. al.* (120) conducted quasi-static indentation tests on aluminium, stainless steel, alumina ( $\text{Al}_2\text{O}_3$ ) and CFRP skins with aluminium foam cores using hemispherical and flat-ended indentors. They found that increasing the thickness of the facesheet increased the energy absorbed by the sandwich structure. Sandwich structures with stainless steel facesheets offered a higher energy-absorbing capacity compared to other types of skin. Park *et. al.* (121) used a scanning acoustic microscope to evaluate the damage resistance of sandwich structures, composed of a honeycomb core and carbon/epoxy and glass/epoxy facesheets. Delamination in the facesheets was peanut-shaped and the results are shown in **Figure 2.19**.

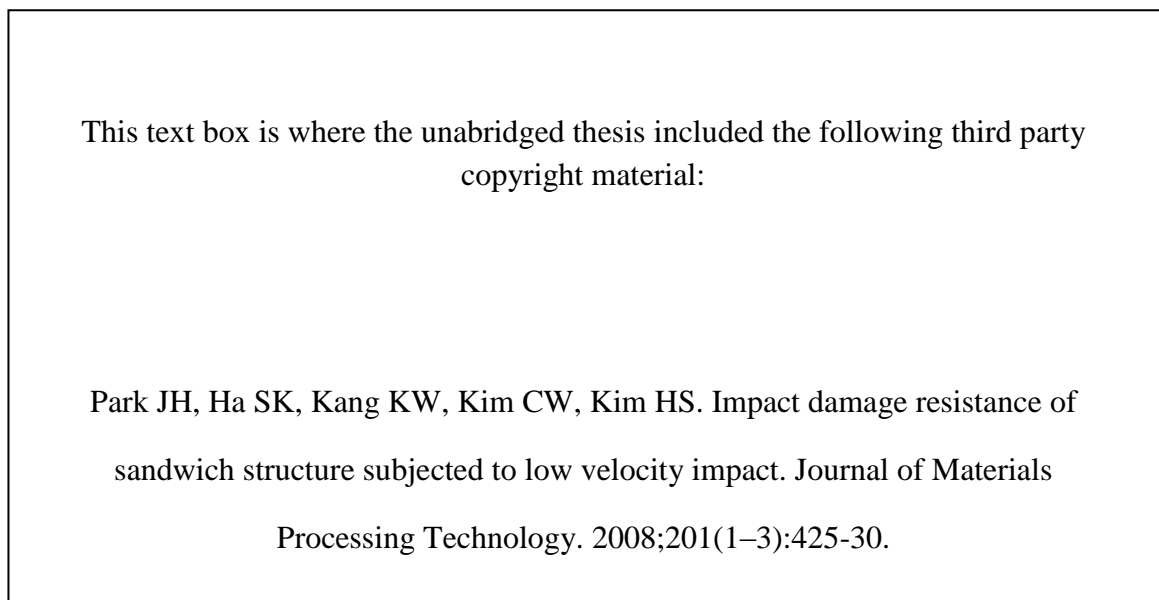


**Figure 2.19** The variation of damage area with impact energy for honeycomb core sandwich structures with (a) carbon/epoxy and (b) glass/epoxy skins with incident impact energy (121).

Shuaeib and Soden (122) investigated the indentation response of panels with GFRP/polyester skins and PVC foam cores and found that increasing the skin thickness from 3.3 to 5.7 mm roughly doubled the failure load. Also, by increasing the skin thickness, the deflection at failure increased, as did the energy to cause failure (122). **Figure 2.20** shows the load-displacement traces for sandwich structures with different skin thicknesses.

This text box is where the unabridged thesis included the following third party copyright material:

Shuaeib FM, Soden PD. Indentation failure of composite sandwich beams.  
Composites Science and Technology. 1997;57(9–10):1249-59.

**Figure 2.20** *Load versus indenter displacement for specimens having different skin thicknesses, all of these specimens had 25 mm thick PVC foam cores (122).*

Extensive experimental work on the quasi-static and low velocity impact response of honeycomb sandwich structures with different thicknesses of skin was studied by Herup and Palazatto (123). They used carbon/epoxy skins with a honeycomb core and found that increasing the facesheet thickness increased the load drop after the peak load. A higher damage resistance and absorbed energy for the thick laminates were observed. Quasi-static tests on a honeycomb sandwich structure with cross-ply carbon/epoxy skins were conducted by Zhou *et. al.* (116). They showed that both the threshold load and ultimate loads were

sensitive to skin thickness. Changing the skin thickness not only changed the flexural rigidity of the sandwich panels, but also the load transfer between the top skin and the adjacent core. Increasing the thickness of the skin increased the shear stiffness and bending stiffness of the structures, thereby affecting the resulting damage mechanisms.

Sadhigi and Pouriaevali (118) showed that under low velocity impact, increasing the skin stiffness decreased the loading time and impactor displacement, whilst increasing the impact force under elastic impact. Park *et. al.* (121) conducted low velocity impact tests to investigate the influence of the skin stiffness and found increasing the stiffness of skin increased the peak load during impact, as shown in **Figure 2.21**. Similar results were reported by Raju *et. al.* (113) and Anderson and Madensi (124). The increase in peak load with incident impact energy was observed to be non-linear. They suggested that the variation in local stiffness, due to the location of the impact event, variability in both the facesheet and core properties might influence these trends (113). For example, if the impact point coincides with a node in the honeycomb core, giving a higher local indentation stiffness, the force tended to be higher than for other locations.

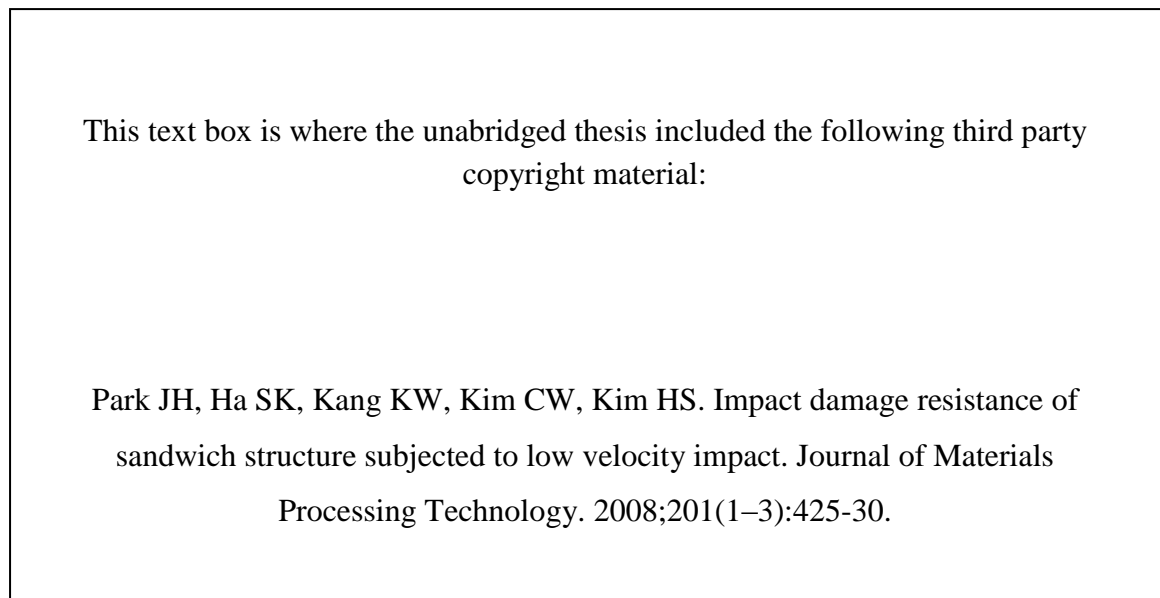


**Figure 2.21** Summary of the variation of the maximum peak load with impact energy for four sandwich structures (121).

Shih and Jang (125) showed that the impact resistance of composite sandwich panels with tough facesheets (PET and PE) was controlled by the properties of the facesheets with the density of the foam core being less important. The impact failure mechanisms in sandwich panels based on less tough facesheets were found to change from a facesheet-dominated to foam core-dominated behaviour, when the density of the PVC foam core increased from low to high. The effect of the face stacking sequence of a sandwich structures on the level of delamination area was studied by Kim and Jun (126). The sandwich structure were made of carbon/epoxy facesheets and a honeycomb core. They observed that a  $[0/45/90/-45]_S$  layup offered a superior damage resistance than a  $[45/-45/0/90]_S$  lay-up.

#### 2.5.4 Effect of the Core

The effect of varying the properties of the core of the sandwich structure on its low velocity impact response were studied by Akay and Hanna (127). They examined the impact perforation of sandwich panels based on a carbon/epoxy skin and either on aramid/phenolic honeycomb or a PMI foam core. They found that the PMI foam core offered a higher energy absorption than the aramid/phenolic honeycomb. They suggested the core provides considerable support to the facesheet and improves the impact resistance and reduces crack propagation in the skin. Core damage mechanisms in aluminium and aramid/phenolic honeycombs were investigated by Bernard and Lagace (114). The aluminium honeycomb had a greater number of damaged cells than those in the aramid/phenolic honeycomb for the same energy level and core thickness. In order to enable a comparison with the PMI foam, the number of buckled cells in the aramid/phenolic honeycomb was converted into a crack length by multiplying the diameter of one honeycomb cell by the number of buckled cells. It shown that damage in PMI foam core was greater than in the aramid/phenolic honeycomb core. Nettles and Hodge (128) examined impact damage in glass/phenolic and aluminium honeycomb cores sandwich structures following low velocity impact. They found that the

number of cell walls buckled in the aluminium honeycomb was over double that in a glass/phenolic honeycomb. Energy absorption in an aluminium foam and PVC foam sandwich structures was investigated by Compston *et. al.* (129) using a double pendulum impact tester. The energy absorption of each structure was similar, but significant differences in damage modes were observed. Damage in the polymer foam was localised and characterised by matrix cracking and core indentation at low energies and composite skin fracture and core crushing at higher energies. In contrast, the aluminium foam core samples experienced some foam cell crushing at all impact energies and minor composite skin buckling damage at the higher energies.

The effect of varying core density following low velocity impact was studied by Caprino and Teti (130). Sandwich structures with three densities of PVC foam core and thin glass/polyester facings were examined. They found that high density foam cores offer higher local rigidities, leading to an increase in the maximum contact force. Similar results were reported by Zhou *et. al.* (116) following quasi-static loading on aluminium honeycomb sandwich structures. This behaviour highlighted the potential advantage of stronger cores in protecting the facings against impact damage. Caprino and Teti (130) suggested that damage development and residual strength after impact were independent of core density. This observation supports the statement that the best performance under impact loading is offered by high strength core materials (130).

## 2.6 Failure Modes in Sandwich Structures

Damage development in sandwich structures during impact is strongly dependent on the skin thickness (131), the indenter shape (112), indenter diameter (113), core thickness (113) and core density (119, 131). Mines *et. al.* (119) concluded that core crushing dominates the overall energy absorption process. The failure modes in PVC core sandwich structures with

glass/epoxy skins under static and dynamic loading conditions were investigated by Lim *et. al.* (131). They found that thin faces and high density cores lead to compressive fracture in the top surface facing. **Figure 2.22** shows the change in failure mode with varying face thickness and core density. They concluded that increasing the skin thickness and density changes the failure mode in the sandwich structures from skin failure, tensile cracking in the core and delamination to core shear.

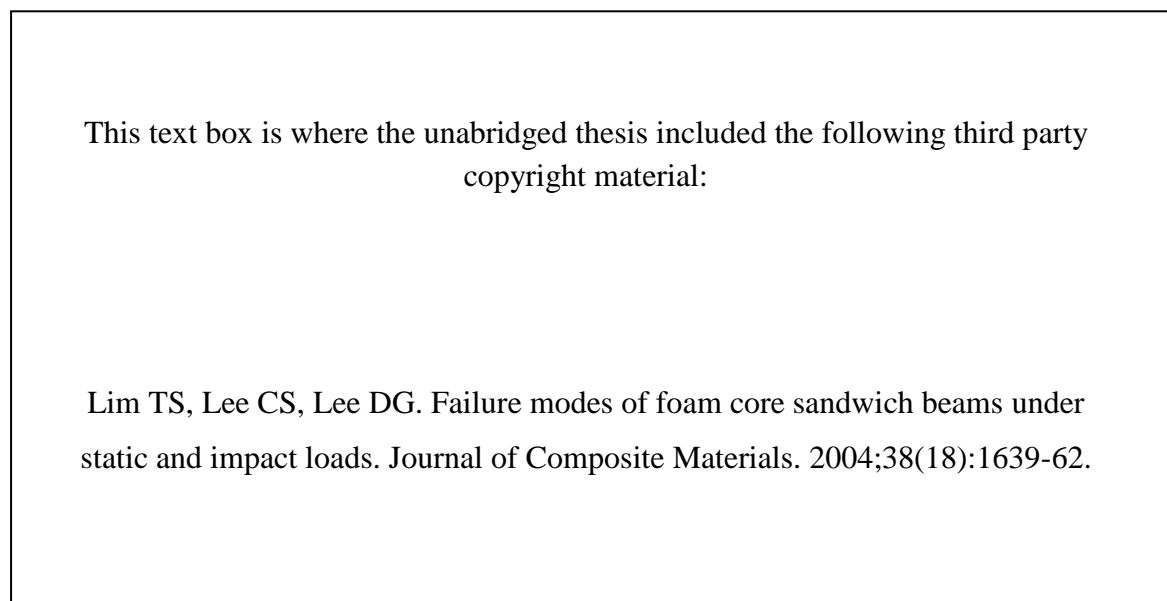


**Figure 2.22** *Damage progression in PVC core sandwich structures following three point bend testing with (a) varying skin thickness and (b) varying core density (131).*

A number of attempts have been made to investigate the process of impact damage development in sandwich structures under quasi-static loading (112), dynamic loading (113)

and at rates between these extremes (119). Zhou *et. al.* (112) showed that in general, the force-displacement response associated with a flat-ended indenter can be divided into three stages, as shown in **Figure 2.23**. The initial damage mechanism involves extensive core crushing over a wider region, with a significant reduction in slope but with no top skin damage. This is followed by top skin delamination with continued core crushing, marked as secondary damage. The significant steepening of the slope after secondary damage was due to stretching of the delaminated top skin. Shear-out of the top skin marked the complete loss of the load-bearing capacity of the sandwich panels. However, under loading by a hemispherical indenter, initial damage involved a combination of core crushing and a small cone-shaped delamination in the top skin, due to the local stress concentration associated with the indenter. This was followed by continued core crushing, a significant slope reduction and by the propagation of delamination in the top skin.

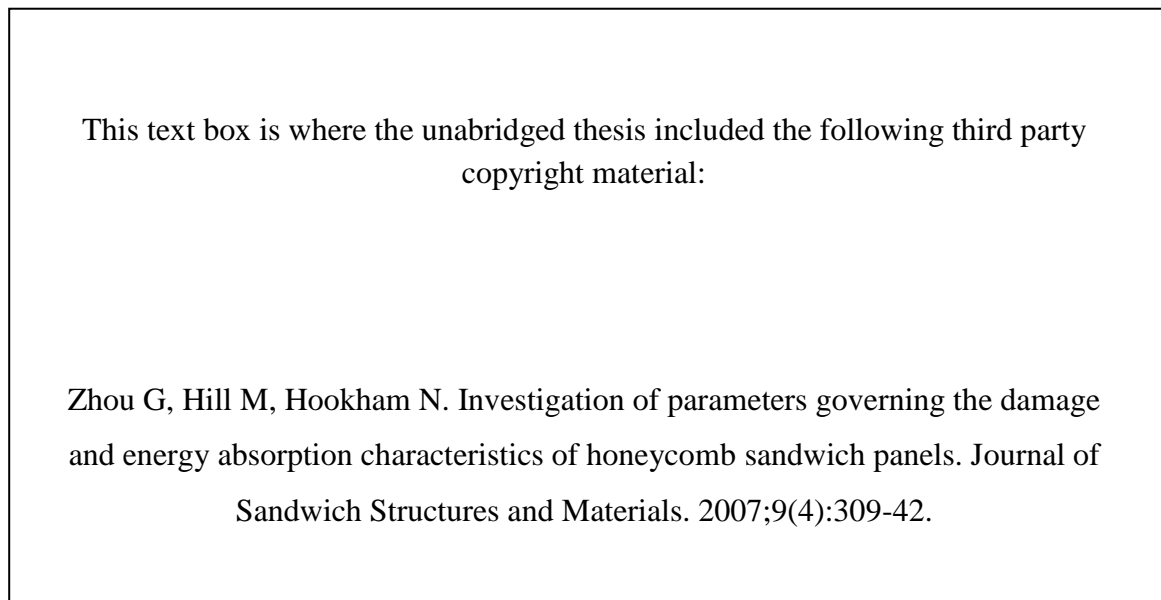


**Figure 2.23** *Typical load-displacement traces for aluminium honeycomb sandwich structures following quasi-static loading (112).*



Lin and Hoo Fatt (132) conducted the quasi-static and low-velocity perforation tests on composite sandwich panels with woven E-glass/epoxy prepreg facesheets and an aluminum honeycomb core. They showed that damage progression occurred in three-stages, as shown in **Figure 2.24**. Stages 1 to 3 can be described as: perforation of the top facesheet, the core, and the bottom facesheet, respectively.

This text box is where the unabridged thesis included the following third party copyright material:

Lin C, Fatt MSH. Perforation of sandwich panels with honeycomb cores by hemispherical nose projectiles. *Journal of Sandwich Structures and Materials*. 2005;7(2):133-72.

**Figure 2.24** *Three-stage perforation process in a honeycomb sandwich panel (132).*

## 2.7 The Analytical Perforation Model

A number of perforation models have been developed in order to predict the perforation resistance of both metallic and composite materials. Metallic materials have been reviewed by Johnson (133), Backman and Goldsmith (134) and Corbett (135), while Abrate (8) reviewed composite materials. Virostek *et. al.* (136) investigated the high velocity impact response of aluminium, steel, Lexan, nylon, ceramic and Kevlar plates using conical and hemispherical indentors. They measured the load-displacement histories of the plates under different angles of incidence. A simple model was developed to predict perforation of the plates by both types of projectile at oblique angles, and comparisons were made with the measured force histories. It was found that the peak force under normal impact was relatively independent of the initial projectile velocity when perforation occurred. For tests at velocities below the ballistic limit, the maximum forces were approximately proportional to the initial velocity. Lee and Sun (137) developed a quasi-static model to simulate the penetration process in carbon/epoxy laminates. Delamination and transverse plugging were identified as the major damage mechanisms during perforation. Impact test results also showed that the dynamic failure modes were very similar to those obtained under static loading. This level of close agreement in damage patterns highlighted the possibility of using a static penetration model to characterise the dynamic perforation process. This model was then successfully used to model the results from dynamic impact testing. Following this, Sun and Potti (19) developed a simple static energy model to predict the ballistic limit of thicker laminates impacted by a blunt projectile.

Ursebach *et. al.* (138) developed an analytical model for perforation of CFRP laminates by a hemispherical indenter. The model was capable of estimating the delamination size and the effective bending stiffness of the laminate. The predicted delamination sizes for various laminate thicknesses were successfully correlated with those measured using C-scan images.

Zhu *et. al.* (139) used a finite difference analysis to model the perforation behaviour of Kevlar 29/polyester laminates plates by a conical projectile. The perforation process was divided into three stages: indentation, perforation and projectile exit. The analysis consisted of both global and local deformations. A comparison of the predicted ballistic limits with test results showed good agreement, where the ballistic limit was found to vary linearly with laminate thickness. Goldsmith *et. al.* (140) proposed a perforation model based on energy absorption due to global plate deflections, fibre breakage, delamination, the formation and bending of petals and friction between the projectile and the plate. They found that the delamination size was up to four times the size of the projectile diameter.

Dorey (141) suggested that under high velocity impact loading, most of the incident energy resulted in shear-out and perforation of the composite. He proposed that the perforation energy of a composite laminate is given by:

$$E_{perforation} = \pi \gamma t d \quad [2.9]$$

where  $\gamma$  is the fracture energy of the composite,  $d$  is diameter of the projectile and  $t$  is thickness of the laminate.

Cantwell and Morton (142) developed a simple analytical model for the prediction of the perforation energy of CFRP under low and high velocity impact condition by a spherical projectile. Here, the energy required for target shear-out was estimated by multiplying the transverse fracture energy by the surface area of the calculated shear zone. They found that the model can predict not only the perforation energy for thinner laminates, but also the effect of beam thickness and beam length.

Wen and co-authors (143-145) developed a simple equation for predicting the perforation resistance of fibre reinforced polymer laminates and sandwich panels with foam cores by rigid projectiles. The results of the the penetration and perforation tests on the composite laminates and sandwich panels using flat-faced, ogival, hemispherical and conical indentors

under quasi-static, drop-weight and ballistic impact conditions with impact velocities up to 305 m/s were reported. The load-displacement characteristics under quasi-static loading were presented and the energies corresponding to different degrees of damage were calculated. The fracture patterns observed in sandwich panels loaded dynamically were compared with those observed in identical panels subjected to quasi-static loading. The ballistic limits and perforation energies were determined and a classification of the responses was deduced from the test data. The experimental evidence showed that ballistic impact on fibre-reinforced polymer laminates and sandwich panels can be categorised into low velocity impact (global) and wave-dominated (localised) responses.

Lin and Hoo Fatt (132) proposed an analytical energy-balance model for the ballistic limit of an aluminum sandwich plate subjected to normal impact by hemispherical and blunt projectiles. They also developed a perforation model for sandwich panels with polymer foam and aramid paper honeycomb cores (146) impacted by hemispherical and flat-end projectiles. The results were in good agreement with the experimental data.

## 2.8 Summary

In summary, a review of the background of the indentation parameters of the composite laminate and sandwich structures has been presented. It is clear that the contact stiffness ' $C$ ' and the parameter ' $n$ ' are dependent on the indenter diameter, laminate thickness and rate of loading. Following this, a number of parameters that influence the impact response of composite laminates, including the impactor diameter, loading rate, geometry and material constituents of the panel have been reviewed. This chapter has briefly discussed various factors including skin thickness, core density and the velocity of the impactor all of which have a significant influence on the impact response of sandwich structures. This chapter has also briefly examined some of the analytical perforation models which will be used to predict

the perforation threshold of the polymer foam based sandwich structures. The following chapter describes the experimental approaches used to investigate the impact response of sandwich structures.

## 2.9 References

1. Shivakumar KN, Elber W, Illg W. Prediction of low-velocity impact damage in thin circular laminates. *AIAA Journal*. 1985;23(3):442-9.
2. Sjoblom PO, Hartness JT, Cordell TM. On low-velocity impact testing of composite materials. *Journal of Composite Materials*. 1988;22(1):30-52.
3. Cantwell WJ, Morton J. Comparison of the low and high velocity impact response of CFRP. *Composites*. 1989;20(6):545-51.
4. Liu D, Malvern LE. Matrix cracking in impacted glass/epoxy plates. *Journal of Composite Materials*. 1987;21(7):594-609.
5. Joshi SP, Sun CT. Impact induced fracture in a laminated composite. *Journal of Composite Materials*. 1985;19(1):51-66.
6. Zukas J. Theory and experimental. Ballistic Research Laboratory Technical Report. ARBL-TR-02271;1980.
7. Cantwell WJ, Morton J. The impact resistance of composite materials - a review. *Composites*. 1991;22(5):347-62.
8. Abrate S. Impact on the composite structures. Cambridge: Cambridge University Press; 1998.
9. Seyed Yaghoubi A, Liu Y, Liaw B. Stacking sequence and geometrical effects on low-velocity impact behaviors of GLARE 5 (3/2) fiber-metal laminates. *Journal of Thermoplastic Composite Materials*. 2012;25(2):223-47.
10. Ghelli D, Minak G. Low velocity impact and compression after impact tests on thin carbon/epoxy laminates. *Composites Part B: Engineering*. 2011;42(7):2067-79.
11. Chen P, Huang F, Dai K, Ding Y. Detection and characterization of long-pulse low-velocity impact damage in plastic bonded explosives. *International Journal of Impact Engineering*. 2005;31(5):497-508.

12. Hosur MV, Vaidya UK, Ulven C, Jeelani S. Performance of stitched/unstitched woven carbon/epoxy composites under high velocity impact loading. *Composite Structures*. 2004;64(3):455-66.
13. Czarnecki GJ. Estimation of the V50 using semi-empirical (1-point) procedures. *Composites Part B: Engineering*. 1998;29(3):321-9.
14. Czarnecki GJ. The significance of laminate spallation generated by high-velocity spherical metallic impactors. *Composites Engineering*. 1994;4(3):287-93,95-97.
15. Jenq ST, Wang SB, Sheu LT. A model for predicting the residual strength of GFRP laminates subject to ballistic impact. *Journal of Reinforced Plastics and Composites*. 1992;11(10):1127-41.
16. Hoo Fatt MS, Lin C, Revilock DM, Hopkins DA. Ballistic impact of GLARE™ fiber-metal laminates. *Composite Structures*. 2003;61(1):73-88.
17. Abdullah MR, Cantwell WJ. The impact resistance of polypropylene-based fibre-metal laminates. *Composites Science and Technology*. 2006;66(11):1682-93.
18. Jacobs MJN, Van Dingenen JLJ. Ballistic protection mechanisms in personal armour. *Journal of Materials Science*. 2001;36(13):3137-42.
19. Sun CT, Potti SV. A simple model to predict residual velocities of thick composite laminates subjected to high velocity impact. *International Journal of Impact Engineering*. 1996;18(3):339-53.
20. Wen HM. Predicting the penetration and perforation of targets struck by projectiles at normal incidence. *Mechanics of Structures and Machines*. 2002;30(4):543-77.
21. Wen HM. Penetration and perforation of thick FRP laminates. *Composites Science and Technology*. 2001;61(8):1163-72.
22. Caprino G, Langella A, Lopresto V. Indentation and penetration of carbon fibre reinforced plastic laminates. *Composites Part B: Engineering*. 2003;34(4):319-25.
23. Swanson SR. Limits of quasi-static solutions in impact of composite structures. *Composites Engineering*. 1992;2(4):261-7.

24. Olsson R. Mass criterion for wave controlled impact response of composite plates. *Composites Part A: Applied Science and Manufacturing*. 2000;31(8):879-87.
25. Olsson R. Closed form prediction of peak load and delamination onset under small mass impact. *Composite Structures*. 2003;59(3):341-9.
26. Tabor D. *The hardness of metals*: Oxford University Press; 1951.
27. Yang SH, Sun CT. Indentation law for composite laminates. *ASTM STP*. 1982;787:425-49.
28. Tan TM, Sun CT. Use of statical indentation laws in the impact analysis of laminated composite plates. *Journal of Applied Mechanics*. 1985;52:6.
29. Wu E, Yen CS. The contact behavior between laminated composite plates and rigid spheres. *Journal of Applied Mechanics*. 1994;61:60.
30. Wu E, Shyu K. Response of composite laminates to contact loads and relationship to low-velocity impact. *Journal of Composite Materials*. 1993;27(15):1443-64.
31. Sutherland LS, Soares CG. Contact indentation of marine composites. *Composite Structures*. 2005;70(3):287-94.
32. Lee CY, Liu D. Effect of impact velocity on the indentation of thick composite laminate. *Experimental Techniques*. 2009;33(4):59-64.
33. Zhou DW, Stronge WJ. Low velocity impact denting of HSSA lightweight sandwich panel. *International Journal of Mechanical Sciences*. 2006;48(10):1031-45.
34. Koller MG. Elastic impact of spheres on sandwich plates. *Zeitschrift für Angewandte Mathematik und Physik (ZAMP)*. 1986;37(2):256-69.
35. Lee LJ, Huang KY, Fann YJ. Dynamic Responses of Composite Sandwich Plate Impacted by a Rigid Ball. *Journal of Composite Materials*. 1993;27(13):1238-56.
36. Sburlati R. The effect of a slow impact on sandwich plates. *Journal of Composite Materials*. 2002;36(9):1079-92.
37. Soden PD. Indentation of composite sandwich beams. *The Journal of Strain Analysis for Engineering Design*. 1996;31(5):353-60.



38. Akil Hazizan M, Cantwell WJ. The low velocity impact response of foam-based sandwich structures. *Composites Part B: Engineering*. 2002;33(3):193-204.
39. Kiratisaevee H, Cantwell WJ. Low-velocity impact response of high-performance aluminum foam sandwich structures. *Journal of Reinforced Plastics and Composites*. 2005;24(10):1057-72.
40. Rizov V. Indentation of foam-based polymer composite sandwich beams and panels under static loading. *Journal of Materials Engineering and Performance*. 2009;18(4):351-60.
41. Rizov V, Shipsha A, Zenkert D. Indentation study of foam core sandwich composite panels. *Composite Structures*. 2005;69(1):95-102.
42. Rizov V. Elastic-plastic response of structural foams subjected to localized static loads. *Materials and Design*. 2006;27(10):947-54.
43. Whisler D, Kim H. Effect of impactor radius on low-velocity impact damage of glass/epoxy composites. *Journal of Composite Materials*. 2012.
44. Kim SJ, Goo NS. Dynamic contact responses of laminated composite plates according to the impactor's shapes. *Computers and Structures*. 1997;65(1):83-90.
45. Finn SR, He YF, Springer GS. Delaminations in composite plates under transverse impact loads—experimental results. *Composite Structures*. 1993;23(3):191-204.
46. Amaro AM, Reis PNB, Magalhães AG, de Moura MFSF. The Effect of the Impactor Diameter and Boundary Conditions on Low Velocity Impact Composites Behaviour. *Applied Mechanics and Materials*. 2007;7:217-22.
47. Mines RAW, Roach AM, Jones N. High velocity perforation behaviour of polymer composite laminates. *International Journal of Impact Engineering*. 1999;22(6):561-88.
48. Mitrevski T, Marshall IH, Thomson R, Jones R, Whittingham B. The effect of impactor shape on the impact response of composite laminates. *Composite Structures*. 2005;67(2):139-48.

49. Mili F. Effect of the Impact Velocity on the Dynamic Response of E-Glass/Epoxy Laminated Composites. *Arabian Journal for Science and Engineering*. 2012;37(2):413-9.
50. Aggour H, Sun CT. Finite element analysis of a laminated composite plate subjected to circularly distributed central impact loading. *Computers and Structures*. 1988;28(6):729-36.
51. Breen C, Guild F, Pavier M. Impact of thick CFRP laminates: the effect of impact velocity. *Composites Part A: Applied Science and Manufacturing*. 2005;36(2):205-11.
52. Aliyu AA, Daniel IM. Effects of strain rate on delamination fracture toughness of graphite/epoxy. *Delamination and debonding of materials, ASTM STP*. 1985;876:336-48.
53. Smiley AJ, Pipes RB. Rate effects on mode I interlaminar fracture toughness in composite materials. *Journal of Composite Materials*. 1987;21(7):670-87.
54. Gillespie JW, Carlsson LA, Smiley AJ. Rate-dependent mode I interlaminar crack growth mechanisms in graphite/epoxy and graphite/PEEK. *Composites Science and Technology*. 1987;28(1):1-15.
55. Mall S, Law GE, Katouzian M. Loading rate effect on interlaminar fracture toughness of a thermoplastic composite. *Journal of Composite Materials*. 1987;21(6):569-79.
56. Kusaka T, Hojo M, Mai YW, Kurokawa T, Nojima T, Ochiai S. Rate dependence of mode I fracture behaviour in carbon-fibre/epoxy composite laminates. *Composites Science and Technology*. 1998;58(3):591-602.
57. Hug G, Thevenet P, Fitoussi J, Baptiste D. Effect of the loading rate on mode I interlaminar fracture toughness of laminated composites. *Engineering Fracture Mechanics*. 2006;73(16):2456-62.
58. Smiley AJ, Pipes RB. Rate sensitivity of mode II interlaminar fracture toughness in graphite/epoxy and graphite/PEEK composite materials. *Composites Science and Technology*. 1987;29(1):1-15.

59. Maikuma H, Gillespie JW, Wilkins DJ. Mode II interlaminar fracture of the center notch flexural specimen under impact loading. *Journal of Composite Materials*. 1990;24(2):124-49.
60. Maikuma H, Gillespie JW, Whitney JM. Analysis and experimental characterization of the center notch flexural test specimen for mode II interlaminar fracture. *Journal of Composite Materials*. 1989;23(8):756-86.
61. Compston P, Jar PYB, Davies P. Matrix effect on the static and dynamic interlaminar fracture toughness of glass-fibre marine composites. *Composites Part B: Engineering*. 1998;29(4):505-16.
62. Blackman BRK, Kinloch AJ, Wang Y, Williams JG. The failure of fibre composites and adhesively bonded fibre composites under high rates of test. *Journal of Materials Science*. 1996;31(17):4451-66.
63. Friedrich K, Walter R, Carlsson LA, Smiley AJ, Gillespie JW. Mechanisms for rate effects on interlaminar fracture toughness of carbon/epoxy and carbon/PEEK composites. *Journal of Materials Science*. 1989;24(9):3387-98.
64. Cantwell WJ. The influence of loading rate on the mode II interlaminar fracture toughness of composite materials. *Journal of Composite Materials*. 1997;31(14):1364-80.
65. Cantwell WJ. Loading rate effects in the mode II fracture of carbon fibre polyetherether-ketone composites. *Journal of Materials Science Letters*. 1996;15(7):639-41.
66. Berger L, Cantwell WJ. Temperature and loading rate effects in the mode II interlaminar fracture behavior of carbon fiber reinforced PEEK. *Polymer Composites*. 2001;22(2):271-81.
67. Compston P, Jar PYB, Burchill PJ, Takahashi K. The effect of matrix toughness and loading rate on the mode-II interlaminar fracture toughness of glass-fibre/vinyl-ester composites. *Composites Science and Technology*. 2001;61(2):321-33.

68. Fracasso RR, M. Pavan, A. Frassine, R. The effects of strain-rate and temperature on the interlaminar fracture toughness of interleaved PEEK/CF composites. *Composites Science and Technology*. 2001;61(1):57-63.
69. Kusaka T, Yamauchi Y, Kurokawa T. Effects of strain rate on mode II interlaminar fracture toughness in carbon-fibre/epoxy laminated composites. *Le Journal de Physique IV*. 1994;4(C8):671-6.
70. Cantwell WJ. The influence of target geometry on the high velocity impact response of CFRP. *Composite Structures*. 1988;10(3):247-65.
71. Takeda N, Sierakowski RL, Malvern LE. Transverse cracks in glass/epoxy cross-ply laminates impacted by projectiles. *Journal of Materials Science*. 1981;16(7):2008-11.
72. Cantwell WJ, Morton J. Geometrical effects in the low velocity impact response of CFRP. *Composite Structures*. 1989;12(1):39-59.
73. Hitchen SA, Kemp RMJ. The effect of stacking sequence on impact damage in a carbon fibre/epoxy composite. *Composites*. 1995;26(3):207-14.
74. Caprino G, Lopresto V, Scarponi C, Briotti G. Influence of material thickness on the response of carbon-fabric/epoxy panels to low velocity impact. *Composites Science and Technology*. 1999;59(15):2279-86.
75. Short D, Summerscales J. Hybrids-a review. Part 1. Techniques, design and construction. *Composites*. 1979;10(4):215-22.
76. Adams DF, Miller AK. An analysis of the impact behavior of hybrid composite materials. *Materials Science and Engineering*. 1975;19(2):245-60.
77. Dorey G, Sidey GR, Hutchings J. Impact properties of carbon fibre/Kevlar 49 fibre hybrid composites. *Composites*. 1978;9(1):25-32.
78. Liu D. Impact-induced delamination—a view of bending stiffness mismatching. *Journal of Composite Materials*. 1988;22(7):674-92.
79. Novak RC, DeCrescente MA. editors. Impact behavior of unidirectional resin matrix composites tested in the fiber direction. 1972;497:311-23.

80. Short D, Summerscales J. Hybrids—a review. Part 2. Physical properties. *Composites*. 1980;11(1):33-8.
81. Lee YS, Kang KH, Park O. Response of hybrid laminated composite plates under low-velocity impact. *Computers and Structures*. 1997;65(6):965-74.
82. Imielińska K, Castaings M, Wojtyra R, Haras J, Clezio EL, Hosten B. Air-coupled ultrasonic C-scan technique in impact response testing of carbon fibre and hybrid: glass, carbon and Kevlar/epoxy composites. *Journal of Materials Processing Technology*. 2004;157:513-22.
83. Naik NK, Ramasimha R, Arya H, Prabhu SV, ShamaRao N. Impact response and damage tolerance characteristics of glass–carbon/epoxy hybrid composite plates. *Composites Part B: Engineering*. 2001;32(7):565-74.
84. Hosur MV, Adbullah M, Jeelani S. Studies on the low-velocity impact response of woven hybrid composites. *Composite Structures*. 2005;67(3):253-62.
85. Hong S, Liu D. On the relationship between impact energy and delamination area. *Experimental Mechanics*. 1989;29(2):115-20.
86. Wu HYT, Springer GS. Measurements of matrix cracking and delamination caused by impact on composite plates. *Journal of Composite Materials*. 1988;22(6):518-32.
87. Strait LH, Karasek ML, Amateau MF. Effects of stacking sequence on the impact resistance of carbon fiber reinforced thermoplastic toughened epoxy laminates. *Journal of Composite Materials*. 1992;26(12):1725-40.
88. Cantwell WJ. The influence of fibre stacking sequence on the high velocity impact response of CFRP. *Journal of Materials Science Letters*. 1988;7(7):756-8.
89. Aktaş M, Atas C, İçten BM, Karakuzu R. An experimental investigation of the impact response of composite laminates. *Composite Structures*. 2009;87(4):307-13.
90. Sela N, Ishai O. Interlaminar fracture toughness and toughening of laminated composite materials: a review. *Composites*. 1989;20(5):423-35.

91. Mukhopadhyay S, Deopura BL, Alagiruswamy R. Interface behavior in polypropylene composites. *Journal of Thermoplastic Composite Materials*. 2003;16(6):479-95.
92. Pinnell MF, Sjoblom PO. Low-Velocity Impact Testing of Thermoplastic and Thermoset Matrix Composite Materials: DTIC Document, 1990.
93. Dorey G, Bishop SM, Curtis PT. On the impact performance of carbon fibre laminates with epoxy and PEEK matrices. *Composites Science and Technology*. 1985;23(3):221-37.
94. Bishop SM. The mechanical performance and impact behaviour of carbon-fibre reinforced PEEK. *Composite Structures*. 1985;3(3-4):295-318.
95. Srinivasan K, Jackson WC, Smith BT, Hinkley JA. Characterization of damage modes in impacted thermoset and thermoplastic composites. *Journal of Reinforced Plastics and Composites*. 1992;11(10):1111-26.
96. Prichard JC, Hogg PJ. The role of impact damage in post-impact compression testing. *Composites*. 1990;21(6):503-11.
97. Nejhad G, Parvizi-Majidi A. Impact behaviour and damage tolerance of woven carbon fibre-reinforced thermoplastic composites. *Composites*. 1990;21(2):155-68.
98. Ramakrishna S, Hamada H, Maekawa Z, Sato H. Energy absorption behavior of carbon-fiber-reinforced thermoplastic composite tubes. *Journal of Thermoplastic Composite Materials*. 1995;8(3):323-44.
99. Chang IY. Thermoplastic matrix continuous filament composites of Kevlar® aramid or graphite fiber. *Composites Science and Technology*. 1985;24(1):61-79.
100. El-Habak AM. Effect of impact perforation load on GFRP composites. *Composites*. 1993;24(4):341-5.
101. Sutherland LS, Guedes Soares C. Effect of laminate thickness and of matrix resin on the impact of low fibre-volume, woven roving E-glass composites. *Composites Science and Technology*. 2004;64(10):1691-700.

102. Yeung P, Broutman LJ. The effect of glass-resin interface strength on the impact strength of fiber reinforced plastics. *Polymer Engineering and Science*. 1978;18(2):62-72.
103. Park SJ, Seo MK, Ma TJ, Lee DR. Effect of chemical treatment of Kevlar fibers on mechanical interfacial properties of composites. *Journal of Colloid and Interface Science*. 2002;252(1):249-55.
104. Kessler A, Bledzki AK. Low velocity impact behavior of glass/epoxy cross-ply laminates with different fiber treatments. *Polymer Composites*. 1999;20(2):269-78.
105. Hirai Y, Hamada H, Kim JK. Impact response of woven glass-fabric composites--I. Effect of fibre surface treatment. *Composites Science and Technology*. 1998;58(1):91-104.
106. Cantwell WJ, Tato W, Kausch HH, Jacquemet R. The influence of a fiber-matrix coupling agent on the properties of a glass fiber/polypropylene GMT. *Journal of Thermoplastic Composite Materials*. 1992;5(4):304-17.
107. Davies GA, Hitchings D, Zhang X. Damage Tolerance to Low Velocity Impact of Laminated Composites: DTIC Document 2000.
108. Liu D, Uchiyama T. Characterization of Energy Absorption Capability of Composite Materials Subjected to Impact Loading. *Proceeding of the American Society for Composites, Technical Conference 2005*;20:107.
109. Jen KC, Sun CT. Matrix cracking and delamination prediction in graphite/epoxy laminates. *Journal of Reinforced Plastics and Composites*. 1992;11(10):1163-75.
110. Davies GAO, Zhang X. Impact damage prediction in carbon composite structures. *International Journal of Impact Engineering*. 1995;16(1):149-70.
111. Sun CT, Jen KC. On the effect of matrix cracks on laminate strength. *Journal of Reinforced Plastics and Composites*. 1987;6(3):208-22.

112. Zhou G, Hill M, Hookham N. Investigation of parameters governing the damage and energy absorption characteristics of honeycomb sandwich panels. *Journal of Sandwich Structures and Materials*. 2007;9(4):309-42.
113. Raju KS, Smith BL, Tomblin JS, Liew KH, Guarddon JC. Impact damage resistance and tolerance of honeycomb core sandwich panels. *Journal of Composite Materials*. 2008;42(4):385-412.
114. Bernard ML, Lagace PA. Impact resistance of composite sandwich plates. *Journal of Reinforced Plastics and Composites*. 1989;8(5):432-45.
115. Tsotsis TK, Lee SM. Characterization of localized failure modes in honeycomb sandwich panels using indentation. *Composite Materials, Testing and Design, ASTM STP 1274*. 1996;12:139-65.
116. Zhou G, Hill M, Loughlan J, Hookham N. Damage characteristics of composite honeycomb sandwich panels in bending under quasi-static loading. *Journal of Sandwich Structures and Materials*. 2006;8(1):55-90.
117. Flores-Johnson EA, Li QM. Experimental study of the indentation of sandwich panels with carbon fibre-reinforced polymer face sheets and polymeric foam core. *Composites Part B: Engineering*. 2011;42(5):1212-9.
118. Sadighi M, Pouriayeali H. Quasi-static and low-velocity impact response of fully backed or simply supported sandwich beams. *Journal of Sandwich Structures and Materials*. 2008;10(6):499-524.
119. Mines RAW, Worrall CM, Gibson AG. Low velocity perforation behaviour of polymer composite sandwich panels. *International Journal of Impact Engineering*. 1998;21(10):855-79.
120. Mohan K, Yip TH, Sridhar I, Seow H. Effect of face sheet material on the indentation response of metallic foams. *Journal of Materials Science*. 2007;42(11):3714-23.



121. Park JH, Ha SK, Kang KW, Kim CW, Kim HS. Impact damage resistance of sandwich structure subjected to low velocity impact. *Journal of Materials Processing Technology*. 2008;201(1–3):425-30.
122. Shuaieb FM, Soden PD. Indentation failure of composite sandwich beams. *Composites Science and Technology*. 1997;57(9–10):1249-59.
123. Herup EJ, Palazotto AN. Low-velocity impact damage initiation in graphite/epoxy/Nomex honeycomb-sandwich plates. *Composites Science and Technology*. 1998;57(12):1581-98.
124. Anderson T, Madenci E. Experimental investigation of low-velocity impact characteristics of sandwich composites. *Composite Structures*. 2000;50(3):239-47.
125. Shih WK, Jang BZ. Instrumented impact testing of composite sandwich panels. *Journal of Reinforced Plastics and Composites*. 1989;8(3):270-98.
126. Kim CG, Jun EJ. Impact resistance of composite laminated sandwich plates. *Journal of Composite Materials*. 1992;26(15):2247-61.
127. Akay M, Hanna R. A comparison of honeycomb-core and foam-core carbon-fibre/epoxy sandwich panels. *Composites*. 1990;21(4):325-31.
128. Nettles A, Hodge A, editors. Impact testing of glass/phenolic honeycomb panels with graphite/epoxy facesheets. 35th International SAMPE Symposium, Anaheim, CA; 1990.
129. Compston P, Styles M, Kalyanasundaram S. Low energy impact damage modes in aluminum foam and polymer foam sandwich structures. *Journal of Sandwich Structures and Materials*. 2006;8(5):365-79.
130. Caprino G, Teti R. Impact and post-impact behavior of foam core sandwich structures. *Composite Structures*. 1994;29(1):47-55.
131. Lim TS, Lee CS, Lee DG. Failure modes of foam core sandwich beams under static and impact loads. *Journal of Composite Materials*. 2004;38(18):1639-62.

132. Lin C, Fatt MSH. Perforation of sandwich panels with honeycomb cores by hemispherical nose projectiles. *Journal of Sandwich Structures and Materials*. 2005;7(2):133-72.
133. Johnson W. *Impact strength of materials*: London : Edward Arnold; 1983.
134. Backman ME, Goldsmith W. The mechanics of penetration of projectiles into targets. *International Journal of Engineering Science*. 1978;16(1):1-99.
135. Corbett GG, Reid SR, Johnson W. Impact loading of plates and shells by free-flying projectiles: a review. *International Journal of Impact Engineering*. 1996;18(2):141-230.
136. Virostek SP, Dual J, Goldsmith W. Direct force measurement in normal and oblique impact of plates by projectiles. *International Journal of Impact Engineering*. 1987;6(4):247-69.
137. Lee SWR, Sun CT. Dynamic penetration of graphite/epoxy laminates impacted by a blunt-ended projectile. *Composites Science and Technology*. 1993;49(4):369-80.
138. Ursenbach DO, Vaziri R, Delfosse D. An engineering model for deformation of CFRP plates during penetration. *Composite Structures*. 1995;32(1):197-202.
139. Zhu G, Goldsmith W, Dharan CKH. Penetration of laminated Kevlar by projectiles. I. Experimental investigation. *International Journal of Solids and Structures*. 1992;29(4):399-420.
140. Goldsmith W, Dharan CKH, Chang H. Quasi-static and ballistic perforation of carbon fiber laminates. *International Journal of Solids and Structures*. 1995;32(1):89-103.
141. Dorey G. *Impact and crashworthiness of composite structures*. Elsevier Science Publishing Co, Inc. 1984:155-92.
142. Cantwell WJ, Morton J. Impact perforation of carbon fibre reinforced plastic. *Composites Science and Technology*. 1990;38(2):119-41.

143. Wen HM, Reddy TY, Reid SR, Soden PD. Indentation, penetration and perforation of composite laminate and sandwich panels under quasi-static and projectile loading. *Key Engineering Materials*. 1997;141:501-52.
144. Reddy TY, Wen HM, Reid SR, Soden PD. Penetration and perforation of composite sandwich panels by hemispherical and conical projectiles. *Journal of Pressure Vessel Technology*. 1998;120:186.
145. Reid SR, Wen HM, Soden PD, Reddy TY. Response of single skin laminates and sandwich panels to projectile impact. *Composite Materials for Offshore Operation*. 1999;2:593-617.
146. Hoo Fatt MS, Park KS. Dynamic models for low-velocity impact damage of composite sandwich panels—Part A: Deformation. *Composite Structures*. 2001;52(3):335-51.

## **CHAPTER III**

### **EXPERIMENTAL PROCEDURE**

---

The materials used in this study, the manufacturing processes and the testing procedures are presented in the following chapter. Initially, the mechanical properties of the core material and the skins are reported. Details of specimen preparation are then outlined. Following this, mechanical testing procedures including compression, Mode I, Mode II (shear), indentation and low velocity impact tests are presented.

### 3.1 The Core Materials

#### 3.1.1 Polypropylene (PP) Honeycomb

The PP honeycomb investigated in this study was supplied in sheet form with a thickness of 15 mm by EconCore NV. Two densities of PP honeycomb were used, these being 40 and 80 kg/m<sup>3</sup>. The typical compression strength and modulus for the 80 kg/m<sup>3</sup> PP honeycomb are 1.2 and 40 MPa respectively. The wall-to-wall distance for both honeycombs was approximately 9.6 mm. This hexagonal honeycomb core was finished with a combination of polypropylene and polyester films (1).

#### 3.1.2 Corrugated Paperboard

The second type of core material investigated in this study was a corrugated paperboard. It was supplied by Xanita Ltd, South Africa. The corrugated panel was brown in colour and was manufactured from recycled paper-waste (**Table 3.1**). This fully recycled core has a high strength to weight ratio, good sound absorption characteristics and a high flexural strength. This material is commonly used in the furniture and packaging industries (2).

Compression strength [MPa]	0.88
Density [kg/m <sup>3</sup> ]	88
Thickness [mm]	16

**Table 3.1** Summary of the mechanical properties of the corrugated cardboard.

### 3.1.3 Polymer Foam

#### 3.1.3.1 Crosslinked (H 130) and Linear (HD 130) PVC Foams

The crosslinked and linear PVC foams were supplied by Divinycell Ltd. The linear polyvinyl-chloride (PVC) (HD 130) and the crosslinked PVC (H 130) systems are closed-cell foams (3). These foams exhibit a high strength to density ratio, impressive compressive strength characteristics and also offer excellent shear properties. The mechanical properties of both foams are given in the **Table 3.2**.

	HD 130	H 130
Compression strength [MPa]	2.1	3.0
Compression modulus [MPa]	140	170
Density [kg/m <sup>3</sup> ]	130	130
Shear strength [MPa]	0.8	2.2
Shear modulus [MPa]	32	50
Thickness [mm]	25	25

**Table 3.2** *Summary of the properties of the linear PVC (HD 130) and crosslinked PVC (H 130) foams investigated in this study.*

#### 3.1.3.2 Linear-styreneacrylonitrile (SAN) Foam

The SAN A500 foam used in this study was supplied by Gurit AG. The applications of this closed-cell foam are in the manufacture of boat hull, wind turbine blades and sporting goods (4). **Table 3.3** summaries the mechanical properties of this foam.

Compression strength [MPa]	0.9
Compression modulus [MPa]	64
Density [kg/m <sup>3</sup> ]	92
Shear strength [MPa]	1.0
Shear modulus [MPa]	26
Thickness [mm]	25

**Table 3.3** *Summary of the mechanical properties of the A500 foam.*

#### **3.1.3.3 Polymethacrylimide (PMI) Foam**

The PMI (WF 71) foam investigated here was supplied by Evonik Industries Ltd. This foam can withstand pressures and temperatures up to 0.7 MPa and 130°C respectively (5). These materials are widely used in the aerospace and automotive industries. Other applications include in the manufacture of skis, rackets, and yachts. The mechanical properties of this foam are shown in **Table 3.4**.

Compression strength [MPa]	1.7
Tensile Strength [MPa]	2.2
Density [ $\text{kg/m}^3$ ]	75
Shear strength [MPa]	1.3
Shear modulus [MPa]	42
Thickness [mm]	25

**Table 3.4** Summary of mechanical properties of the polymethacrylimide (WF 71) foam.

#### 3.1.3.4 Crosslinked PVC (C70) Foams

The crosslinked PVC (C70) foam was supplied by Alcan Ltd. This thermoplastic core material offers a high impact strength, chemical resistance, although a high stiffness and strength to weight ratio. Two thicknesses of crosslinked PVC foam were used in this study, these being 20 and 25 mm. The material properties for the five densities of crosslinked PVC foam are given in **Table 3.5**.

#### 3.1.3.5 Linear PVC (R63) Foams

Here, two types of linear PVC foam were used as shown in **Table 3.5**. These rigid foams offer an excellent impact strength and a ductile failure mode. Typical applications of this material are in manufacture of ship hulls and ferries, helmets, cargo containers and surfboards (6).



	C70.55	C70.75	C70.90	C70.130	C70.200	R63.80	R63.140
Density [kg/m <sup>3</sup> ]	60	80	100	130	200	80	140
Compression strength [MPa]	0.90	1.45	2.0	3.0	5.2	0.9	1.6
Compression modulus [MPa]	65	104	130	170	280	56	110
Shear strength [MPa]	0.9	1.2	1.7	2.4	3.5	1.0	1.9
Shear modulus [MPa]	22	30	40	54	75	21	37
Thermal conductivity [W/m.K]	0.031	0.033	0.035	0.039	0.048	0.037	0.039

**Table 3.5** Material properties of the crosslinked PVC (C70) and linear PVC (R63) foams.

### 3.1.3.6 Polyethyleneterephthalate (T92) Foams

The final type of polymer core investigated in this study was based on a polyethyleneterephthalate (PET) foam. This thermoplastic foam is compatible with all common resins and is fully recyclable. Its outstanding performance in compression and shear makes it suitable for use in dynamically-loaded structural applications, such as kayaks, trains and boats (6). The foam was supplied by Alcan Composites Ltd and its properties of PET foams are summarised in **Table 3.6**.

	T92.100	T92.130
Density [kg/m <sup>3</sup> ]	100	130
Compression strength [MPa]	1.4	1.8
Compression modulus [MPa]	90	110
Shear strength [MPa]	0.9	1.05
Shear modulus [MPa]	21	23
Thermal conductivity [W/m.K]	0.034	0.035

**Table 3.6** *Properties of the PET foams investigated in this study.*

## 3.2 The Skin Materials

Five different types of composite material were used as skins. **Table 3.7** gives a summary of the mechanical properties of the composites investigated in this study. Further details of this composite are given below.

### **3.3.2 Glass Fibre Reinforced Epoxy (GFRP)**

The unidirectional glass fibre reinforced epoxy (GFRP) (UD001) used in this study was manufactured by the Advanced Composites Group, UK. This unidirectional GFRP was supplied in a form of a 0.5 meter wide prepreg roll with density  $1120 \text{ kg/m}^3$ . The thickness of the prepreg is 0.25 mm with a fibre weight fraction of 62% (7).

### **3.3.3 Self-reinforced Polypropylene (SRPP) (Curv)**

The self-reinforced polypropylene (SRPP) (Curv) was supplied by Propex Fabrics (Germany). It is 100% polypropylene and fully recyclable. SRPP is commonly used in car body panels, luggage and sporting goods (8). The advantages of using SRPP include low weight, high impact resistance, non-toxicity and high resistance to abrasion. It was supplied in the form of a black sheet in a range of thicknesses from 0.3 to 3 mm.

### **3.3.4 Woven Glass Fibre-Reinforced Polymer (GFRP)**

The woven glass fibre reinforced polymer (GFRP) (Stesapreg EP127-44-40), manufactured by Gurit Ltd. The fibre volume fraction is approximately 55 % and the thickness of the prepreg is 0.15 mm. It is suitable for the production of high-performance composite structures and is widely used in the aviation industries, automotive and marine industries (9).

### **3.2.4 Woven Glass Fibre-reinforced Polyamide 6,6 (GFPA)**

The woven glass fibre reinforced polyamide 6,6 (GFPA) was supplied by Bond Laminates GmbH, in the form of composite sheets with a thickness of 0.5 mm. It is black in colour. High

toughness, high stiffness, excellent impact performance and chemical resistance are the key properties associated with this material. Typical applications are in the automotive industry, structural parts, aerospace industries and helmet shells (10).

Material	Grade	Ultimate Tensile Strength (MPa)	Tensile Modulus (GPa)	Density (kg/m <sup>3</sup> )
Unidirectional GFRP	UD001/00 (unidirectional glass fibre/ epoxy resin matrix)	1100	45	1120
SRPP	Woven polypropylene fibre/ polypropylene matrix	120	4.2	920
Woven GFRP	Stesapreg EP 127-44-40 (woven E-glass fibre/triazine resin matrix)	460	23	1175
Woven GFPA	TEPEX Dynalite 101-RGUD600 (woven E-glass fibre/ polyamide 6,6 matrix)	605	30.1	1800

**Table 3.7** *Summary of the mechanical properties of the composite skins*

### 3.3 Manufacture of the Sandwich Structures

#### 3.3.1 Manufacture of Honeycomb and Corrugated Paperboard Sandwich Structures

The polypropylene the honeycomb and the corrugated paperboard sandwich panels were manufactured by placing the SRPP skins, the adhesive and the core materials in a steel

picture frame mould. A 60 micron polypropylene film was used as an adhesive to bond the skins to the composite core. For the multilayer SRPP skins, a ply of polypropylene film was used between each SRPP layer and between the SRPP laminates and the composite core. This thermoplastic film was supplied by Collano (Switzerland).

The mould was then placed in an air-circulating oven and heated to temperatures between 175 and 185°C before being removed for cooling to room temperature. The panel was then removed from the mould and inspected for defects.

### 3.3.2 Manufacture of Polymer-foam Based Sandwich Structures

A Meyer hot press (**Figure 3.1**) was used to prepare the skins. This conventional compression moulding machine uses pneumatic pressure to mould the sample. Initially, the composite plies were cut to a size of 150 x 150 mm before placing into picture frame mould as shown in **Figure 3.2**. The configurations and thicknesses of the laminates used in this study are tabulated in **Table 3.8**. A thermocouple was placed between the composite layers in order to monitor the processing temperature.

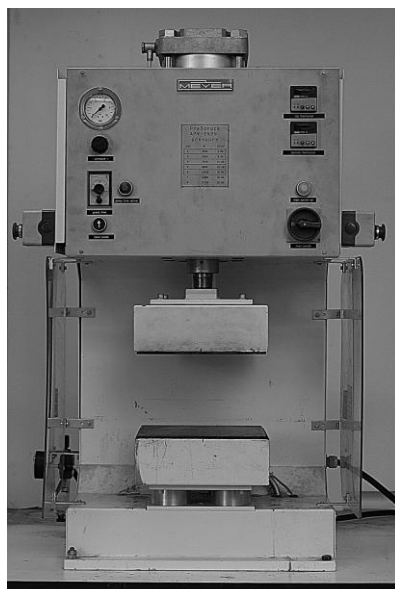


**Figure 3.1** *The Meyer hot press used for manufacturing the composite skins*

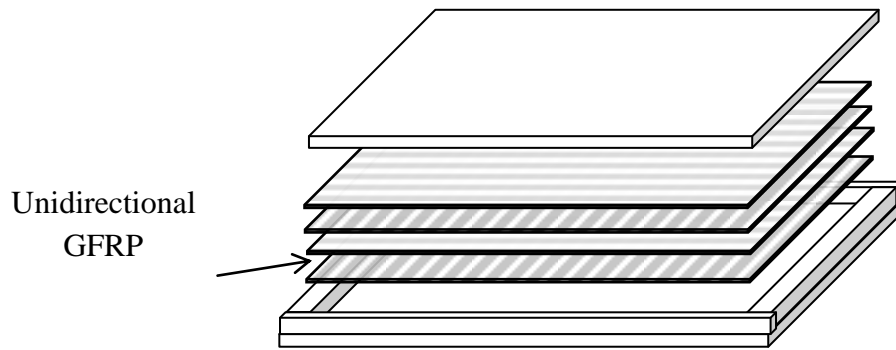


**Figure 3.2** Schematic of the stacking sequence for a 4-ply of unidirectional GFRP composite.

The stacked plies were then heated to 125 °C for one hour under a pressure of 3 bar, before cooling slowly to room temperature. Once the mould had cooled, the pressure was released and the mould was removed from the press. The composite skin was then removed from the mould and inspected visually.

The unidirectional GFRP, woven GFRP and GFPA skins were bonded to the cores using a two part epoxy paste and cured under pressure for twelve hours at room temperature.

Material	Configuration	Number of plies	Nominal thickness (mm)
Unidirectional GFRP	0/90	2	0.5
	0/90/90/0	4	1.0
	0/90/0/90/90/0/90/0	8	2.0
	0/90/0/90/0/90/90/0/90/0/90/0	12	3.0
	0/90/0/90/0/90/0/90/90/0/90/0/90/0/90/0	16	4.0
Woven GFRP	Woven	2	0.25

**Table 3.8** *Summary of the configurations and thicknesses of the unidirectional and woven GFRP skins.*

### 3.4 Determination of the Mechanical Properties of the Composites

The mechanical properties of the composites were studied through a series of quasi-static and dynamic compression, quasi-static and dynamic single-end notch bend (SENB) and Mode II (shear) tests. The following section details the experimental arrangements for the tests conducted here.

#### 3.4.1 Compression Tests

##### 3.4.1.1 Quasi-static Compression Testing

Quasi-static compression tests were conducted using a 5 kN load cell on an Instron 4045 universal testing machine. The compressive tests were conducted according to BS ISO 844:1998 (11) on specimens with dimensions of 20 x 20 mm. In this study, at least three

specimens of each type of material were examined. Initially, the specimens were placed between two circular plattens and loaded at a crosshead displacement rate of 1 mm/minute. The output of the compression test results was then recorded in the form of load versus displacement traces. The compression tests were continued beyond the densification threshold of the specimen. The specimen was then unloaded and removed from the plattens.

The compressive stress-strain curves were plotted in order to determine the mechanical properties of the materials. The compressive strength was calculated using:

$$\sigma_c = \frac{P}{A_o} \quad [3.1]$$

where  $\sigma_c$  = compressive strength (MPa),  $P$  = load and  $A_o$  = original cross-sectional area of the specimen ( $\text{m}^2$ )

The strain was calculated using:

$$\varepsilon_c = \frac{\delta L}{L} \quad [3.2]$$

where  $\varepsilon_c$  = compression strain,  $\delta L$  = elongation (m) and  $L$  = original length (m)

### 3.4.1.2 Dynamic Compression Testing

The dynamic compressive properties of the materials were evaluated using a drop-weight impact tower. Here, a steel carriage with a 50 mm diameter circular disk was guided by two steel columns. A 10 kN Kistler 9321A piezo-electric load cell was used to record the voltage-time traces during the tests. Initially, a static calibration was undertaken using the Instron 4045 machine in order to obtain the voltage-force conversion factor. This load cell was then located just above the circular disk. The movement of the sample deformation during the impact event was recorded using a high speed camera positioned in front of the



impact tower. Prior to testing, specimens with dimensions of 20 x 20 x 20 mm were cut from the panel using a band saw and then placed on the top of a rigid support as shown in **Figure 3.3**.

The dynamic compression tests were continued until the specimens had been completely crushed. In this study, a 5 mm thick rubber sheet was placed on top of the specimen in order to minimise ringing due to impact (12).

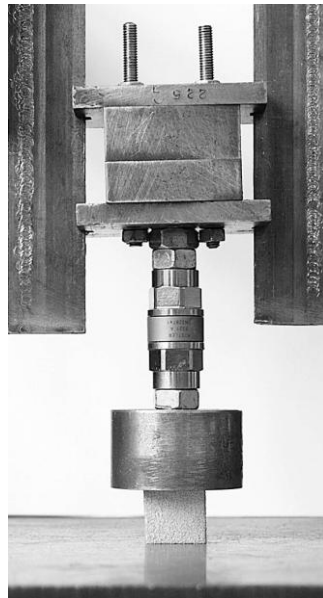


**Figure 3.3** *Photo of the dynamic compression test geometry.*

### 3.4.2 Single End Notch Bend Test (SENB)

#### 3.4.2.1 Quasi-static SENB Tests

Quasi-static SENB tests were conducted using an Instron 4045 and loaded under three point bending conditions. The specimen was loaded at a crosshead displacement rate of 10 mm/minute until it had completely fractured. Initially, the specimens were cut into beams

with dimensions of 150, 30 and 20 mm using a bend saw. A notch with a length of approximately 10 mm was introduced in the middle of the sample. This notch was sharpened by tapping a sharp razor blade as suggested in the BS ISO 13586:2000 standard (13). The loading regime for the quasi-static SENB test is shown in **Figure 3.4**.

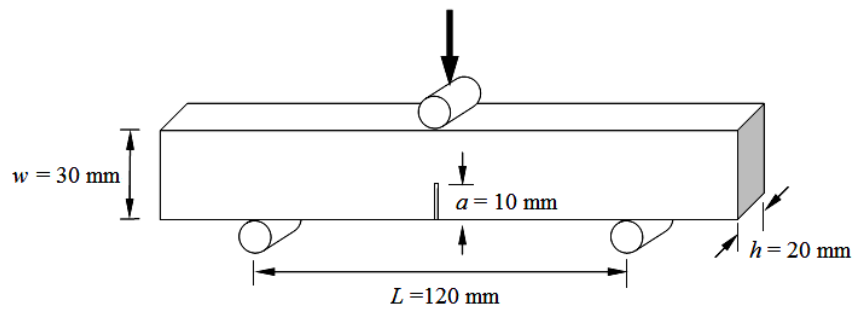


**Figure 3.4** Schematic diagram of the quasi-static SENB test geometry.

The toughnesses of the materials were characterised by determining the work of fracture ( $W_f$ ) using:

$$W_f = \frac{U}{h(w-a)} \quad [3.3]$$

where,  $U$  = energy absorbed by the specimen,  $h$  = thickness,  $w$  = depth and  $a$  = notch length.

### 3.4.2.2 Dynamic Single End Notch Bending Tests

Dynamic SENB tests were conducted by placing the test samples on the same supports as those used for quasi-static testing and impacting the sample using the drop-weight impact rig. A 10 mm diameter loading bar was located on the nose of the carriage in order to apply a line load to the sample. The load-time and displacement-time traces were recorded using a piezo-

electric load cell and a high-speed camera respectively. The tests were conducted using a kilogram impact mass at 1 m/s, as suggested in BS ISO17281:2002 (14). A schematic of the dynamic SENB test fixture is shown in **Figure 3.5**.

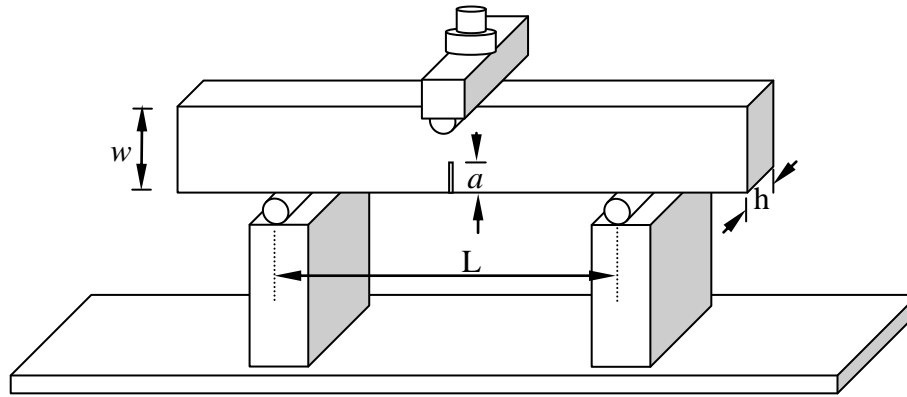
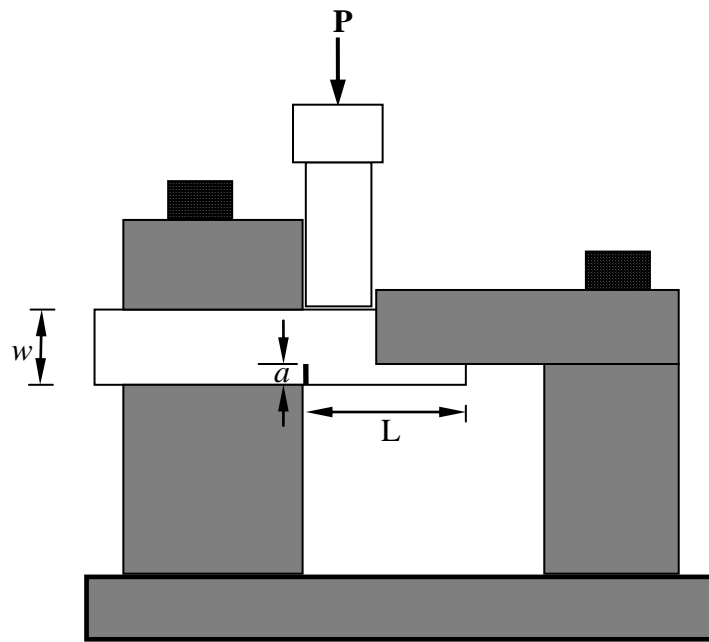


**Figure 3.5** Schematic diagram of the dynamic SENB test geometry.

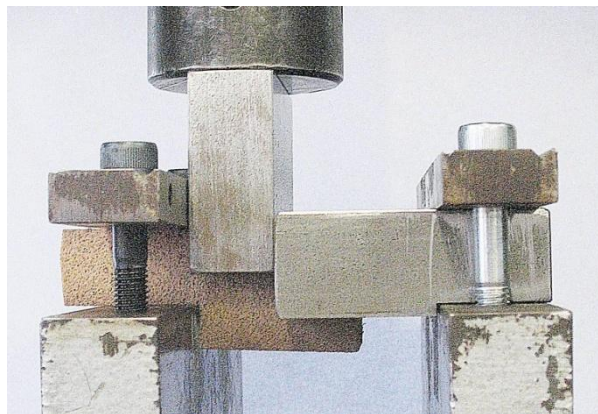
### 3.4.3 Mode II (Shear) Test

Mode II (shear) tests were carried out on nine polymer foams using a purpose-built rig, as shown in **Figure 3.6**. The fracture properties of the foams were investigated on specimens with nominal notch length ( $a$ ), length ( $L$ ), depth ( $w$ ) and thickness ( $d$ ) dimensions of 10, 80, 30 and 20 mm respectively.

The specimens were clamped at one end and loaded at 10 mm/min in a shearing mode by a solid steel transverse. The shearing action of the crosshead caused the foam to fail along a vertical plane. As before, the work of fracture was calculated from the area under the load-displacement trace and the area of the fractured ligament. The shear strength of the foam was determined from the maximum measured load and the area of the fractured ligament.



(a)



(b)

**Figure 3.6** (a) Schematic diagram and (b) photo of the Mode II test geometry

### 3.4.4 Indentation Test

#### 3.4.4.1 Quasi-static Indentation Tests

A series of quasi-static indentation tests was carried out on the polymer foam sandwich structures using an Instron 4045 universal testing machine. The tests were conducted at a

crosshead displacement rate of 1 mm/min using a hemispherical steel indenter with diameters 5, 10, 15 and 20 mm. **Figure 3.7** shows the hemispherical indentors used in this study.



**Figure 3.7** Photo of the hemispherical indentors used during the indentation test.

The load-displacement traces were recorded during the test. The deformation of the uppermost skin of the sandwich structure was determined using an extensometer attached to both the indenter and the top surface of the sandwich structures as shown in **Figure 3.8**.

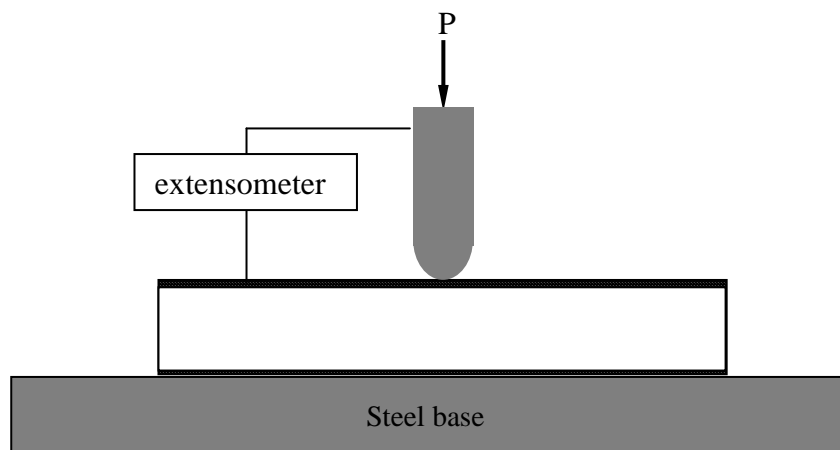


**Figure 3.8** Schematic diagram of the indentation test.

The indentation response of the sandwich structures was characterised using a Meyer indentation law of the form:

$$P = C\alpha^n \quad [3.4]$$

where  $P$  is the applied load,  $\alpha$  is the contact indentation,  $C$  is the contact stiffness and  $n$ , the constact parameter. The contact parameters,  $C$  and  $n$  were derived from the intercept and the gradient of the plot of  $\log P$  versus  $\log \alpha$  curves.

$$\log P = \log C + n \log \alpha \quad [3.5]$$

The parameters  $C$  and  $n$  can be calculated using a curve-fitting method as shown in **Figure 3.9**.

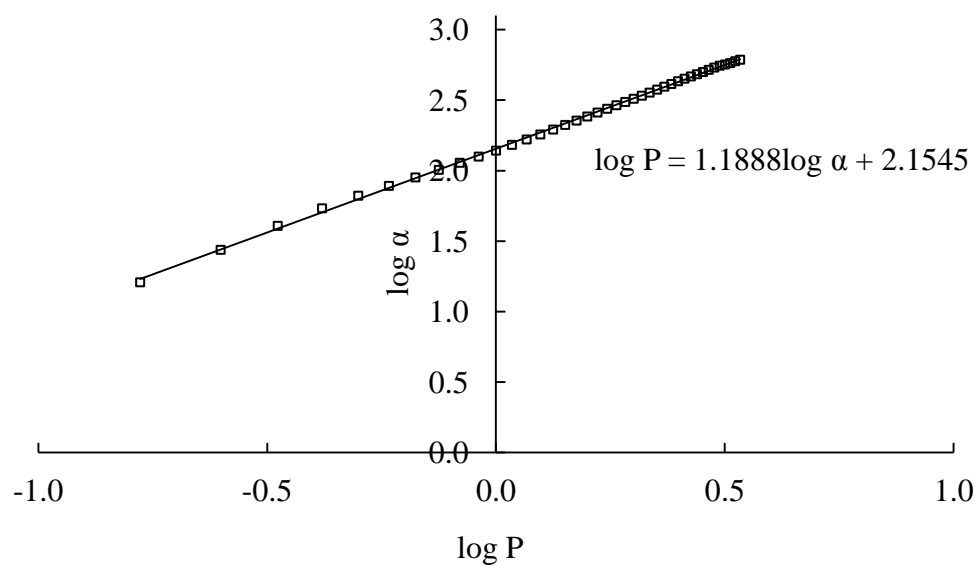


**Figure 3.9** Typical plot of  $\log P$  versus  $\log \alpha$  for the quasi-static indentation tests for linear PVC R63.80.

#### 3.4.4.2 Dynamic Indentation Tests

Low velocity impact tests were undertaken to investigate the strain-rate sensitivity of the sandwich structures, **Figure 3.10**. The sandwich structure was placed on the top of a solid steel base and the top surface was loaded by an indenter. The four previously-discussed indenter diameters were employed during impact testing. The impact force was recorded

using a load cell situated just above the indenter. The signal from the load cell was amplified by a strain gauge amplifier and recorded using a dedicated desktop computer.

The displacement of the top surface of the sandwich structure was measured using a high speed video camera positioned in front of the impact tower. After testing, the data from the load cell and the high speed camera were combined, giving a load-indentation trace for the impact event. The indentation law given in equation [3.4] was then used to characterise the indentation behaviour of the sandwich structures.

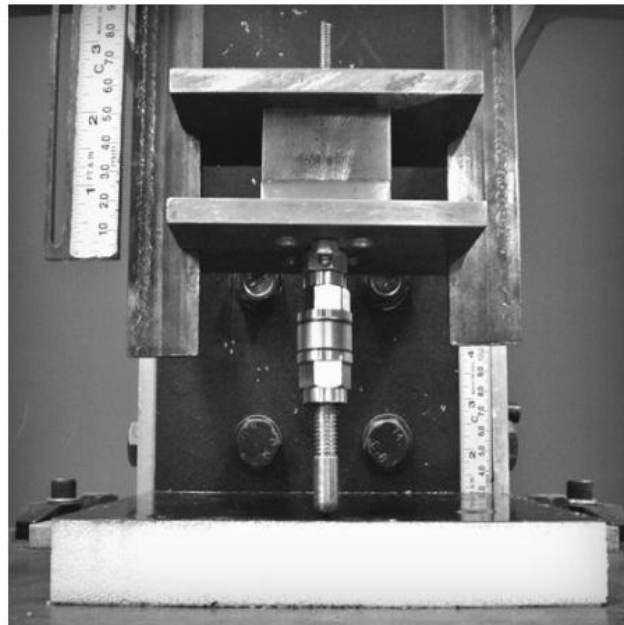


**Figure 3.10** *Photo of the dynamic indentation test.*

### 3.4.5 Low Velocity Impact Testing

The perforation resistance of the sandwich structures was investigated using an instrumented drop-weight impact tower. Here, a 5.6 kg carriage was released from heights up to 1.4 m onto

sandwich structures supported on a 100 mm diameter circular steel ring as shown in **Figure 3.11**. The panels, with dimensions of 150 x 150 mm and 20 mm thick, were impacted centrally. Prior to testing, eight of 10 mm diameter holes were drilled along the edges of the panels.

A Kistler 9312B load-cell was used to record the voltage signal. It was located just above the 12 mm diameter hemispherical indenter. A charge amplifier, Kistler 5011B, was used to convert the output into a proportional voltage signal. The voltage signal was analysed and recorded using a TRA 800 Instrument oscilloscope.



**Figure 3.11** *The low velocity impact tower.*



A high-speed video camera was used to measure the displacement of the impactor. The camera, with a standard F/0.95-50 mm lens, was placed approximately one metre in front of the impact tower to record the deformation of the specimen. Two high-intensity lamps were used to illuminate the test rig during filming as shown in **Figure 3.12**.

The recording was started at the moment the indenter impacted the uppermost surface of the sandwich panel and continued until the indenter had stopped. The distance, in pixels, was converted into millimetres versus time curves using the ProAnalyst<sup>®</sup> software package.

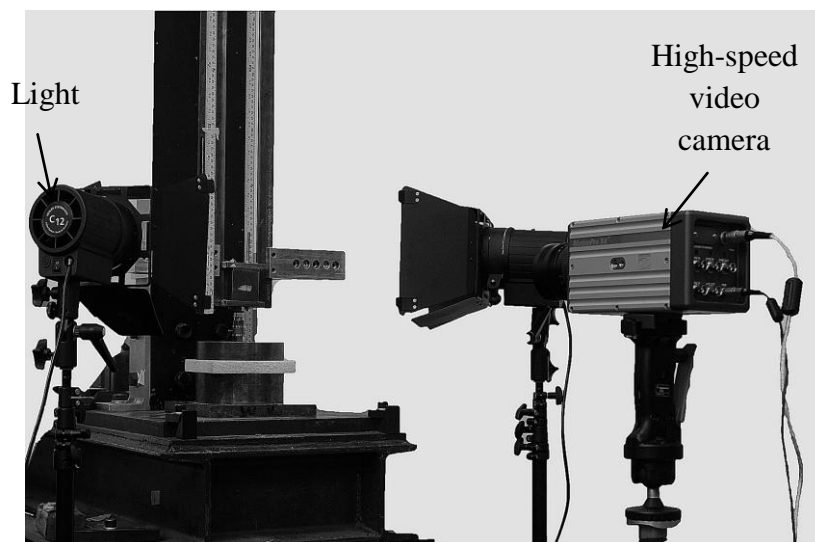


**Figure 3.12** *The high speed video camera set-up used for drop-weight impact testing.*

In order to calculate the energy absorbed by the sandwich panels, load-displacement traces were plotted and the area under load-displacement curves was then determined using the trapezoidal rule (15).

### 3.5 References

- (1) [www.econcore.com](http://www.econcore.com)
- (2) [www.xanita.com](http://www.xanita.com)
- (3) <http://www.diabgroup.com/>
- (4) <http://www.gurit.com/corecell-mfoam.aspx>
- (5) <http://www.rohacell.com>
- (6) <http://www.airexag.ch>
- (7) <http://www.advanced-composites.co.uk/>
- (8) [www.curvonline.com/](http://www.curvonline.com/)
- (9) <http://www.gurit.com/>
- (10) [www.bond-laminates.com/](http://www.bond-laminates.com/)
- (11) BS ISO 844; 1998, Cellular plastic – compression test for rigid materials – specification
- (12) Hsiao HM, Daniel IM. Strain rate behaviour of composite materials, Composites Part B: Engineering, 1998;29(5):521-33
- (13) BS ISO 13586:2000, Plastics - Determination of fracture toughness ( $G_{IC}$  and  $K_{IC}$ ) – linear elastic fracture mechanics (LEFM) approach
- (14) BS ISO 13586:2000, Plastics - Determination of fracture toughness ( $G_{IC}$  and  $K_{IC}$ ) at moderately high loading rates (1 m/s)
- (15) El-Gebeily, Yushau B. Mathematics Numerical Methods with MS Excel, The Montana Mathematics Enthusiast, 2007;4(1):84-92

## **CHAPTER IV**

### **MECHANICAL BEHAVIOUR OF THE CORE**

---

This part of the research study focused on examining the mechanical properties and fracture characteristics of the core materials. Initially, compression tests on the plain core composite materials were conducted to determine the basic mechanical properties of the foams, including the elastic modulus ( $E_c$ ), the plastic collapse stress ( $\sigma_{pl}$ ) and the steady-state stress ( $\sigma_{ss}$ ) of the core materials. Following this, results from single-end-notch bend (Mode I) and shear tests (Mode II) on the polymer foam are presented.

## 4.1 Compression Tests

Quasi-static and dynamic compression tests have been undertaken in order to investigate the mechanical response and strain-rate effects in a range of foams when subjected to compressive loading. An Instron 4045 machine was used for quasi-static testing and a drop-weight impact tower was used for dynamic loading. The value of the modulus of elasticity,  $E_c$ , the plastic collapse stress,  $\sigma_{pl}$ , the steady-state stress  $\sigma_{ss}$  and the densification strain,  $\varepsilon_D$ , were determined from the resulting stress-strain curves.

### 4.1.1 The Quasi-static Compressive Behaviour of the Cores

#### 4.1.1.1 Compression Behaviour of the Crosslinked PVC (C70), Linear PVC (R63) and PET (T92) Foams

Quasi-static compression tests have been conducted on 13 different core materials at a crosshead displacement rate of 1 mm/min. **Figure 4.1** shows a typical load-displacement trace for the crosslinked PVC (C70.90) foam. This compression curve has three distinct phases. For compression strains less than 5 %, the foam obeyed Hooke's law, where the engineering strain,  $\varepsilon$ , is directly proportional to the applied stress,  $\sigma$ . The modulus of elasticity,  $E_c$ , was determined directly from the slope of this curve (the average in this case was 39.5 MPa). When the compression strain reached 6 %, the stress-strain plot exhibited a peak at a plastic collapse stress,  $\sigma_{pl}$ , of approximately 1.6 MPa. The mechanical properties of this group of foams are listed in **Table 4.1**. The quasi-static stress-strain plot in **Figure 4.1** is similar to that of a typical curve in which the initial elastic region is influenced by the elastic cell-wall bending (1). The second phase, occurring between strains of 8 % and 43 %, is characterised by a relatively constant plateau stress,  $\sigma_{ss}$  (an average value of approximately 1.53 MPa is apparent). This region provides the majority of the energy absorption capacity of the foam. The stress remains constant with increasing strain and is associated with the

collapse of the cells. The final deformation phase involves densification of the foam, where the majority of cell walls collapse and opposing cell walls touch each other.

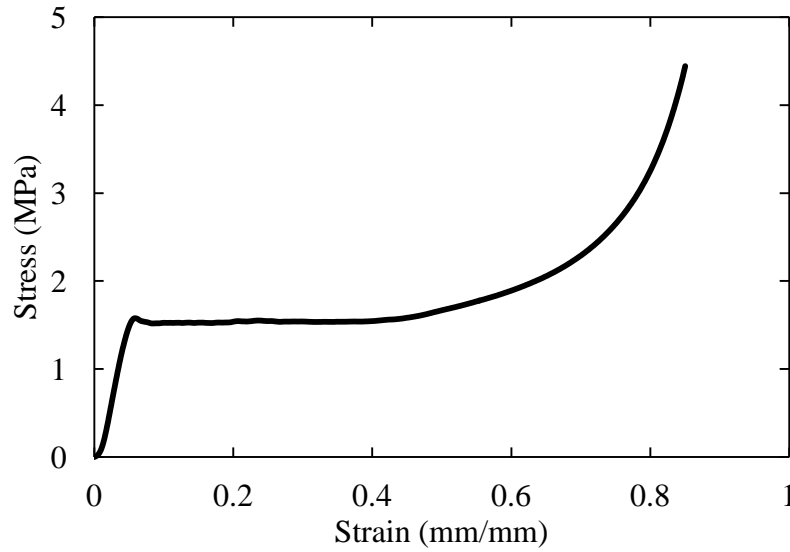


**Figure 4.1** A typical stress-strain trace following quasi-static testing on a crosslinked PVC C70.90 foam.

The foam then begins to respond as a compacted solid at a densification strain,  $\varepsilon_D$ , of 65 %, at which point the compressive stress increased rapidly. The value of  $\varepsilon_D$  was defined as the strain at which the energy absorption efficiency reaches a maximum in the efficiency-strain curve as shown in **Figure 4.2**. The energy absorption efficiency is defined by (2):

$$\eta_\varepsilon = \frac{1}{\sigma(\varepsilon)} \int_0^\varepsilon \sigma(\varepsilon) d\varepsilon \quad [4.1]$$

Where  $\int_0^\varepsilon \sigma(\varepsilon) d\varepsilon$  is the energy absorbed by the foam.

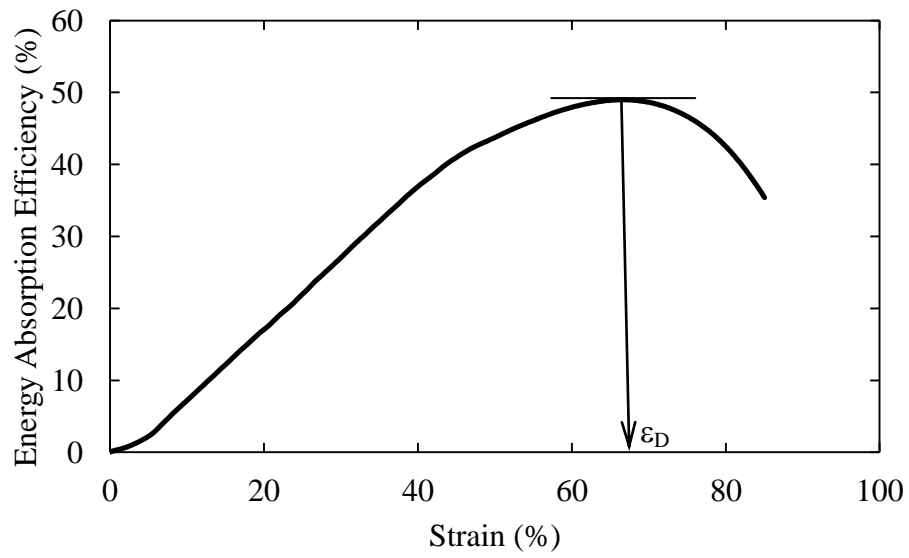


**Figure 4.2** Energy absorption efficiency-strain plot following quasi-static tests on a crosslinked PVC C70.90 foam.

Foam	Density (kg/m <sup>3</sup> )	Plastic collapse stress, $\sigma_{pl}$ (MPa)	Compressive modulus, $E_c$ (MPa)	Steady state stress, $\sigma_{ss}$ (MPa)	Densification strain, $\varepsilon_D$ (%)
C70.55	60	0.70	18.86	0.74	66.24
C70.75	80	1.29	29.75	1.43	66.02
C70.90	100	1.57	39.45	1.53	65.43
C70.130	130	2.34	53.42	2.44	63.66
C70.200	200	4.19	100.9	4.13	62.01
R63.80	90	0.98	28.92	0.76	60.33
R63.140	140	1.56	44.22	1.33	58.12
T92.100	105	1.04	29.63	1.13	60.53
T92.130	135	1.87	42.43	1.94	59.84

**Table 4.1** Average mechanical properties of the crosslinked (C70), linear (R63) and PET (T92) foams.

The effect of varying the density of the crosslinked-PVC foam on the mechanical response of the foams is shown in **Figure 4.3**. The figure shows that an increase in density results in an increase in the modulus of elasticity, the plastic collapse stress, the steady-state stress and a decrease in the densification strain. **Figure 4.4** shows that an increase in density from 60 to 200 kg/m<sup>3</sup> results in an increase in the number of cell walls, which in turn become smaller and thicker. Brenzy and Green (3) reported that the mechanical behaviour of a foam, including its elastic modulus and compressive strength, are directly related to the cell size. They found that the plastic collapse strength and Young's modulus increased steadily with decreasing cell size. From **Figure 4.3**, it is clear that an increase in density serves to increase the steady-state stress before the foam begins to densify. The nominal densification strain was 66 % for the 60 kg/m<sup>3</sup>, 66 % for the 80 kg/m<sup>3</sup>, 65 % for the 100 kg/m<sup>3</sup>, 64 % for the 130 kg/m<sup>3</sup> and approximately 62 % for 200 kg/m<sup>3</sup> for the crosslinked-PVC foam.

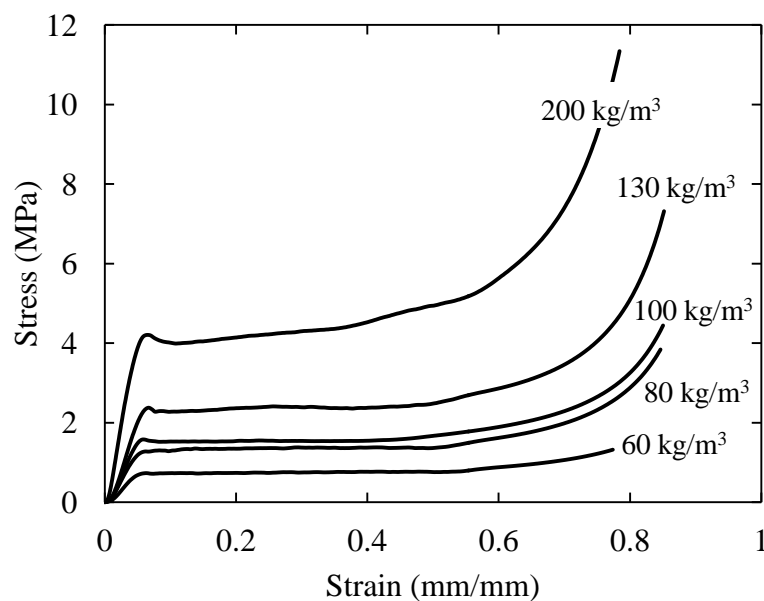


**Figure 4.3** Typical stress-strain traces following quasi-static tests on the crosslinked PVC foams (C70.55), (C70.75), (C70.90), (C70.130) and (C70.200).



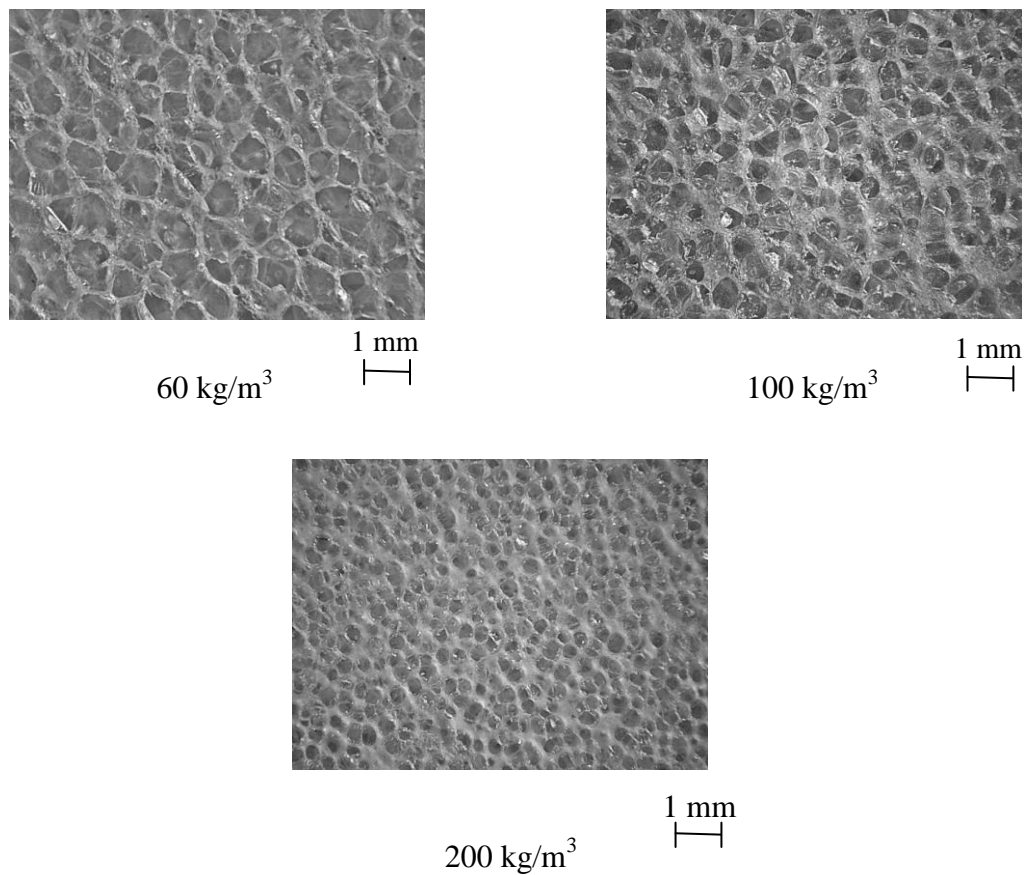


**Figure 4.4** Photos of the surfaces of typical crosslinked PVC (C75.55), (C70.90) and (C70.200) foams.

**Figure 4.5** shows typical stress strain plots following quasi-static tests on the linear PVC foams R63.80 and R63.140. For both foams, the material exhibits an initial linear response before reaching a peak, followed by stress drop and a long plateau regime and finally a densification phase. The static compressive strengths,  $\sigma_{pl}$ , of the R63.80 and R63.140 foams, were found to be 0.98 and 1.6 MPa respectively, as shown in **Figure 4.5**. These values agree with the mechanical properties in the manufacturer's data sheets. The value of  $\sigma_{ss}$  for the R63.80 foam was approximately 75 % lower than that for the R63.140 grade, highlighting the presence of the stronger and stiffer cell structures in the higher density foam. Also, as the

density of the linear PVC foam increases from 90 to 140 kg/m<sup>3</sup>, the value of  $\epsilon_D$  decreased by approximately 4 %, reducing the length of the steady-state stress region.

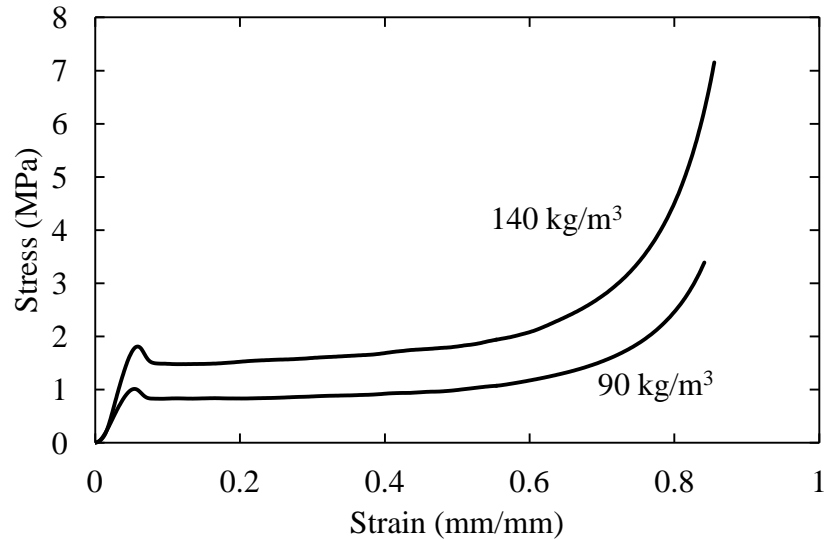


**Figure 4.5** Typical stress-strain curves following quasi-static tests on the linear PVC R63.80 and R63.140 foams.

The T92.100 and T92.130 PET foams were also tested under quasi-static compression loading. **Figure 4.6** shows that once again these foams exhibit three distinct regions; an elastic regime up to an initial peak, followed by a plateau stress, and then a final phase of densification.

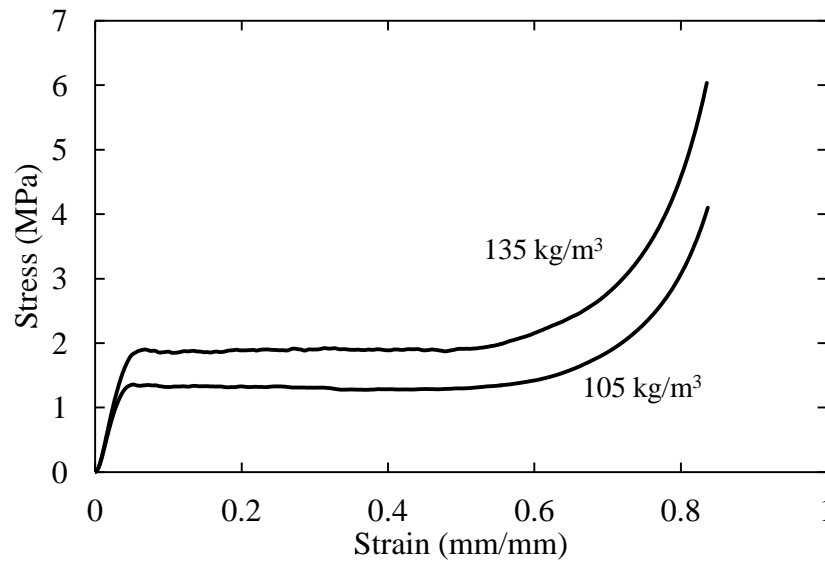


**Figure 4.6** Typical stress-strain plots following quasi-static tests on the PET T92.100 and PET T92.130 foams.

Again, it is clear that increasing the density of the foam is associated with an increase in the value of  $\sigma_{pl}$  and  $\sigma_{ss}$ . It is evident that the T92.130 foam shows a higher plastic collapse stress than the T92.100 grade. However, the length of the steady-state stress region decreases with increasing density. Here, the value of  $\varepsilon_D$  decreased by approximately 2 % as the density of the foam increased.

**Figure 4.7** summarizes the variation of the average values of  $\sigma_{pl}$  with density for nine foams at quasi-static rates of loading. It is clear that the value of  $\sigma_{pl}$  for all types of foam increase with increasing density. Recent work by Tagarielli *et. al.*(4) showed the peak stress increases according to a power law relationship as the foam density increases. From the figure, it is evident that the crosslinked PVC is superior to the linear PVC foam. Lim *et. al.* (5) found that crosslinked PVC foams have a characteristically higher yield stress than linear PVC foams. Material crosslinking was introduced by adding certain additives to PVC during the polymerization phase, resulting in higher mechanical properties than those of the linear PVC

foams. The data presented in **Figure 4.7** also show that the value of  $\sigma_{pl}$  for the crosslinked PVC foam is approximately 30 % higher than that for the PET foam.

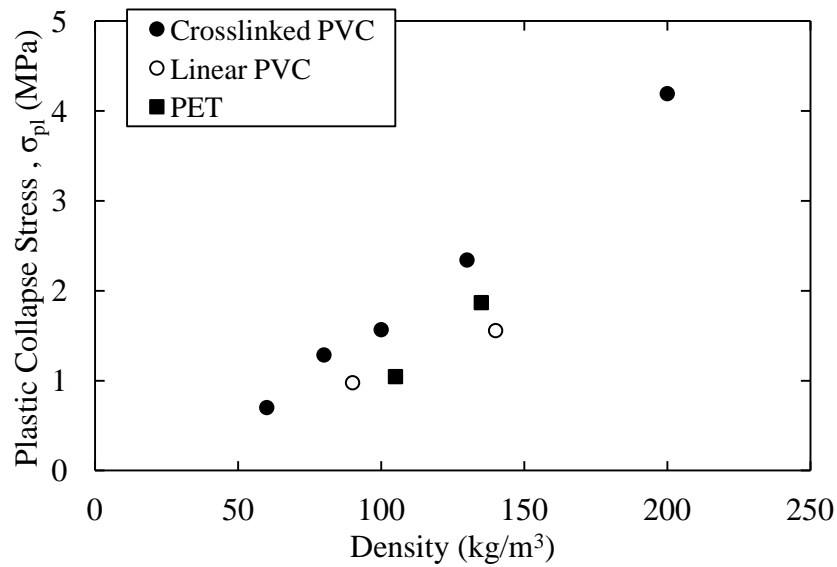


**Figure 4.7** The variation of plastic collapse stress with density for different foams.

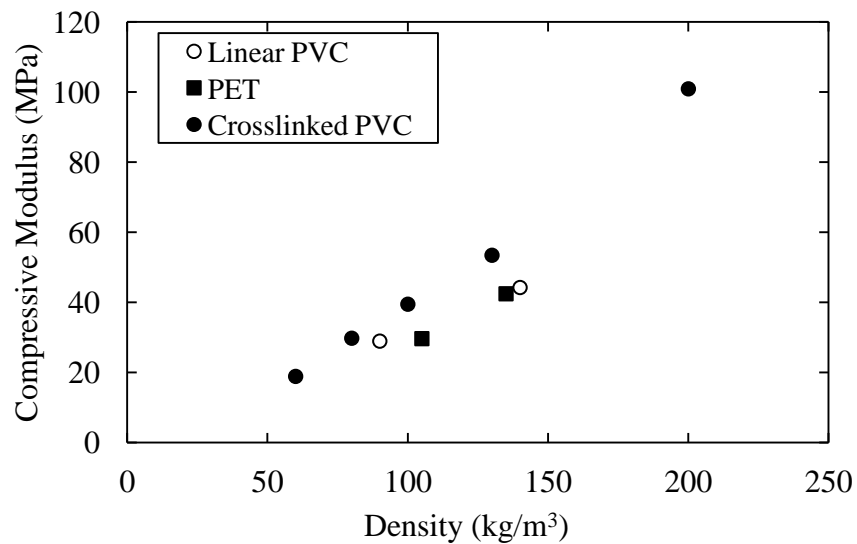


**Figure 4.8** The variation of compressive modulus with density for different foams.

**Figure 4.8** presents variation of compressive modulus with density for the crosslinked PVC, the linear PVC and the PET foams. All of the foam materials exhibit an increasing compressive modulus with increasing foam density. In addition, the crosslinked PVC foams offer a greater compressive modulus than either of the linear PVC and PET foams. Surprisingly, the linear PVC and PET foams exhibit similar value of compressive modulus for a given density.

**Figure 4.9** shows the variation of the steady state stress with density for the crosslinked PVC, the linear PVC and the PET foams. All foams show a trend of increasing steady-state stress with increasing foam density. In addition, the steady-state stress values of PET foams fall between those of the crosslinked PVC and PET foams.

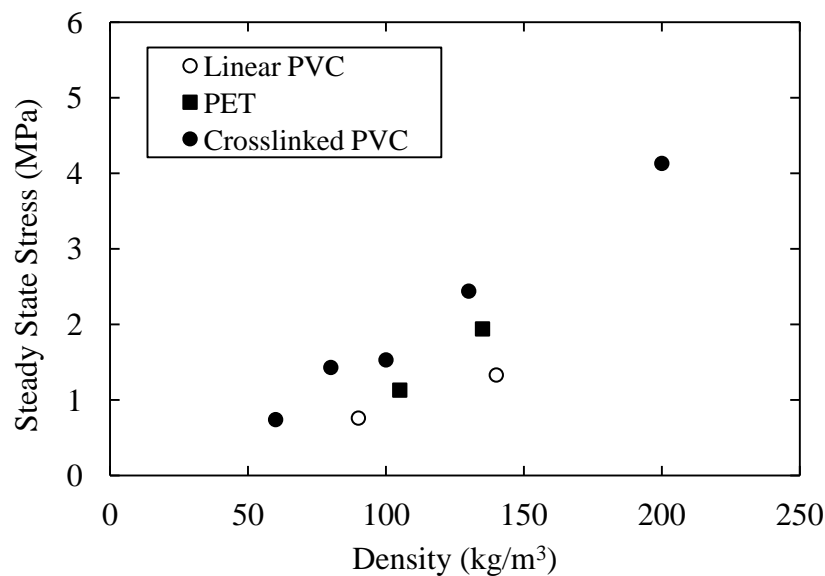


**Figure 4.9** The variation of steady-state stress with density for different foams.

#### 4.1.1.2 Compression Behaviour of the Linear PVC (HD 130), Crosslinked PVC (H 130), SAN (A500) and PMI (WF 71) Foams

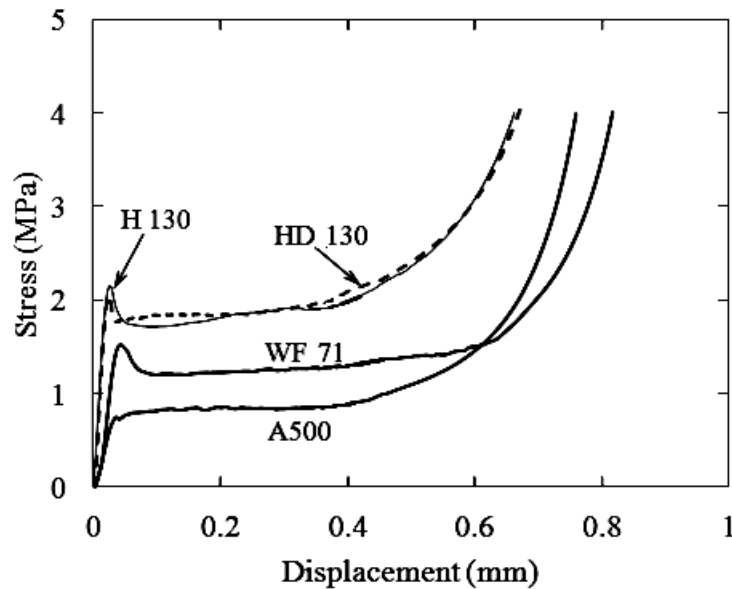


**Figure 4.10** Typical stress-strain plots following quasi-static tests on a crosslinked (H 130), a linear (HD 130), a SAN (A500) and a PMI (WF 71) foams.

**Figure 4.10** shows engineering stress-strain plots for the linear PVC (HD 130), the crosslinked PVC (H 130), the SAN (A500) and the PMI (WF 71) foams and their mechanical properties are tabulated in **Table 4.2**. As shown in **Figure 4.10**, three of the foams undergo five phases of deformation: initial elastic compression, yielding, strain-softening, due to extensive buckling, a steady state stress and finally densification. The exception to this is the A500 foam. The value of  $\sigma_{pl}$  was found to be 1.91, 2.22, 1.53 and 0.87 MPa for the crosslinked PVC (HD 130), linear PVC (H 130), PMI (WF 71) and SAN (A500) foams respectively. The plateau region is was roughly horizontal for the all foams prior to densification. In addition, the values of  $\sigma_{ss}$  and  $\varepsilon_D$  are more pronounced in the WF 71 foam than in the A500 foam. The plateau stress values for both the linear H 130 and crosslinked

HD 130 foams are similar, suggesting that crosslinking does not have a significant effect in these systems.

Foam	Density (kg/m <sup>3</sup> )	Plastic collapse stress, $\sigma_{pl}$ (MPa)	Compressive modulus, $E_c$ (MPa)	Steady state stress, $\sigma_{ss}$ (MPa)	Densification strain, $\varepsilon_D$ (%)
HD 130	130	1.91	121.65	1.78	53.03
H 130	130	2.22	107.45	1.84	53.42
A500	92	0.87	39.46	0.78	54.56
WF 71	75	1.53	76.87	1.12	60.21

**Table 4.2** Summary of the average mechanical properties of the linear PVC (HD 130), the crosslinked PVC (H 130), the SAN (A500) and the PMI (WF 71) foams.

#### 4.1.1.3 Compression Behaviour of the PP Honeycomb, the Paperboard and the Aluminium Honeycomb Sandwich Structures

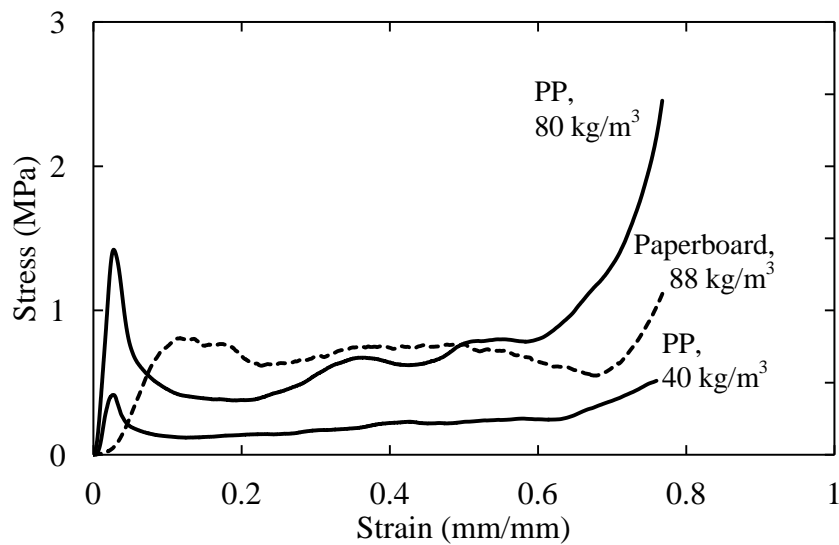


**Figure 4.11** Quasi-static compression tests on the 40 and 80 kg/m<sup>3</sup> PP honeycombs and the 88 kg/m<sup>3</sup> paperboard.

The stress-strain responses of the 40 and 80 kg/m<sup>3</sup> PP honeycombs at a quasi-static loading rate are presented in **Figure 4.11**. Here, it was observed that up to the maximum stress level, the stress-strain curves are reasonably linear. After the maximum, the cell walls collapse and a large drop in the stress occurs. Closer examination indicated that the cause of the drop was bending and local buckling of the cell walls. The load continued to increase gently after this initial drop. This increase in load capacity is associated with the densification of the folded cell walls. It is evident in **Figure 4.11**, that the denser PP honeycomb exhibits a higher strength. It was found that an increase in the density from 40 to 80 kg/m<sup>3</sup> increased  $\sigma_{pl}$  by approximately 220 %. The value of  $\sigma_{ss}$  for the 80 kg/m<sup>3</sup> PP honeycomb was approximately three times higher than the 40 kg/m<sup>3</sup> grade, highlighting that the stiffer cell wall structures in the higher density PP honeycomb. In contrast, the value of  $\varepsilon_D$  was approximately 61.4 % for both densities. **Figure 4.11** also includes a nominal stress-strain curve for the paperboard structure, where that the measured value of  $\sigma_{pl}$  is 0.9 MPa, a value that lies between those for the low and high density PP honeycombs. However, the value of  $E_c$  for paperboard core is between 240 % and 530 % lower than that for the 40 and 80 kg/m<sup>3</sup> PP honeycombs respectively.

Compression tests were also carried out on an aluminium honeycomb sandwich structure to benchmark the properties of the systems tested here. A typical stress-strain curve for this material is shown in **Figure 4.12**. The aluminium honeycomb exhibits four phases of deformation; an initial elastic region, yielding, which is then followed by an extensive soft-hardening and plateau region, caused by plastic yielding and bending of the cell walls. Further loading, then causes densification and a rapid rise in stress. The average values of  $E_c$  and  $\sigma_{pl}$  were approximately 239.5 MPa and 5.1 MPa respectively. The experimental data obtained from the tests on the PP honeycomb, the paperboard and the aluminium honeycomb sandwich structure are summarised in **Table 4.3**.



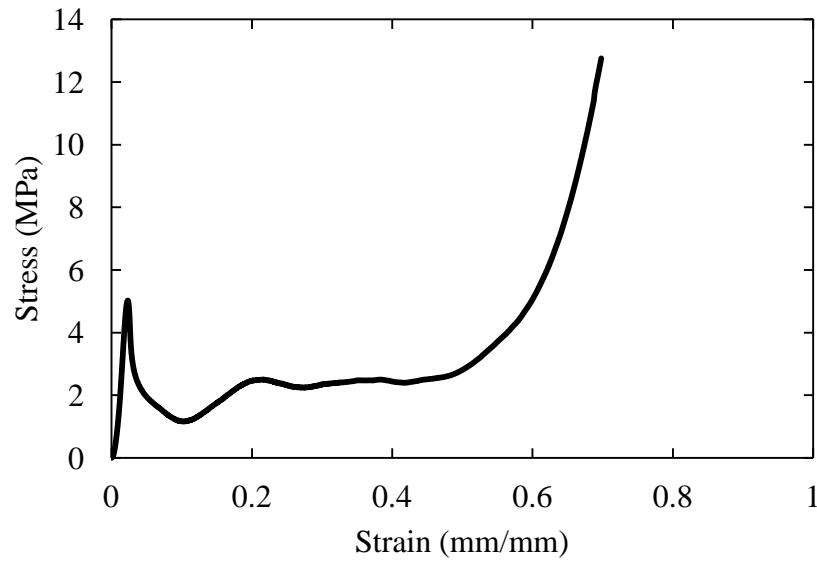


**Figure 4.12** A compressive stress-strain curve for an aluminium honeycomb sandwich structure.

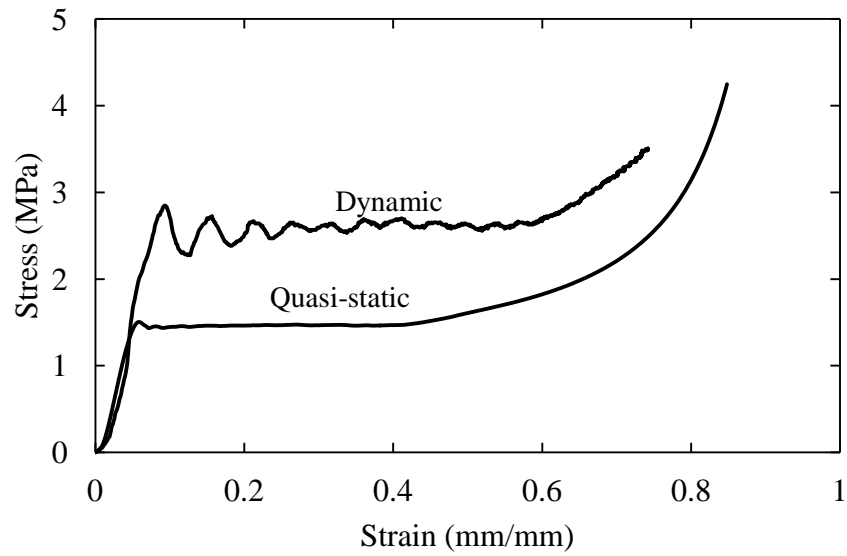
Material system	Density (kg/m <sup>3</sup> )	Plastic collapse stress, $\sigma_{pl}$ (MPa)	Compressive modulus, $E_c$ (MPa)	Steady state stress, $\sigma_{ss}$ (MPa)	Densification strain, $\epsilon_D$ (%)
PP	40	0.41	34.3	0.24	61.4
PP	80	1.31	62.5	0.61	61.4
Paperboard	88	0.87	10.9	0.82	66.6
GFRP/Al honeycomb	260	5.13	239.5	2.35	48.3

**Table 4.3** Summary of the average mechanical properties of the 44 and 86 kg/m<sup>3</sup> PP honeycomb, the paperboard and the aluminium honeycomb sandwich structures.

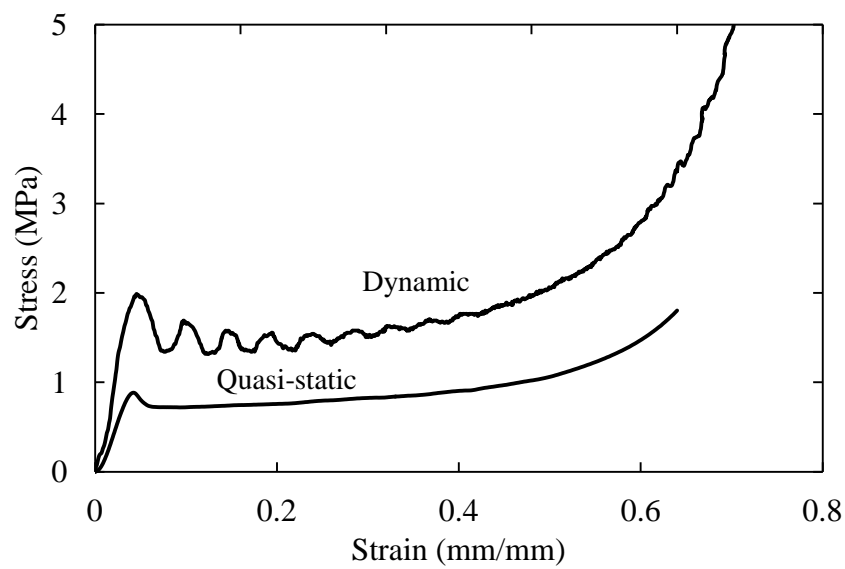
### 4.1.2 The Compression Behaviour of the Foams at Higher Strain Rates

Higher strain rate tests were performed using a drop-weight impact tower. Here, a 50 mm circular disc was fitted to the impact carriage to load the foam cubes, which were supported on the solid steel base. Masses of approximately 6 kg were dropped from heights of up to 1.2 metres to load the specimens. A 35 kN load cell located between the mass and the circular disc was used to record the force-time history, while a high-speed camera was used to measure the displacement-time trace.

Typical stress-strain curves for the C70.90 and R63.80 foams at both quasi-static and dynamic rates of strain are shown in **Figure 4.13**. In general, a significant increase in  $\sigma_{pl}$  was observed at higher rates of strain. In contrast, the value of  $E_c$  of the foam was largely unaffected by increasing strain rate. As shown in **Figure 4.13**, the energy absorbed by the foam also increased significantly with increasing strain rate. A considerable amount of energy is absorbed through the collapse of the cell walls in the stress plateau region. There is also a pronounced increase in the value of  $\sigma_{ss}$  with increasing strain rate. However, the curve exhibits strong oscillations, largely due to ringing in the load cell. This phenomenon becomes more pronounced with increasing density, making the calculation of the value of  $\sigma_{ss}$  somewhat difficult.



(a)



(b)

**Figure 4.13** Dynamic and quasi-static stress-strain curves for the (a) crosslinked PVC C70.90 and (b) linear PVC R63.80 foams.

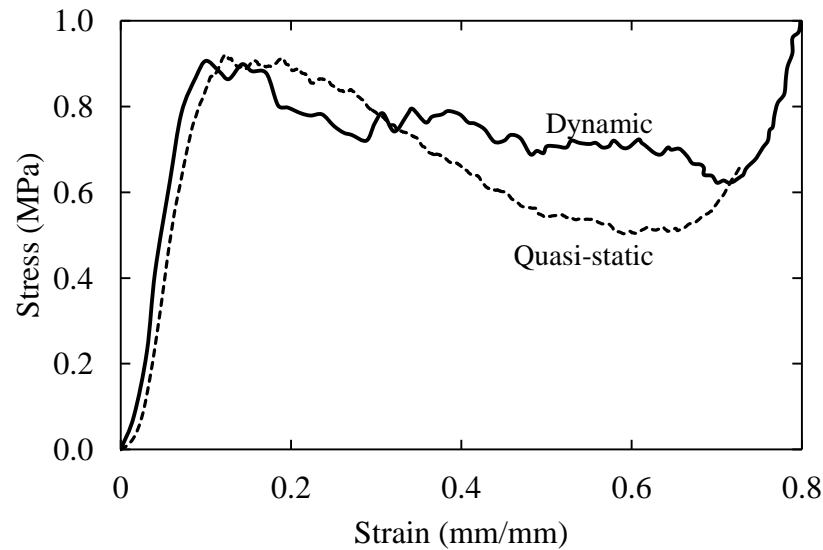


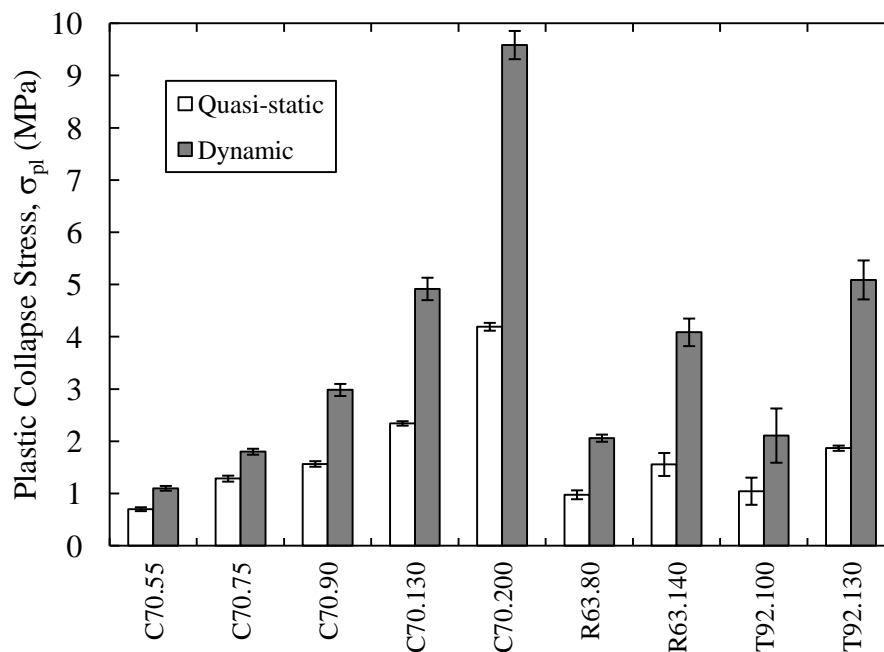
**Figure 4.14** Typical load-displacement traces for corrugated paperboard following dynamic and quasi-static tests.

**Figure 4.14** shows the quasi-static and dynamic stress-strain responses for the corrugated paperboard. There is no significant rate effect apparent in the data, with the plastic collapse stress and compressive modulus being similar. Similar observations were also made for the 40 and 80 kg/m<sup>3</sup> PP honeycomb structures over this range of loading rates.

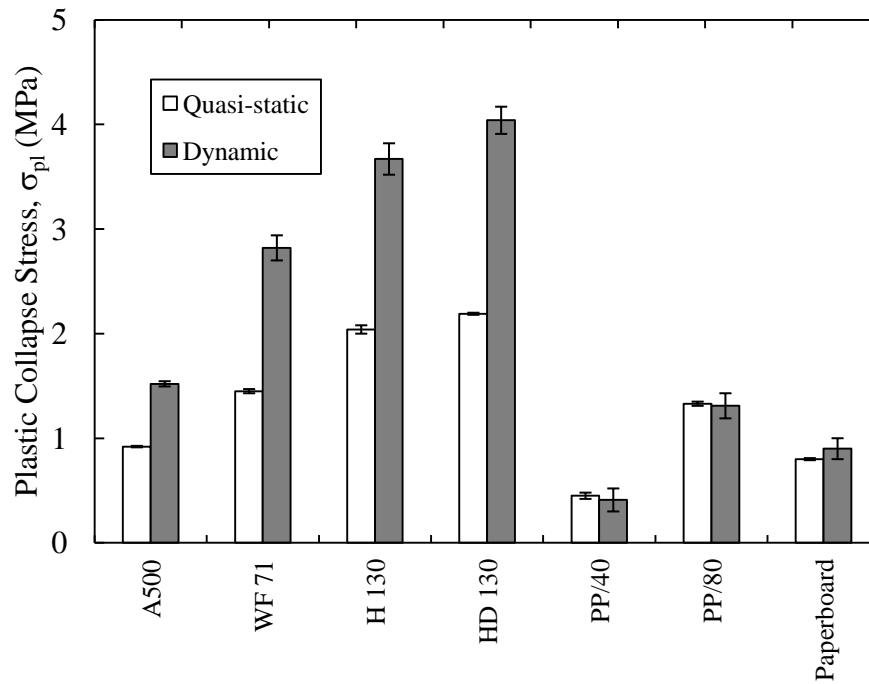
The compressive response of the thirteen foams tested here are summarised in the form of a bar chart in **Figure 4.15(a)**, where a number of observations can be made. Firstly, as previously mentioned, the plastic collapse strength increases with foam density. This is clear in the data for the crosslinked PVC foams, where an increase in the nominal density from 60 to 200 kg/m<sup>3</sup> resulted in a five fold increase in the plastic collapse stress. The linear PVC foams offer lower strength values than their crosslinked counterparts, a clear reflection of the effect of introducing crosslinks into the polymer foam.

The PET (T92), SAN (A.500), linear PVC (H 130), crosslinked PVC (HD 130) and PMI (WF 71) foams appear to exhibit compression properties that lie between those of the linear PVC

(R63) and crosslinked PVC (C70) foams as shown in **Figure 4.15(b)**. The bar chart also highlights the strain-rate sensitivity of the various types of foam, with all systems exhibiting an increase in compression properties at higher rates. A cursory examination of the data indicates that the strain-rate sensitivity increases with foam density, with the dynamic compression strength of the highest density foam being more than double that of its quasi-static value. The observation agrees with the findings of previous researchers who have established that rate-sensitivity is closely linked to foam density (6, 7). This evidence suggests that it is very important to use the dynamic properties of a foam when attempting to model the impact or blast resistance of sandwich structures. In contrast, there is no clear rate effect in the 40 and 80 kg/m<sup>3</sup> PP honeycomb and paperboard structures over the range of loading rates considered here.



(a)



(b)

**Figure 4.15** Summary of the quasi-static and dynamic plastic collapse stress values of (a) the crosslinked PVC (C70), the linear PVC (R63) and the PET (T92) and (b) the SAN (A500), the linear PVC (H 130), the crosslinked PVC (HD 130) foams, the 40 and 80 kg/m<sup>3</sup> PP honeycomb and the paperboard structures.

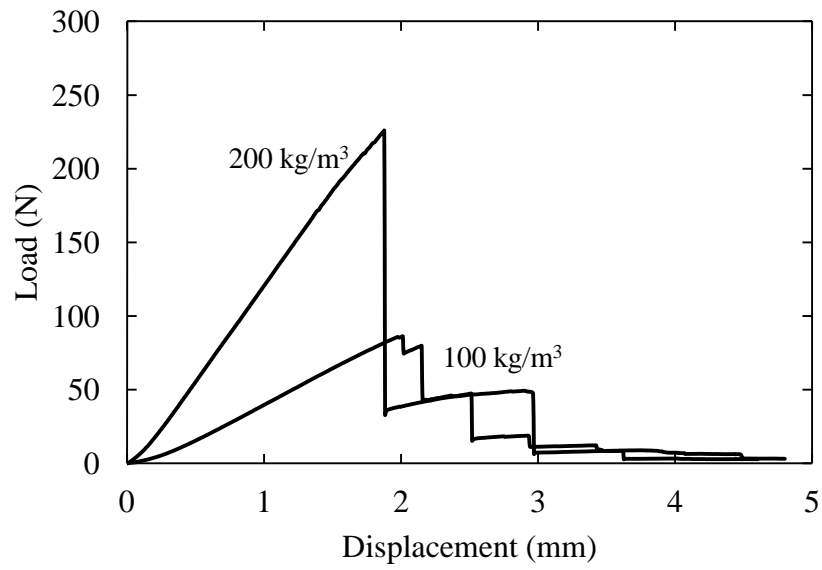
### 4.3 Single End Notch Bend Test – Mode I

Rate effects in the Mode I fracture properties of the foams were investigated through a series of single end notch bend (SENB) tests. Nine foams, with length, depth and thickness dimensions of 150, 30 and 20 mm respectively, were tested under quasi-static and dynamic rates of loading. Prior to testing, a 10 mm notch was introduced in the middle of the specimen length using a sharp blade. The fracture toughness values of the foams was characterised by determining the work of fracture from the area under the load displacement curve and the area of the fracture ligament.

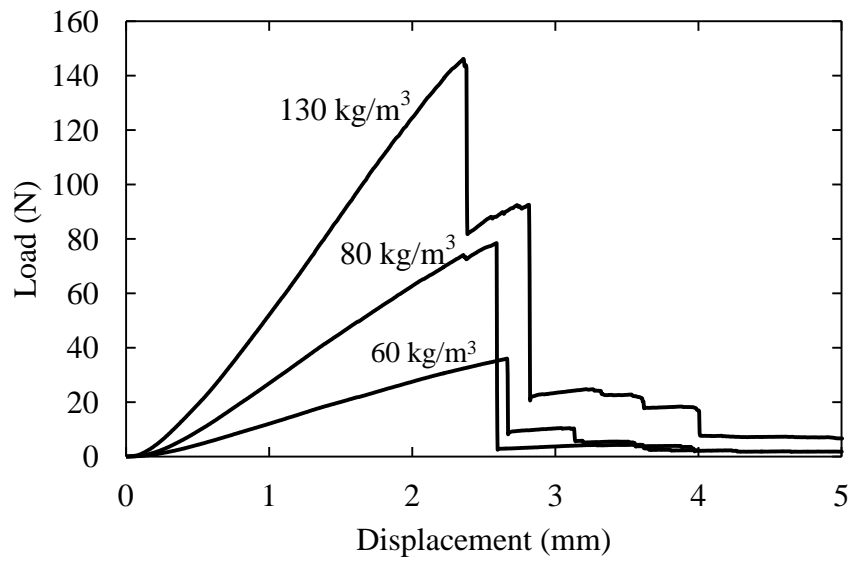
### 4.3.1 The Effect of Foam Density on the Toughness of the Foams

Quasi-static SENB tests were conducted at a loading rate of 10 mm/min using an Instron testing machine. **Figure 4.16** shows typical load-displacement plots for two crosslinked PVC foams. An examination of the figure indicates that these crosslinked PVC foams failed in a relatively brittle manner, for which the curves are smooth, deviating slightly from linearity before reaching the maximum load, and dropping sharply as the crack propagates upwards through the polymer. Similar behaviour was observed in the other crosslinked foams. Comparing the peak load values for the C70.200 and C70.90 foams, it can be seen that an increase in foam density from 100 to 200 kg/m<sup>3</sup> increases the peak load by more than a factor of three, as shown in **Figure 4.16(a)**. The saw tooth appearance in the traces is associated with the crack arresting before subsequently propagating in an unstable manner. The dynamic load-displacement traces for the crosslinked PVC were similar in appearance to the quasi-static plots, again highlighting a relatively brittle mode of failure.

In contrast, the PET foams exhibited a mixed failure mode, with the load increasing in a highly non-linear fashion before reaching the maximum load and suddenly dropping, as shown in **Figure 4.17**. Again, the peak load increases and the maximum displacement reduces with increasing foam density of the foam.



(a)



(b)

**Figure 4.16** Typical load-displacement traces following Mode I SENB test on crosslinked PVC (a) C70.200 and C70.90 (b) C70.55, C70.75 and C70.130 foams.



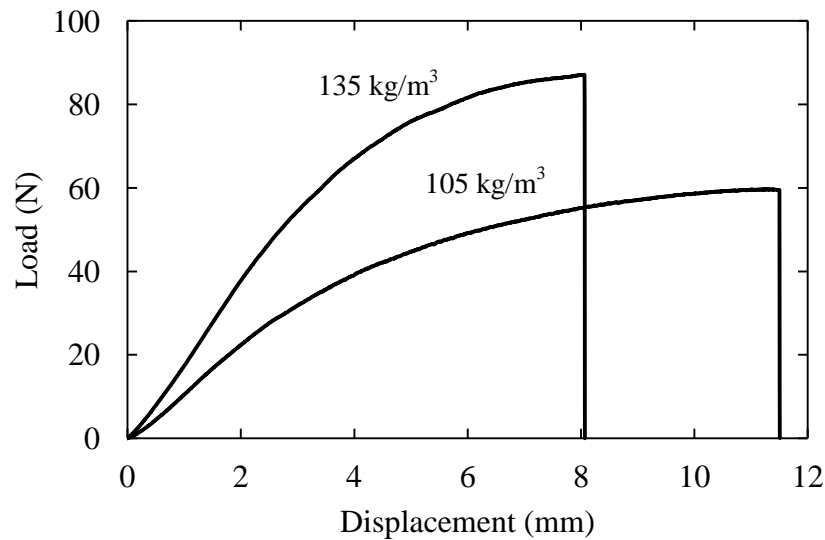


**Figure 4.17** Typical load-displacement traces following Mode I SENB tests on the PET T92.100 and T92.130 foams.

**Figure 4.18** present the influence of foam density on the Mode I work of fracture of the crosslinked PVC, linear PVC and PET foams. As observed from the figure, the fracture toughness of the crosslinked PVC shows a linear dependence on density tending to increase with increasing of the density. The result show that of the three foams tested, the crosslinked PVC foams offers the lowest value of fracture toughness for a given density. In addition, the linear PVC foams offer values of work of fracture for greater than those exhibits by the two other foams. For example, the linear PVC foam, with a density of  $140 \text{ kg/m}^3$ , exhibited a value of  $4.37 \text{ kJ/m}^2$ , compared to the values of  $0.88 \text{ kJ/m}^2$  for the  $130 \text{ kg/m}^3$  crosslinked PVC and  $0.39 \text{ kJ/m}^2$  for the  $135 \text{ kg/m}^3$  PET foam. These findings suggest the Mode I fracture toughness is not only influenced by density but also dependent of the type and manufacture of the foams.

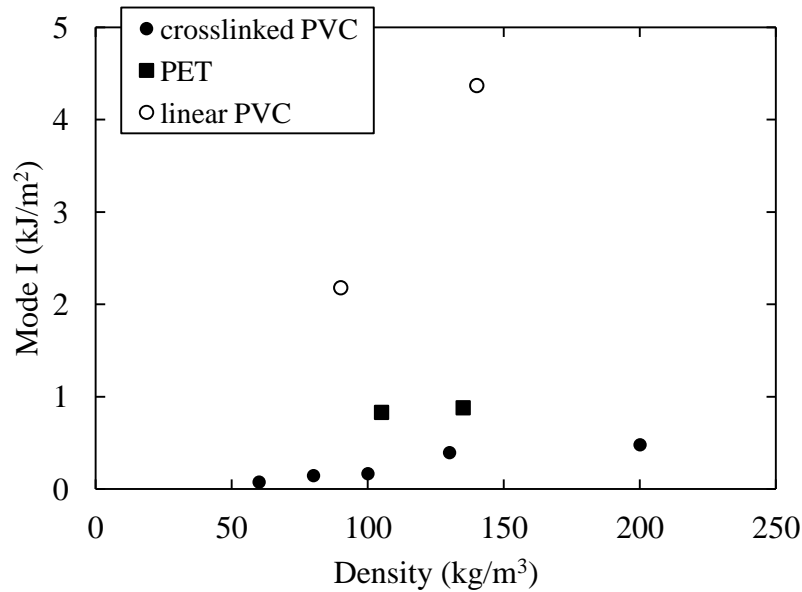


**Figure 4.18** Summary of foam density on the work of fracture of the crosslinked PVC, the linear PVC and the PET foams.

### 4.3.2 The Effect of Crosslinking on Foam Toughness

Typical load-displacement traces following Mode I tests on the crosslinked PVC and linear PVC foams, namely, the C70.90 and R63.80 foams respectively, are shown in **Figure 4.19**. These two types of foam were chosen because they have similar densities, these being 100 kg/m<sup>3</sup> and 90 kg/m<sup>3</sup> respectively. As observed, the peak load and maximum displacement for R63.80 foam is higher than the C70.90 foam, suggesting that the linear PVC offers much higher fracture toughness. Crack propagation in the linear PVC system was much slower, indicating that this foam is intrinsically tougher material than that crosslinked PVC foam.

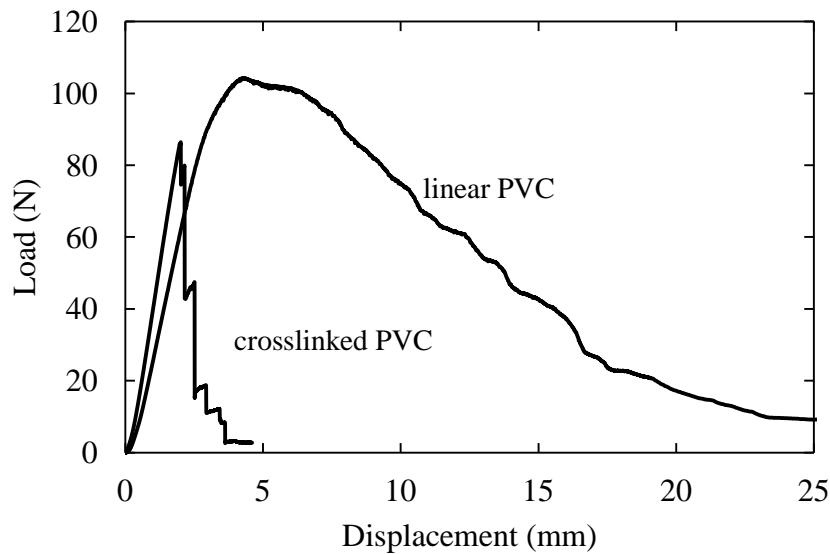


**Figure 4.19** Typical load-displacement traces following Mode I SENB tests on the crosslinked PVC C70.90 and the linear PVC R63.80 foams.

### 4.3.3 The Effect of Loading Rate on the Toughness

**Figure 4.20** presents typical load versus displacement traces for quasi-static and dynamic loading of the R63.140 foam. The dynamic curve contains some small oscillations before reaching a peak load of approximately 250 N, followed by dramatic drop in load. The sudden drop in load is attributed to unstable crack propagation in the specimen. **Figure 4.20** shows that the load-displacement curve for quasi-static loading is non-linear with the peak load being lower than under dynamic loading. It can be seen that the maximum displacement is more than 50 mm, while the thickness of the fractured ligament is only 20 mm. This large deformation is due to the highly ductile behaviour of the linear PVC foam under quasi-static loading.

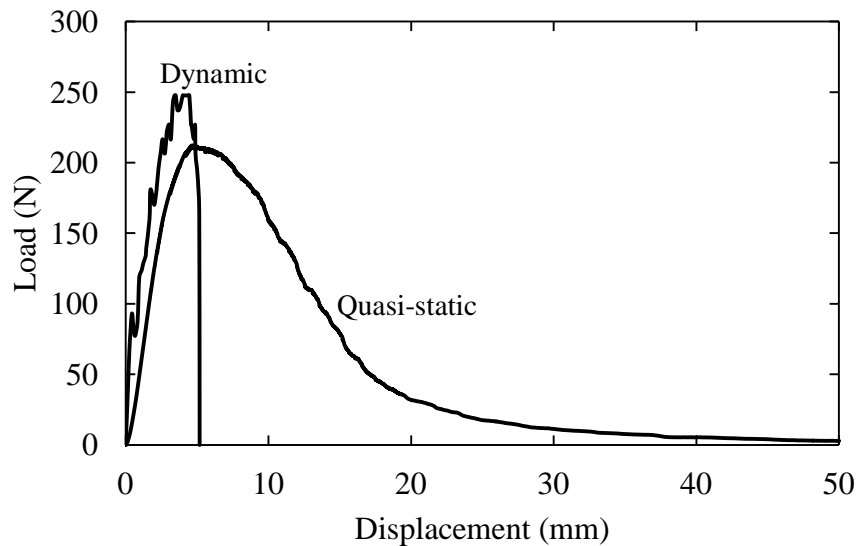
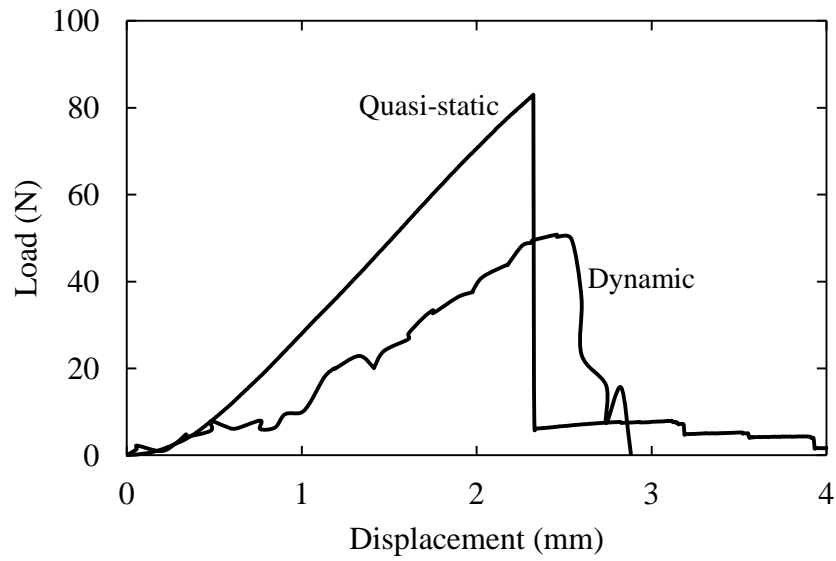
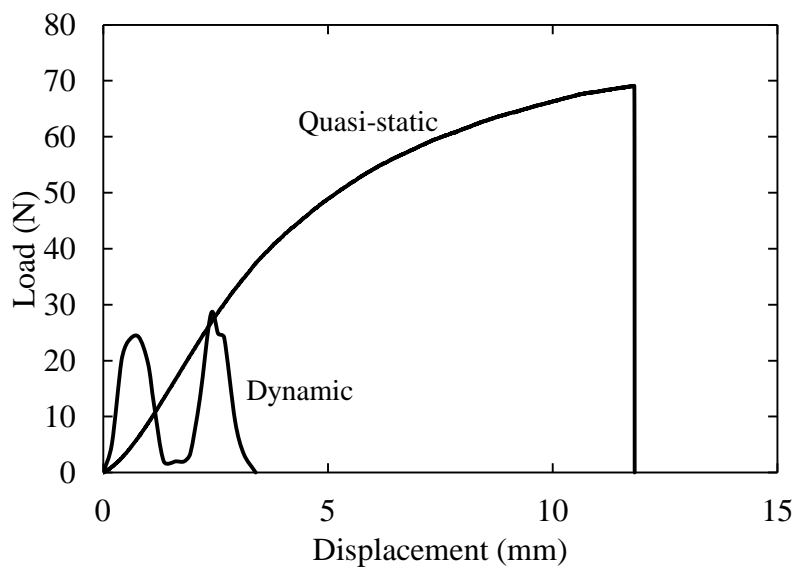


**Figure 4.20** Typical load displacement traces following Mode I (SENB) testing of the linear PVC foam (R63.140).

Typical load displacement curves for quasi-static and dynamic tests on the crosslinked PVC and PET foams are presented in **Figure 4.21**. From **Figure 4.21(a)**, it is clear that the peak load and the maximum displacement following quasi-static testing is higher than dynamic testing suggesting that under quasi-static conditions, the crosslinked-PVC foams offer a much higher fracture toughness. **Figure 4.21(b)** shows the load-displacement for the highest density PET foam following quasi-static and dynamic loading. Under dynamic testing, the PET foam exhibits two distinct peaks in the load displacement trace. Interestingly, the PET foams failed in a brittle mode at higher loading rates, with the maximum load and displacement values being lower than those measured at quasi-static rates. The reason for this trend is not clear, however, it is possible that it is associated with the crack jumping from cell to cell within the PET foam.



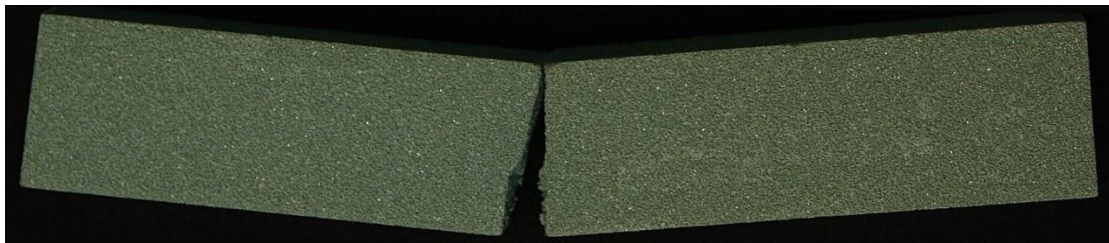
(a)



(b)

**Figure 4.21** Typical load displacement traces following Mode I testing of the crosslinked PVC (C70.75) and PET (T92.130) foams.

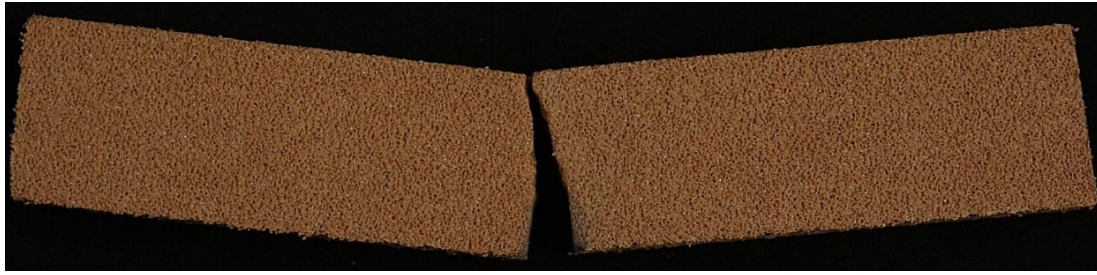
**Figure 4.22** shows typical failed SENB samples following quasi-static and dynamic tests on the 130 kg/m<sup>3</sup> crosslinked PVC, the 135 kg/m<sup>3</sup> PET and the 140 kg/m<sup>3</sup> linear PVC foams. An examination of **Figure 4.22(a)** indicates an unstable opening of the pre-crack in 130 kg/m<sup>3</sup> crosslinked PVC foam, which offered a value of work of fracture of 395 J/m<sup>2</sup>. This helps to explain the absence of a zig-zag in the load-displacement curve, as shown in **Figure 4.16(b)**. In contrast, stable crack propagation was observed in the 135 kg/m<sup>3</sup> PET foam, as shown in **Figure 4.22(b)** which offered a work of fracture of 885 J/m<sup>2</sup>. Interestingly, the 140 kg/m<sup>3</sup> linear PVC offers an impressive work of fracture of 3800 J/m<sup>2</sup> and also exhibited significant pre-crack opening after fracture (**Figure 4.22(c)**). Similar findings were reported by Hazizan (8). **Figures 4.22(d), (e) and (f)** show cross-sections of the 130 kg/m<sup>3</sup> crosslinked PVC, the 135 kg/m<sup>3</sup> PET and the 140 kg/m<sup>3</sup> linear PVC foams following dynamic testing. Damage is similar to that observed following quasi-static testing, involving crack propagation towards the top surface, i.e. the point of loading.



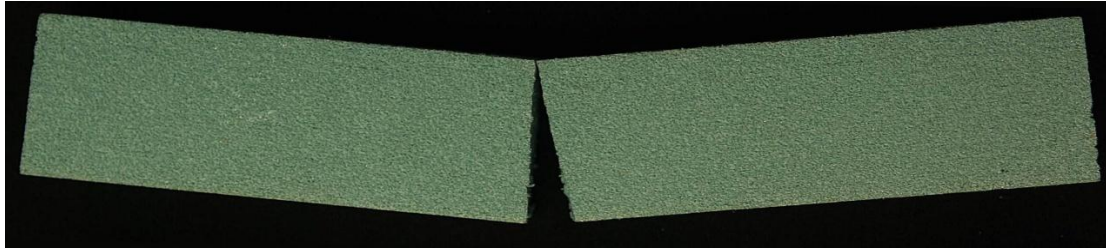
(a)



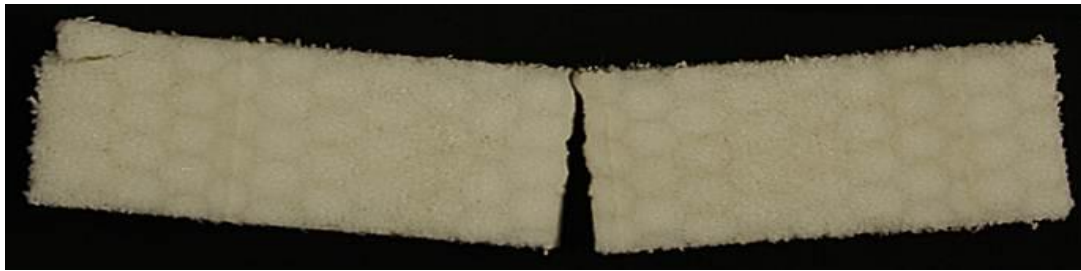
(b)



(c)



(d)



(e)



(f)

5 mm

**Figure 4.22** Photos of typical failed SENB samples following quasi-static testing on the (a)  $130 \text{ kg/m}^3$  crosslinked PVC, (b)  $135 \text{ kg/m}^3$  PET, (c)  $140 \text{ kg/m}^3$  linear PVC foams and dynamic testing on the (d)  $130 \text{ kg/m}^3$  crosslinked PVC, (e)  $135 \text{ kg/m}^3$  PET (f)  $140 \text{ kg/m}^3$  linear PVC foams.

The Mode I work of fracture data for the crosslinked PVC, linear PVC and PET foams at the quasi-static and dynamic rates of loading are shown in **Figure 4.23**. It should be noted that the data for linear PVC (R63.140) has not been included, since its high value of  $4,366 \text{ J/m}^2$  distorts the figure. An examination of the figure highlights the impressive toughness of the linear PVC and PET foams. Indeed the value in excess of  $4 \text{ kJ/m}^2$ , for the higher density linear PVC foam, highlights the extraordinary toughness of this system. In general, it was found that the Mode I work of fracture data decreases with increasing loading rate. The rate-sensitivity is most pronounced in the PET foams, where the dynamic values are significantly lower than those measured quasi-statically. It is also evident that the linear PVC foams suffer a reduction in toughness at higher rates, although this is not as significant as that observed in the PET foams. The values of the work of fracture measured here are in line with those reported by Hazizan (8) as shown in **Figure 4.24**.

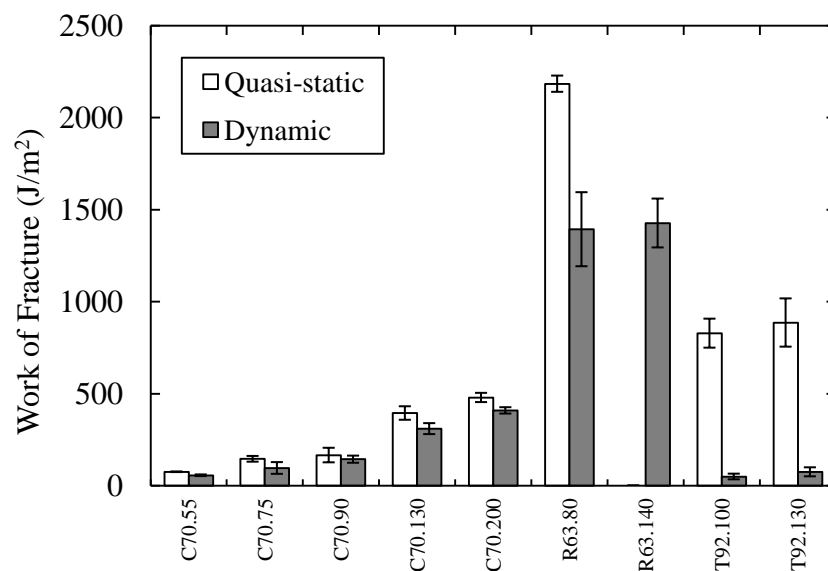


**Figure 4.23** Mode I work of fracture values for the linear and crosslinked PVC foams as well as the PET tested in quasi-static and dynamic loading.



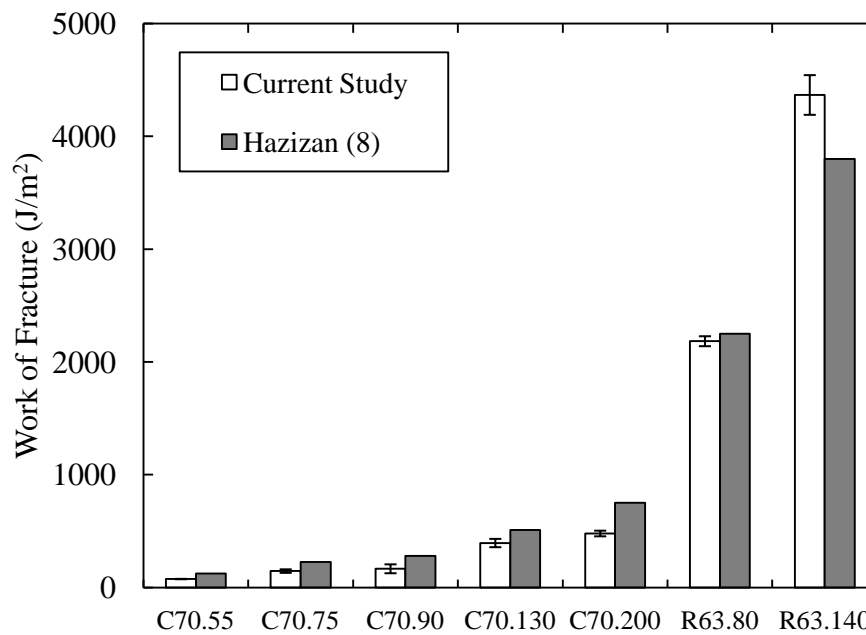


**Figure 4.24** Comparison of the measured work of fracture values of the foams with published data (8).

**Table 4.4** shows the fracture toughness values for the various types of foam. Kabir *et. al* (9) used the ASTM D5045 standard for determining the fracture toughness of crosslinked, linear PVC and polyurethane (PU) foams. They reported that the stress intensity factor,  $K_{Ic}$ , increased by 18 % when the loading rate was increased by two orders of magnitude. Interestingly, the value of  $K_{Ic}$  for the crosslinked PVC (HD 130) is higher than linear PVC (H 130) for all three loading rates investigated. Recent work by Marsavina *et. al.* (10) on notched and un-notched PU foam using an instrumented Charpy impact test is also included. The energy absorbed to fracture was calculated based on the area under the force-displacement curve. They showed that the energy for fracture decreased with increasing loading rate. Comparing these finding with the current work, the work of fracture for the foam decreases with increasing loading rate, while the work of fracture for the linear PVC foam is higher

than the crosslinked PVC foam. Once again, this evidence suggests that when analysing structures based on polymer foams, it is important to use the appropriate fracture data.

	Type of foam						
	HD 130 <sup>*</sup>	H 130 <sup>*</sup>	R.75 <sup>*</sup>	R.260 <sup>*</sup>	PU <sup>**</sup>	C70.130	R63.140
Density [kg/m <sup>3</sup> ]	130	130	75	260	200	130	140
Loading rate [mm/s]	Stress intensity factor, $K_{Ic}$ [MPa.m <sup>0.5</sup> ]				Energy absorbed to fracture (J)	Work of fracture (kJ/m <sup>2</sup> )	
0.017						0.4	4.3
0.0245	0.3	0.22	0.09	0.66			
0.0833					0.72		
0.245	0.34	0.23	0.1	0.72			
2.45	0.36	0.24	0.11	0.78			
1400						0.31	1.4
3815					0.57		

Note : \* Kabir *et. al* (9) and \*\* Marsavina *et. al.* (10)

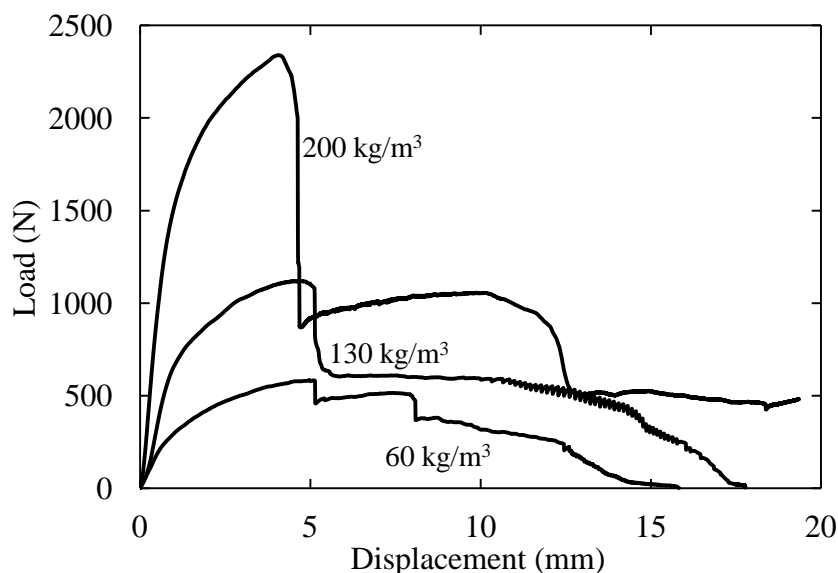
**Table 4.4** Comparison of the fracture properties for various foams.

#### 4.4 Shear Tests – Mode II

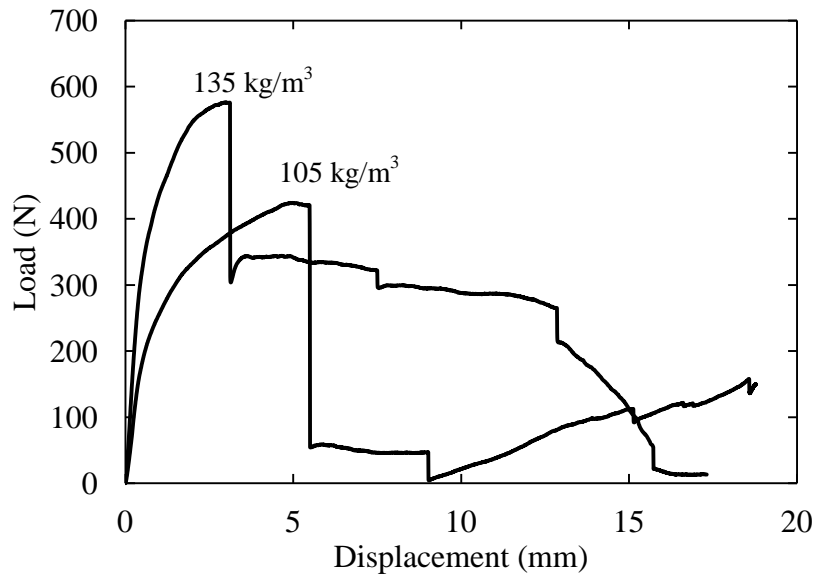
The fracture properties of the foam in Mode II (shear) were determined using a specially designed test rig in which notched specimens, with dimensions 80, 30, 20 mm, were clamped at one end and loaded in a shearing mode by a steel traverse. The notch length was 10 mm and testing was conducted at 10 mm/min. As before, the work of fracture was determined from the area under the load displacement trace and the area of the fractured ligament.

#### 4.4.1 The Effect of Foam Density on the Mode II Work of Fracture Properties

Typical load-displacement traces following Mode II tests on three crosslinked PVC foams are shown in **Figure 4.25(a)**. All traces exhibit a similar appearance, with the load increasing in a non-linear manner to the maximum load followed by unstable crack propagation. The non-linearity in the initial portion of the load-displacement traces is associated with the plastic deformation directly under the steel loading cylinder. It can be seen from **Figure 4.25(a)**, that loading often resulted in micro-instabilities, this being most evident in the crosslinked PVC C70.130, where very small crack jumps are apparent in the trace at displacements above 10 mm. The linear PVC foams exhibited a stable mode of crack growth, with the load increasing slowly to a maximum before gradually reducing until complete fracture of the sample. The PET foams displayed an initial non-linear response before reaching maximum load. An examination of **Figure 4.25(b)** indicates that the crack does not propagate at a steady rate, but in a stick-slip mode, involving relatively small periods of unstable crack propagation. As before, increasing the foam density serves to increase the maximum load recorded during the test.



(a)



(b)

**Figure 4.25** Typical load-displacement traces following Mode II SENB tests on (a) the crosslinked C70.200, C70.130, C70.55 PVC foams and (b) the T92.130, T92.100 PET foams

#### 4.4.2 The Effect of Crosslinking on the Mode II Properties of The Foams

**Figure 4.26** shows representative load-displacement traces for the linear PVC R63.80 and the crosslinked PVC C70.90 foams, both of which exhibit a non-linear response before reaching the maximum load. However, the R63.80 foam exhibited a more ductile fracture behaviour than the C70.90 foam. This ductility is evidenced by the longer shear deformation zone for the R63.80 system as shown in **Figure 4.26**, where the elongation of the R63.80 foam was approximately four times that of the C70.90 foam. This large difference in plastic deformation is clearly related to presence of crosslinking in the PVC foam. Increasing the degree of crosslinking restrains chain motion, strengthening the polymer, but also making it more brittle (11).

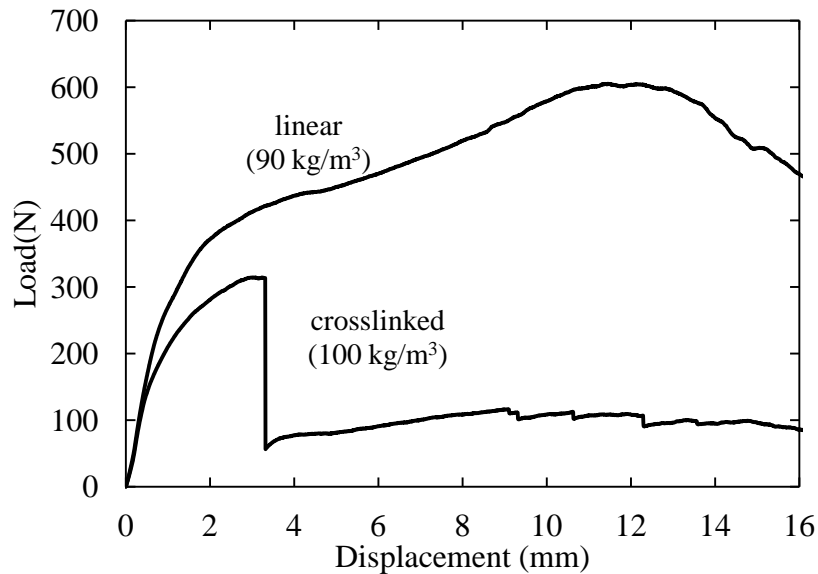
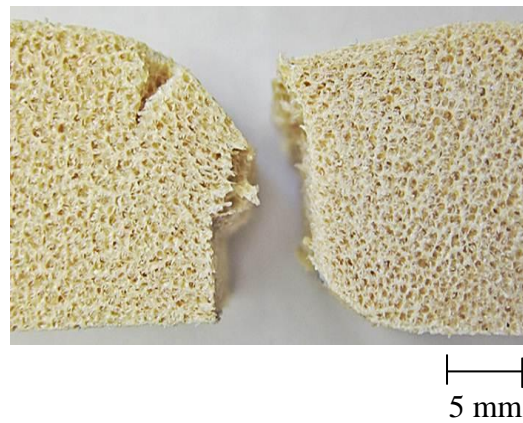
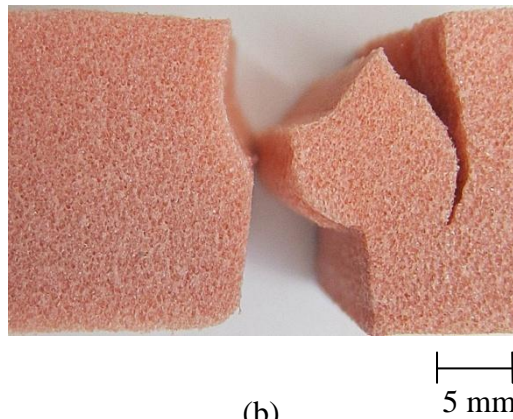


**Figure 4.26** Typical load-displacement traces following Mode II tests on the crosslinked PVC C70.90 and the linear PVC R63.80 foams

**Figure 4.27(a)** shows the failure modes on both the compression and tension sides in the linear R 63.80 foam. Just prior to failure, the cells were extended on the tension side (bottom) and compacted on the top (compression) side of the foam. Crack propagation was noted close to the notch. **Figure 4.27(b)** shows a side view of the crosslinked PVC C70.90 foam. It was observed that during Mode II testing, the crack propagated in a region between the clamping fixtures. The crack propagated across the width of the specimen at an angle of approximately  $45^\circ$ , propagating towards the moving traverse. This helps to explain the absence of a peak and the rapid drop in force in the load-displacement curve during testing. In a recent study (12), it was found that the higher values of the shear fracture toughness of linear PVC foams is due to the cell structure forming a sub-interphase zone during the manufacturing process. This phase delays crack propagation and increases the amount of deformation in the plastic region.



(a)



(b)

**Figure 4.27** Side views of (a) the linear PVC R63.80 and (b) the crosslinked PVC C70.90 foams following Mode II testing

#### 4.5 Relationship between the Mode I and Mode II Toughness

**Figure 4.28** presents a plot of the Mode II work of fracture against foam density for the crosslinked PVC, the linear PVC and the PET foams. As can be seen, there is roughly a linear relationship between the shear toughness and density for the five crosslinked PVC foams. Perhaps surprisingly, the toughness values for the linear PVC foams are similar to those of its crosslinked counterpart, contradicting the observation following Mode I tests. The PET foams offer the lowest shear toughness values for a given density, however these values still remain impressive.

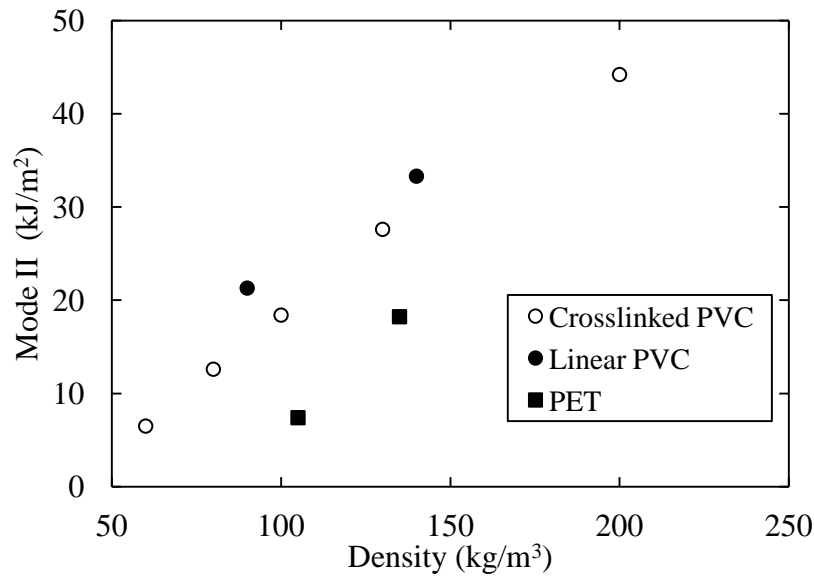


**Figure 4.28** Summary of the variation work of fracture (Mode II) with density for the crosslinked PVC, linear PVC and PET foams.

The relationship between the Mode I and Mode II fracture toughness values of the foams is presented in **Figure 4.29**. An examination of the data highlights the impressive shear fracture values relative to the Mode I data. This is most pronounced in the crosslinked PVC foams where the shear work of fracture values are approximately forty times greater than their corresponding Mode I values, suggesting the presence of significant plastic deformation during the failure process in the shear specimens. The shear fracture toughness enhancement was not as significant in the linear PVC and PET foams, however the Mode II values still remain impressive.

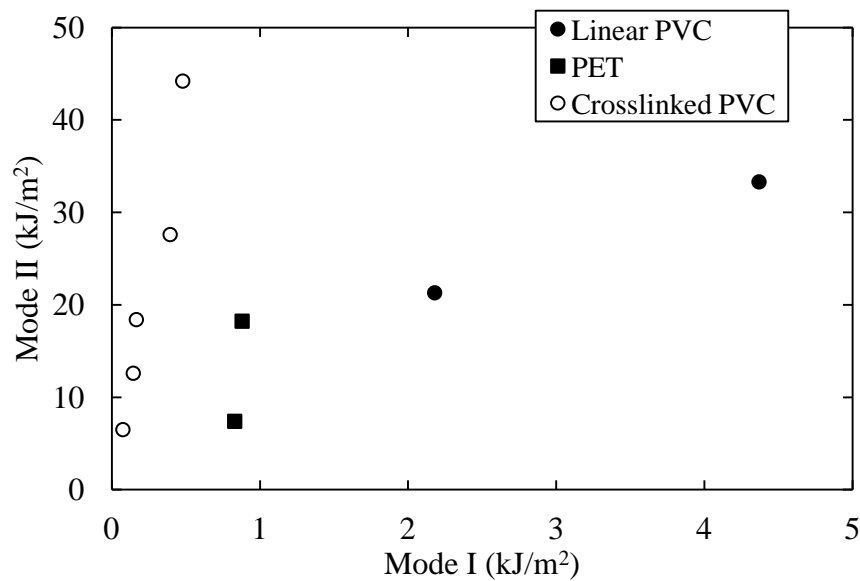


**Figure 4.29** Comparison of the Mode II work of fracture values of the foams with their corresponding Mode I values

#### 4.6 Conclusions

A series of mechanical test have been undertaken on a range of polymer foams in order to investigate how polymer type, foam density and loading rate influence the properties of these lightweight systems. Compression tests have shown that the plastic collapse strength is very sensitive to both foam density and strain-rate, tending to increase with an increase in both of these parameters. Furthermore, the strain-rate sensitivity has been shown to increase with foam density, an effect that has been observed by previous workers. Mode I fracture tests using the single edge notch bend specimen geometry have shown that the work of fracture increases with foam density and decreases with strain-rate. A simple geometry has been developed to measure the work of fracture properties of the foams under Mode II (shear) loading. As before, the work of fracture increased with foam density, with the PVC foams offering higher values than their PET counterparts. Here, the values of the work of fracture in shear were significantly higher than those in tension.



## 4.7 References

1. Maiti SK, Gibson LJ, Ashby MF. Deformation and energy absorption diagrams for cellular solids. *Acta Metallurgica*. 1984;32(11):1963-75.
2. Li QM, Magkiriadis I, Harrigan JJ. Compressive strain at the onset of densification of cellular solids. *Journal of Cellular Plastics*. 2006;42(5):371-92.
3. Brezny R, Green DJ. The effect of cell size on the mechanical behavior of cellular materials. *Acta Metallurgica et Materialia*. 1990;38(12):2517-26.
4. Tagarielli VL, Deshpande VS, Fleck NA. The high strain rate response of PVC foams and end-grain balsa wood. *Composites Part B: Engineering*. 2008;39(1):83-91.
5. Lim GT, Altstädt V, Ramsteiner F. Understanding the Compressive Behavior of Linear and Cross-linked Poly (vinyl chloride) Foams. *Journal of Cellular Plastics*. 2009;45(5):419-39.
6. Subhash G, Liu Q, Gao XL. Quasistatic and high strain rate uniaxial compressive response of polymeric structural foams. *International Journal of Impact Engineering*. 2006;32(7):1113-26.
7. Song B, Chen W, Frew DJ. Dynamic compressive response and failure behavior of an epoxy syntactic foam. *Journal of Composite Materials*. 2004;38(11):915-36.
8. Hazizan A. The impact response of composite sandwich structures (Ph.D Thesis): The University of Liverpool; 2002.
9. Kabir ME, Saha MC, Jeelani S. Tensile and fracture behavior of polymer foams. *Materials Science and Engineering: A*. 2006;429(1):225-35.

10. Marsavina L, Sadowski T, Kneć M, Negru R. Non-linear behaviour of foams under static and impact three point bending. *International Journal of Non-Linear Mechanics*. 2010;45(10):969-75.
11. Callister WD, Rethwisch DG. *Fundamentals of Materials Science and Engineering: An Integrated Approach*: Wiley; 2011.
12. Kanny K, Mahfuz H, Thomas T, Jeelani S. Static and dynamic characterization of polymer foams under shear loads. *Journal of Composite Materials*. 2004;38(8):629-39.

## **CHAPTER V**

### **LOW VELOCITY IMPACT ON SANDWICH STRUCTURES**

---

In this section of the thesis, the low velocity impact response of sandwich structures will be presented. Initially, indentations test under quasi-static and dynamic loading for sandwich structures with various densities of foam will be discussed. Following this, the results of perforation tests on the sandwich structures will be presented. Here, attention is given to evaluating and reviewing the failure mechanisms in the composites and core sandwich structures.

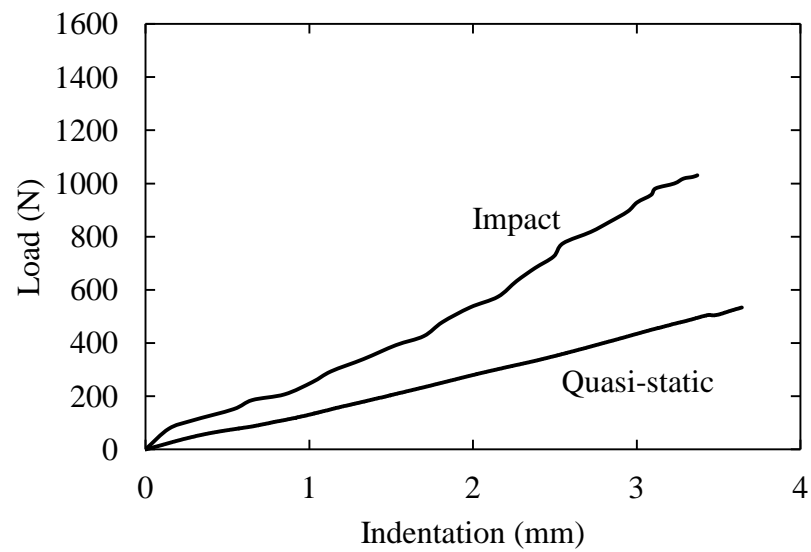
## 5.1 Indentation Testing

### 5.1.1 Quasi-static and Dynamic Indentation Tests on the Sandwich Structures

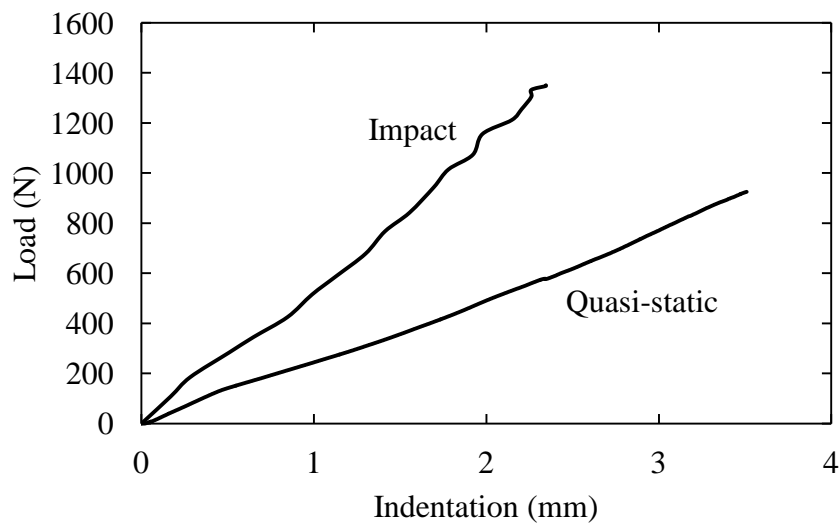
Indentation tests were conducted at quasi-static (1 mm/min) and dynamic (1.4 m/s) rates on sandwich structures based on six different types of polymer foam core and two types of composite skin. Initial tests were undertaken on sandwich structures based on 0.5 mm thick  $0^\circ/90^\circ$  woven glass fibre reinforced polyamide 6,6 (GFPA) skin with a nominal fraction of 0.55. The R63.80, C70.130, A500, WF 71, H 130 and HD 130 foams were used as a core material.

The quasi-static indentation tests were conducted on an Instron 4045 universal test machine at 1 mm/min, while low velocity impact tests were undertaken using an instrumented impact tower at impact velocity of 1.4 m/s. Both types of experiment were conducted using a steel indenter with a diameter of 10 mm. Further tests were conducted on sandwich structures with unidirectional GFRP skins and A500, H 130 and C70.130 foams.

**Figure 5.1** shows quasi-static and dynamic load-indentation curves for GFPA sandwich structures based on R63.80 and C70.130 foams. An examination of **Figure 5.1 (a)** and **(b)** indicates that all four load-indentation traces are relatively linear, suggesting that the indentation coefficient in the Meyer law is close to unity. **Figure 5.1** shows that the load-indentation plots obtained at dynamic rates are steeper than their quasi-static counterparts, suggesting a pronounced rate-sensitivity in the indentation response of the foams. This clearly agrees with the previously-discussed compression data, where significant rate sensitivity was apparent in **Figure 4.15**. Finally, a comparison of the load-indentation traces for the two types of PVC foam once again highlights the stiffer nature of the crosslinked system.



(a)



(b)

**Figure 5.1** Quasi-static and impact force-indentation curves for (a) the linear PVC foam R63.80 (b) the crosslinked PVC foam C70.130. The diameter of the indenter was 10 mm.

### 5.1.2 The Effect of Loading Rate on the Indentation Response of the Sandwich Structures

The indentation behavior of the sandwich structures was characterised using the Meyer indentation law, which states

$$P = C\alpha^n \quad [5.1]$$

where  $C$  is the contact stiffness and  $n$ , the indentation index, both of which are constants for a given system at a given temperature and loading rate. Equation [5.1] can be rewritten as:

$$\log P = \log C + n \log \alpha \quad [5.2]$$

The values of  $\log P$  and  $\log \alpha$  can be measured following quasi-static and dynamic indentation tests. **Figure 5.2** shows a plot of log force against log indentation showing the curve fitting method for determining the indentation constants  $n$  and  $C$  for the GFPA sandwich structure based on the C70.130 foam at a quasi-static rate of loading. The constants  $n$  and  $C$  were measured from the slope and intersection of the trace on the y-axis respectively. The average values of  $n$  and  $C$  following indentation tests on this sandwich structure are 1.1 and 282.9 N/mm<sup>1.1</sup>, respectively.

**Figure 5.3** summarises the values of the indentation coefficient,  $n$ , measured at both quasi-static and dynamic rates of strain. An examination of the data at 1 mm/min indicates that  $n$  lies between 0.96 and 1.11, coefficients that are clearly lower than the value of 1.5 predicted by Hertzian contact theory. **Figure 5.3** shows that when the strain rate is increased to that associated with impact loading, the value of  $n$  for the PMI WF 71 foam increases markedly, with the impact values being approximately 30 % greater than that measured at low strain rates.

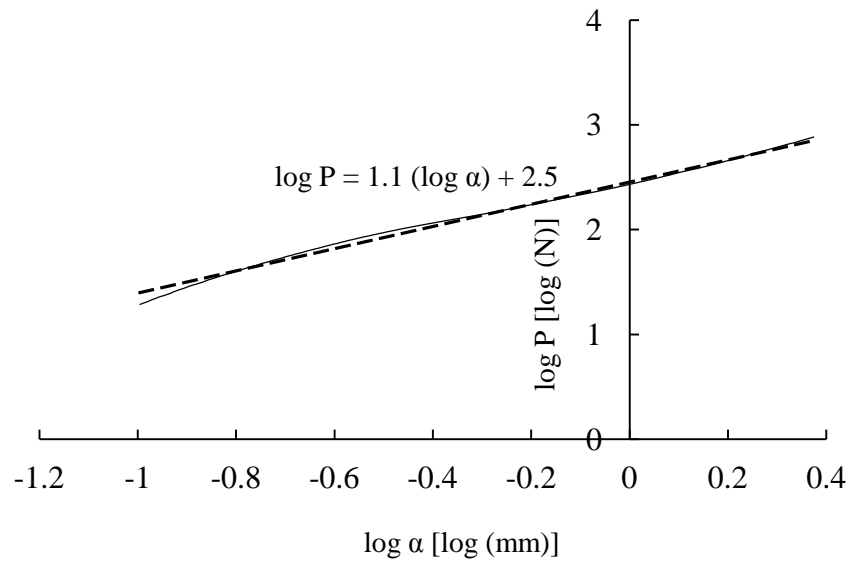


**Figure 5.2** A plot of  $\log P$  versus  $\log \alpha$  showing the curve-fitting method for calculating indentation constants  $n$  and  $C$  for the GFPA sandwich structure based on C70.130 foam. The test was undertaken at 1 mm/min.

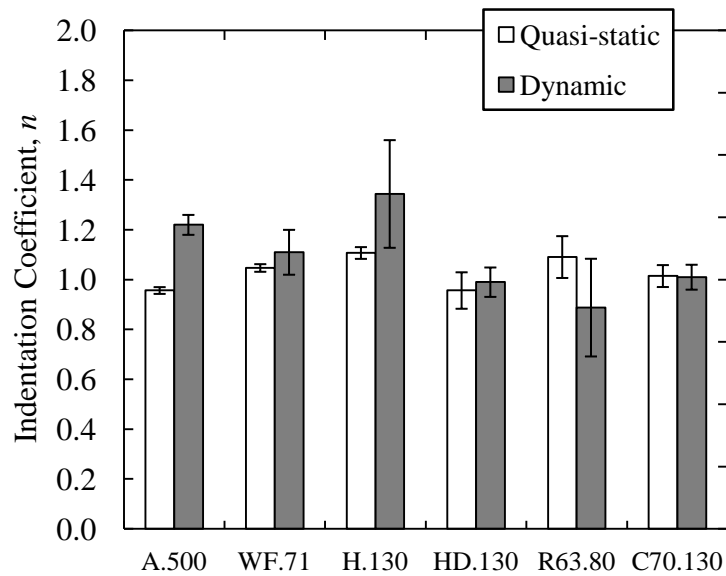


**Figure 5.3** Comparison of the quasi-static and dynamic values of the indentation exponent parameter ' $n$ '. The indenter diameter was 10 mm.

The evidence in **Figure 5.4** suggests that for most of the sandwich structures, the fundamental shape of the load-indentation trace remains unchanged as the strain rate is increased. This is a useful observation as it suggests that the quasi-static value of  $n$  can be used when modelling the dynamic indentation response of sandwich structures. **Figure 5.4** shows the corresponding values of the indentation constants,  $C$ , at the both quasi-static and dynamic rates of loading. Here, distinct strain-rate sensitive effects are in evidence, with the value of  $C$  increasing by up to 80 % in some systems. The A500 grade exhibits the lowest sensitivity to strain rate, whereas the C70.130 demonstrates the highest sensitivity. This evidence suggests that whereas the fundamental shape of the load-indentation trace does not change significantly with strain rate, its effective slope does.

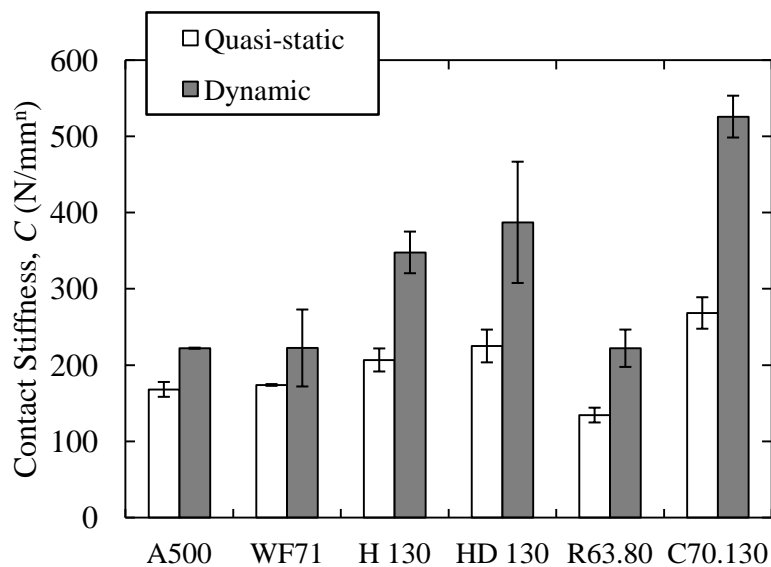


**Figure 5.4** Comparison of the quasi-static and dynamic values of the contact stiffness parameter ' $C$ '. The indenter diameter was 10 mm.

Loading a sandwich with a hemispherical steel indenter will result in locally high stresses within the core directly under the indenter. Localised loading of this nature is likely to trigger failure mechanisms similar to those observed during compression (e.g., plastic buckling and



the formation of plastic hinges within the foam), suggesting that the contact stiffness parameter,  $C$ , may depend on the compressive properties of the foam material. In order to investigate this, the quasi-static and dynamic values of  $C$  were plotted against the corresponding (i.e., quasi-static or dynamic) values of  $\sigma_{pl}$ .

**Figure 5.5** shows the resulting figure, which indicates that all of the data fall on what appears to be a single curve. This is an interesting observation, which suggests that the increase in  $C$  at dynamic rates of loading, reported in **Figure 5.5**, results from an increase in the value of  $\sigma_{pl}$ . It is worth reiterating that the data in this figure result from tests on four different types of foam (i.e., a SAN foam, a PMI foam, and two linear and two crosslinked PVC foams) with different densities, yet, the data appear to exhibit a unique dependency on  $\sigma_{pl}$ . The data in the figure clearly suggest a finite value of  $C$  when  $\sigma_{pl} = 0$ , an effect that reflects the contribution of the top surface composite skin in the indentation process.

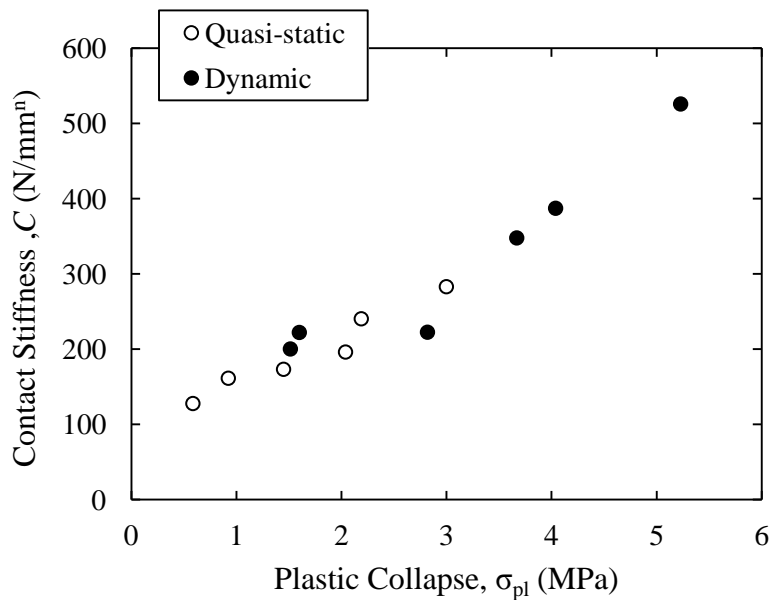


**Figure 5.5** The variation of the contact stiffness with the plastic yield stress for the quasi-static and impact tests.

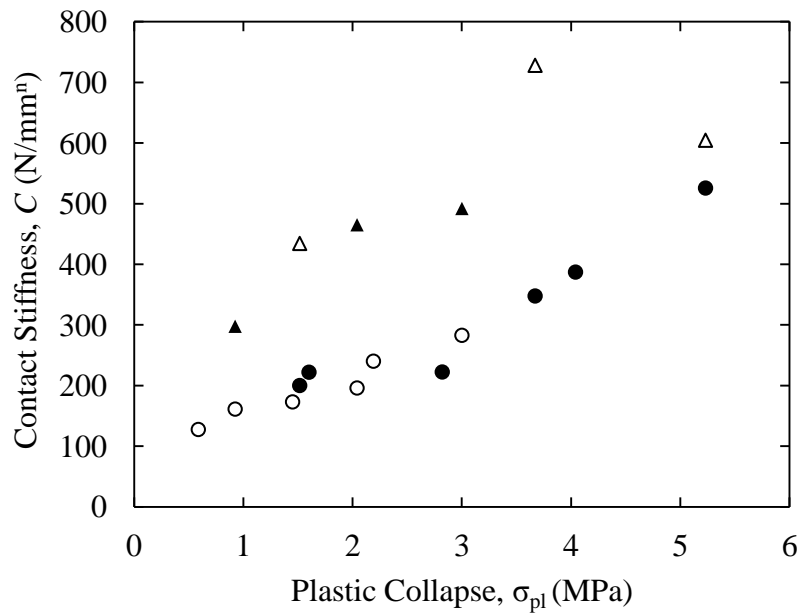


**Figure 5.6** The variation of 'C' with plastic collapse stress for the sandwich structures with foam cores (SAN A500, crosslinked H 130 and crosslinked C70.130) and glass fibre/epoxy skins. The tests were conducted at quasi-static (closed triangles) and dynamic (open triangles) rates of strain. The data from the tests on the glass/nylon sandwich structures (circles) are included for comparison.

This was investigated further by bonding GFRP skins to three of the foams, A500, H 130 and C70.130 and **Figure 5.6** shows the variation of  $C$  with  $\sigma_{pl}$ . It should be noted that the flexural rigidity of the GFRP skins was approximately eight times that of the GFPA composite. For comparison, the data presented in **Figure 5.6** are also included in this plot. From the figure, it is clear that increasing the flexural rigidity of the composite skins has effectively pushed the plot of  $C$  vs.  $\sigma_{pl}$  upwards.

### 5.1.3 The Effect of Indentor Diameter on Indentation Response of the Sandwich Structures

In order to investigate the effect of the indentor diameter on the indentation test of the sandwich structures, several quasi-static and impact tests were conducted by varying the diameter the hemispherical steel indentor. The dynamic indentation tests were undertaken using the indentors with diameters of 5, 10, 15 and 20 mm. **Figure 5.7** shows the variation of the indentation coefficient,  $n$ , for six foams, where it is evident that the value of  $n$  does not depend on the projectile diameter. The values of  $n$  are higher for the A500, WF 71 and R63.80 foams than for the three remaining systems.

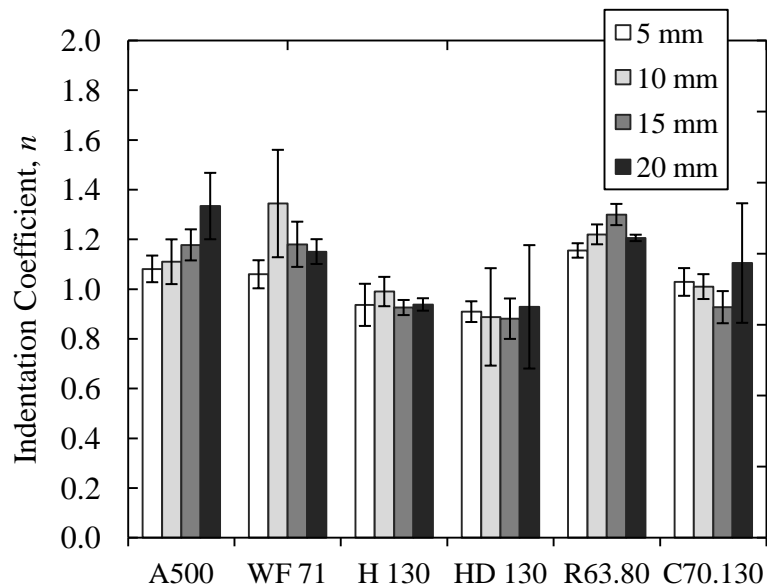


**Figure 5.7** Summary of indentation coefficient values as a function of indentor diameter for the six foams.

**Figure 5.8** summarises the influence of indentor diameter on the dynamic contact stiffness,  $C$ , for the six foams investigated in this study. An observation of the figure suggests that the value of  $C$  tends to increase with projectile diameter, although there does appear to be some scatter in the results, particularly between the 15 and 20 mm diameter projectiles. The figure

shows that the indenter diameter plays a more significant role as the stiffness of the core increases. For example, the value of  $C$  increases by approximately 25 % over the range of diameters for the low modulus R63.80 foam and by over 50 % for the stiffer C70.130 foam.

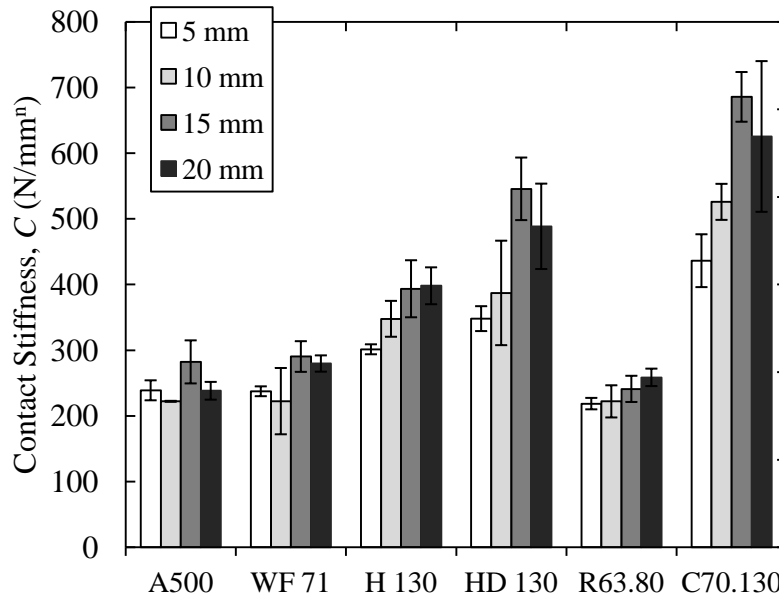


**Figure 5.8** Summary of contact stiffness values as a function of indenter diameter for sandwich structures based on the six foams.

Hertzian contact mechanics for indentation between two isotropic bodies suggests that:

$$P = C\alpha^{\frac{3}{2}} \quad [5.3]$$

where the contact stiffness  $C$  is given by:

$$C = \frac{4}{3}ER^{\frac{1}{2}} \quad [5.4]$$

This suggests that the contact stiffness is proportional to the square root of the indenter radius. **Figure 5.9** shows the variation of contact stiffness as a function of the square root of the indenter, from where it is evident that the data do exhibit a dependency on indenter geometry. It is interesting to note that for very small indenter diameters the data appear to extrapolate back to a value of contact stiffness  $C$  between 200 and 250 N/mm<sup>n</sup>. Indeed, the

data for the least stiff core materials, for example the R63.80 foam, are relatively flat with regard to indenter diameter, being close to what appears to be a limiting value of  $C$  for this set of sandwich structures. It is possible that the experimental data are tending towards a behaviour that is controlled by the mechanical properties of the skin material. Changing the facing material to a stiffer system, such as a carbon fibre reinforced plastic, is likely to change the effective slopes of the traces in this figure.

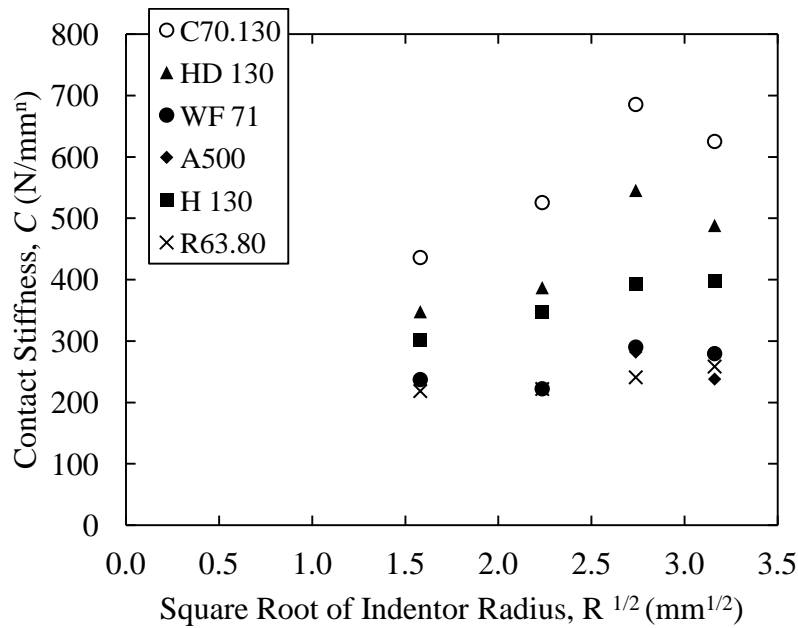


**Figure 5.9** *The variation of the contact stiffness with the square root of the indenter radius for six different sandwich structures.*

#### 5.1.4 The Effect of Skin Thickness on Indentation Behaviour

**Figure 5.10** summarises the influence of the thickness of the composite skins on the indentation response of the H 130, C70.130, and A500 sandwich structures at both quasi-static and impact rates of strain. The figure contains data for sandwich structures based on 2, 4, 8, 12, and 16 ply GFRP skins and also includes the previously-reported data for tests on the GFPA. It is evident that the indentation constant increases with the plastic collapse strength

of the foam for all of the systems examined here. It is also clear that the value of  $C$  increases as the thickness (flexural rigidity) of the skin material increases. The flexural rigidity is given by:

$$D = \frac{Eh^3}{12(1-\nu^2)} \quad [5.5]$$

where  $E$  is Young's Modulus of the skin,  $h$  is the skin thickness and  $\nu$  is the Poisson's ratio. It is interesting to note that increasing the laminate thickness from 0.6 to 4.8 mm (2 to 16 ply), that is, A500-fold increase in the flexural rigidity of the skin, typically resulted in a 300 to 400 % increase in the indentation constant.

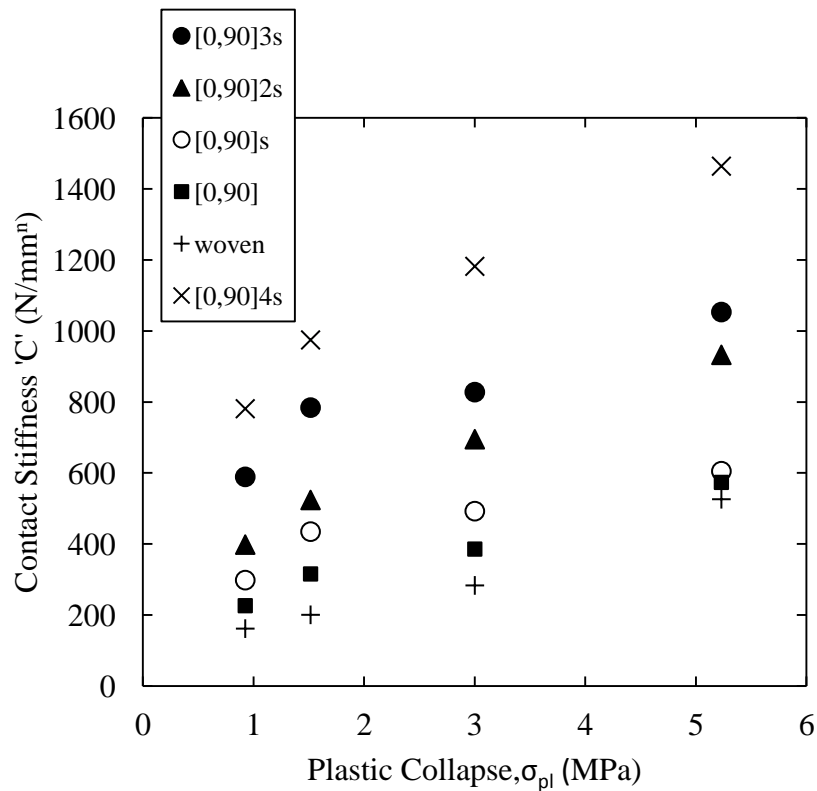


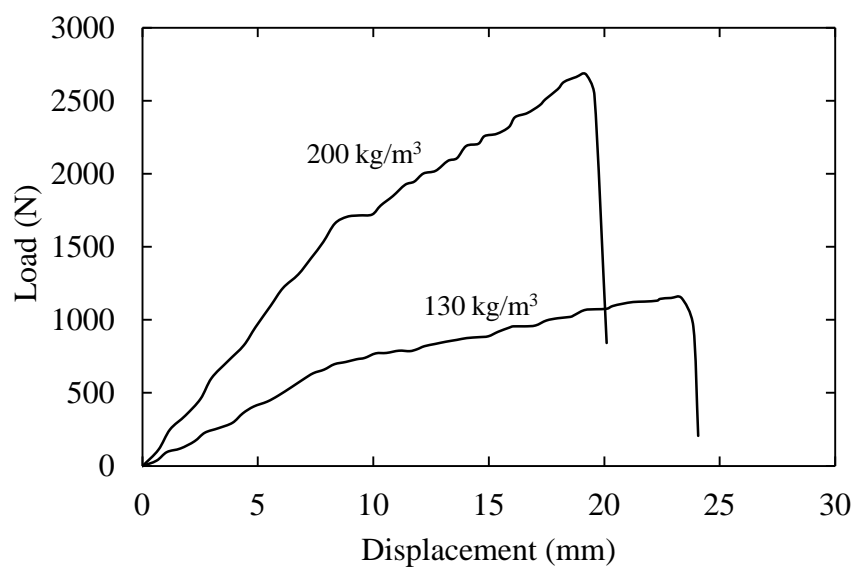
**Figure 5.10** The influence of skin thickness on the indentation constant of the C70.130 and A500 sandwich structures. The 0/90 laminates are based on GFRP skins and the woven laminate refers to the GFPA skin.

## 5.2 Perforation Resistance of the Sandwich Structures

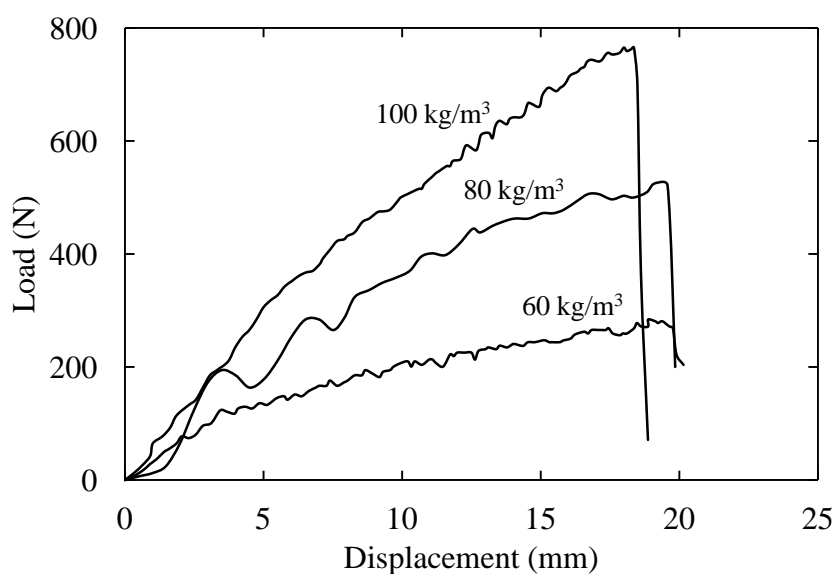
In this section, data are presented from perforation tests on the nine types of foam. Prior to conducting impact tests on the sandwich structures, a series of perforation tests were undertaken on the plain core materials. Foam panels with dimensions of 150 x 150 mm were clamped between the steel rings with an internal opening of diameter 100 mm. Impact tests were conducted using a 12.7 mm diameter hemispherical indenter. The mass used was 5.6 kg and it was released from the heights between 0.2 and 1.4 metres. The impact force and impactor displacement were measured using a piezoelectric load cell and a high-speed video camera. Furthermore, cross-sections of samples in these materials through the point of impact are presented to identify the failure modes.

### 5.2.1 Perforation Properties of the Plain Foams

Tests on plain foams were undertaken in order to establish the possible relationship between perforation resistance of a sandwich structure and that of its core material. **Figure 5.11** shows typical load-displacement traces following tests on the crosslinked PVC foams. Typically, all of the load-displacement traces exhibited an initial linear portion, associated with elastic deformation in the core, followed by a secondary, less steep region involving the passage of the projectile through the thickness of the foam core. This is most pronounced in the 200 kg/m<sup>3</sup> crosslinked PVC foam, where a distant knee is apparent at a displacement of approximately 9 mm. Loading continued until the load dropped suddenly and the target was perforated. Similar trends are observed in the load-displacement traces of the 135 kg/m<sup>3</sup> plain PET foam as shown in **Figure 5.13**.



(a)



(b)

**Figure 5.11** Typical load-displacement histories following drop-weight impact test on the plain crosslinked PVC foams.



Typical load-displacement curves following low velocity impact testing on the plain linear PVC foams are shown in **Figure 5.12**. From the figures, it is clear that all the traces exhibit a linear load-displacement trace until the peak force is reached. Beyond this point, a non-linear region is apparent. This region is associated with the majority of the energy absorption capacity of the foam. Following this, a pronounced load drop is observed.

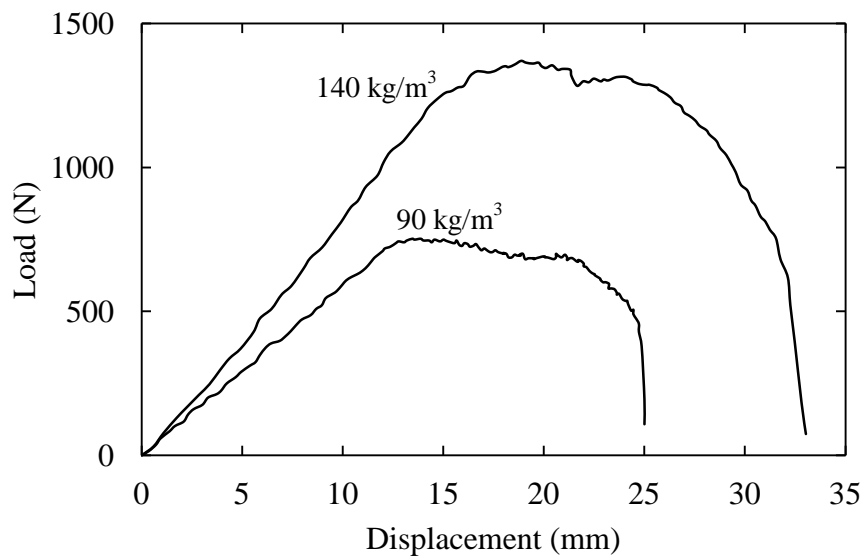


**Figure 5.12** Typical load-displacement histories following drop-weight impact test on the plain linear PVC foams.

**Figure 5.13** shows typical load-displacement traces following low velocity impact tests on the PET foams. From this figure, for the 105 kg/m<sup>3</sup> PET foam, it is clear that the curve initially exhibits an elastic response up to approximately 7 mm. After this point, a steep drop in load is observed associated with penetration of the foam. Following this, a constant load is apparent before a final sharp drop.

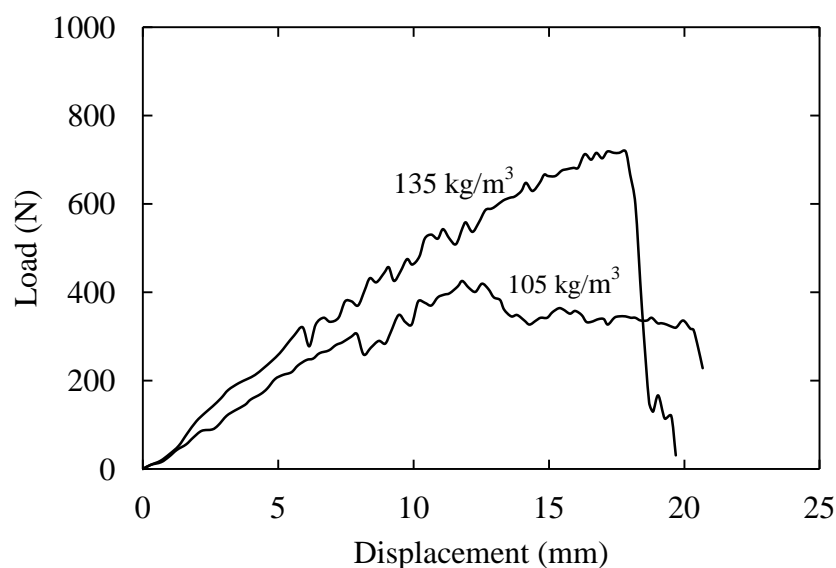


**Figure 5.13** Typical load-displacement curves following drop-weight impact tests on the PET foams.

**Figure 5.14(a)** shows cross-sections of plain foam panels following drop-weight impact testing. The pictures were taken through the perforated region in each sample. The passage of the projectile through the 60 and 80 kg/m<sup>3</sup> crosslinked PVC foams results in cylindrical-shaped hole, with the diameter being similar to that of the projectile. A change in failure mode was observed in the higher density crosslinked foams, where a conical-shaped perforation zone was apparent in the lower half of the specimen. Here, it is believed that the initial cylindrical region is associated with shearing of the core, whereas the conical region includes a tensile component. **Figure 5.14(b)** shows typical cross-sections of the linear PVC structures following perforation by the hemispherical projectile. The linear PVC foams exhibit relatively well-defined cylindrically-shaped perforation zones, suggesting that the foam fails predominantly in a shear mode. In contrast, the PET foam fails in the mixed-mode of failure.

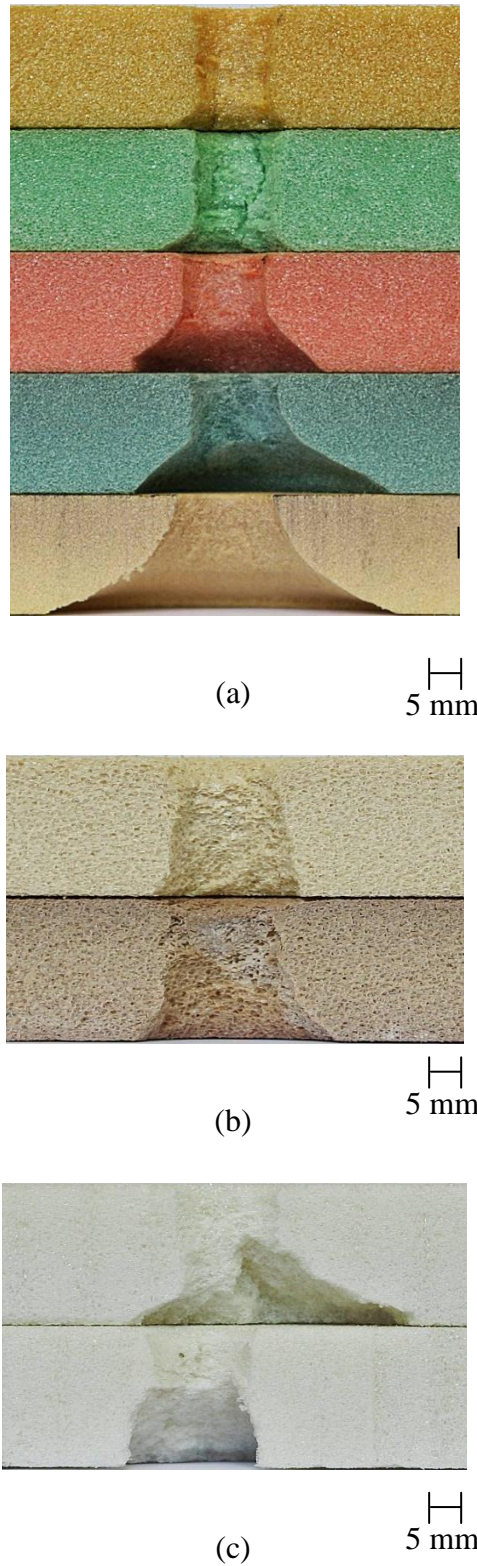


**Figure 5.14** Cross-sections of the perforated, (a) from top to bottom crosslinked PVC (C70.55), (C70.75), (C70.90), (C70.130), (C70.200) and (b) linear PVC (R63.80), (R63.140) (c) PET (T92.100), (T92.130) foams.

A summary of the perforation energy versus foam density of the nine foams is shown in **Figure 5.15**. As expected, increasing the density of a given foam type results in an increase in the perforation resistance. For example, an increase in the density of the crosslinked PVC foam from 60 to 200 kg/m<sup>3</sup> results in a 700 % increase in the perforation resistance of the foam. Rather surprisingly, the crosslinked PVC foams out-performed their more ductile linear PVC foams counterparts. The two PET foams offer lower impact resistances for a given density, although the rate of increase is similar to that observed in the crosslinked foams. The figure clearly shows that the foam density, on its own, does not determine the absolute perforation resistance of the sandwich.

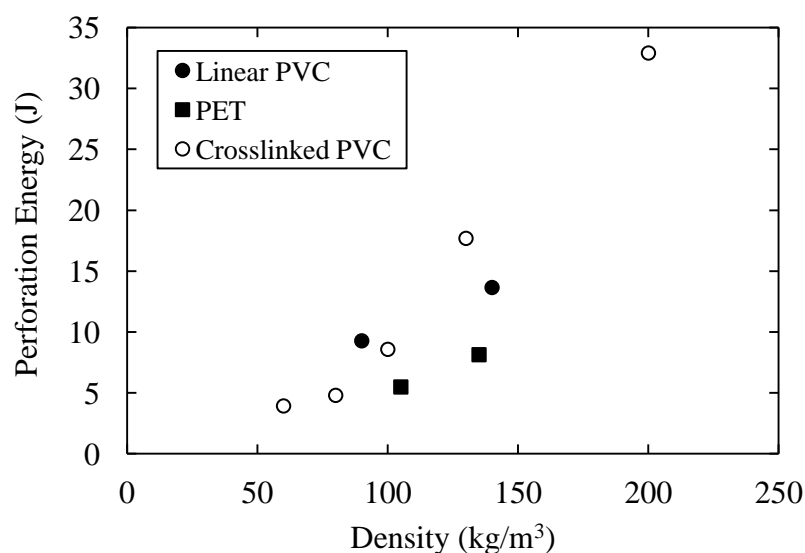


**Figure 5.15** Summary of the perforation energy of the plain cores as a function of core density.

As mentioned above, as the density increases, the core material within the sandwich structure plays an increasingly important role in the overall perforation process. This is clearly evident in **Figure 5.16**, where the average perforation force increases from approximately 200 N in

the 60 kg/m<sup>3</sup> system to over 1681 N in the highest density foam. It is likely that this value will be dependent on the shear strength of the core. In order to investigate this further, the average force during the core perforation process was measured and this is plotted against the average shear strength measured during the Mode II shear tests on the plain foam, **Figure 5.16**. An examination, the figure indicates that there is reasonable agreement between the average perforation force and the shear strength of the foam. The average perforation force of the linear PVC foams is higher than its crosslinked PVC foam counterparts due to the fact that shear dominated the fracture process in this foam. The PET foams lies below the remaining data, probably as a result of its low shear strength and the mixed-mode of failure, as shown in **Figure 5.14(c)**.

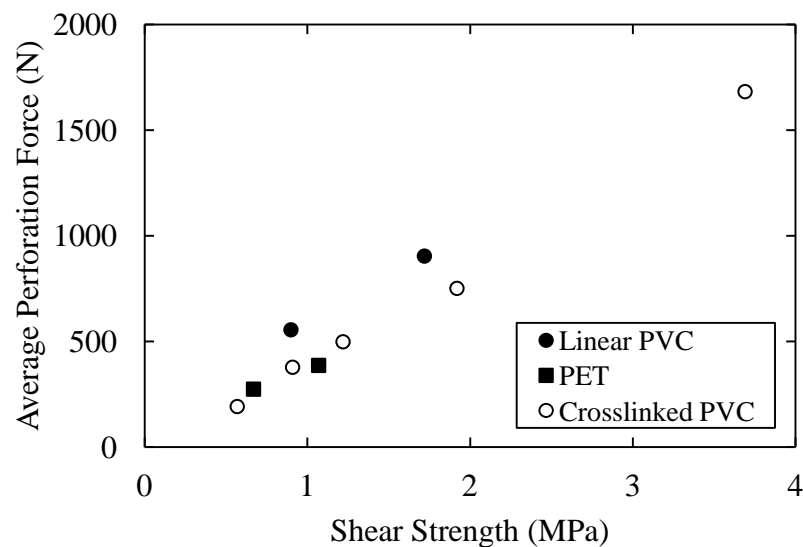


**Figure 5.16** Summary of the average perforation force of the plain core as a function of shear stress strength of the foam.

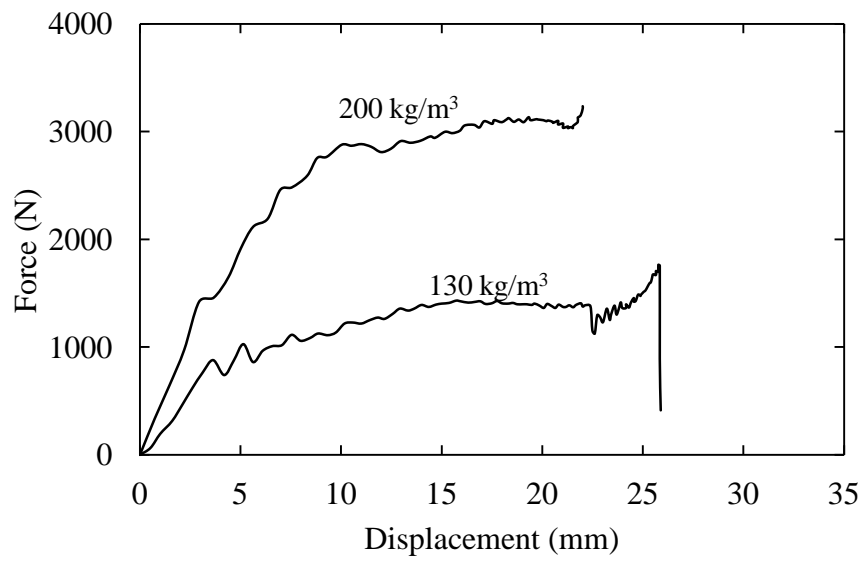
### 5.2.2 Impact Perforation of Sandwich Structures

In preparation for drop-weight impact testing, a series of sandwich structures were prepared by bonding composite skins to the foam core using a two part epoxy adhesive. The skins were based on a woven glass fibre reinforced epoxy. The majority of tests were conducted on panels with 0.25 mm thick skins and a number of tests were undertaken on structures with 0.5 mm thick facings. As before, sandwich structures with dimensions 150 x 150 mm were clamped between two steel rings and impacted centrally by a carriage with a 12.7 mm diameter hemispherical head. The force during the test was recorded using a piezoelectric load cell and the displacement using a high speed video camera. A simple model was used to predict the maximum impact force for subsequent comparison with the experimental results. The relationship between the mode of failure and the perforation resistance of the foam-based sandwich structures will be discussed.

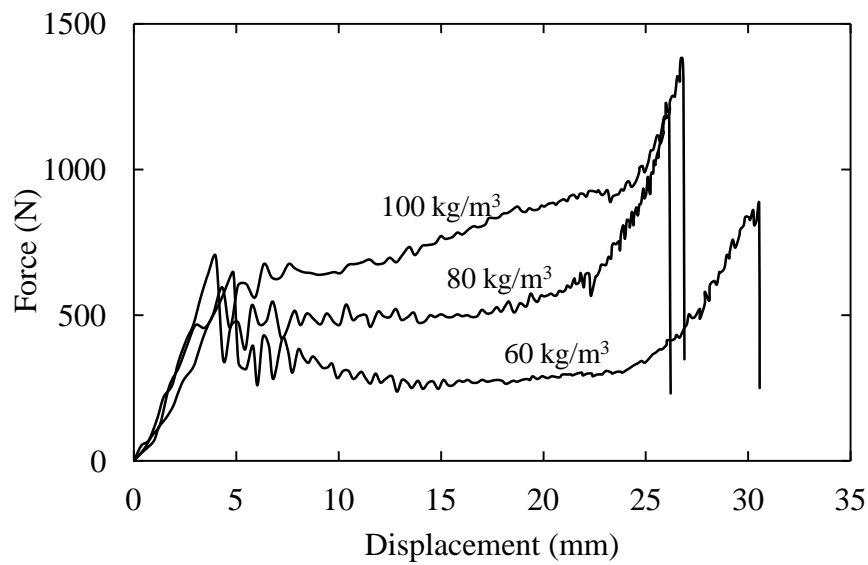
#### 5.2.2.1 Perforation Behaviour of the Sandwich Structures

**Figure 5.17** shows typical load-displacement plots following impact tests on sandwich structures based on the crosslinked PVC foams. The responses of the 60, 80 and 100 kg/m<sup>3</sup> structures are typical of that associated with drop-weight impact on sandwich structures as reported by Reid *et. al.* (1), where two distinct peaks in the load-displacement trace, associated with failure of the upper and lower skins, are in evidence. Similar responses can be observed from the sandwich structures based on PET foams, as shown in **Figure 5.18(b)**. Between these peaks there is a region where the force remains roughly constant, associated with the projectile perforating the foam core. The response during this phase of the impact process will clearly be dependent on the fracture properties of the core and this will be discussed further below. Increasing the core density to 130 kg/m<sup>3</sup> yields a response in which the core plays a more dominant role (**Figure 5.17 (a)**). The initial peak, resulting from

fracture of the top skin, remains in evidence. Following this, the force continues to rise as the projectile perforates the tougher core. The final peak in the trace is higher than that observed in the previous system and is again associated with failure of the lower composite skin. Finally, the load-displacement trace for the highest density system is almost entirely dominated by the response of the foam core. Here, failure of the top surface skin results in a small step in the initial portion of the trace. The force then increases rapidly, as the projectile perforates the core, before reaching a plateau value of approximately 3000 N (**Figure 5.17(a)**). Finally, a small increase in load is apparent as the projectile perforates the lower skin. It is interesting to note that the forces associated with failure of both the upper and lower skins increases as the density of the core increases, an effect that will be discussed in more detail below. Also, similar trends can be observed for the 140 kg/m<sup>3</sup> linear PVC foam sandwich structure, as shown in **Figure 5.18(a)**.



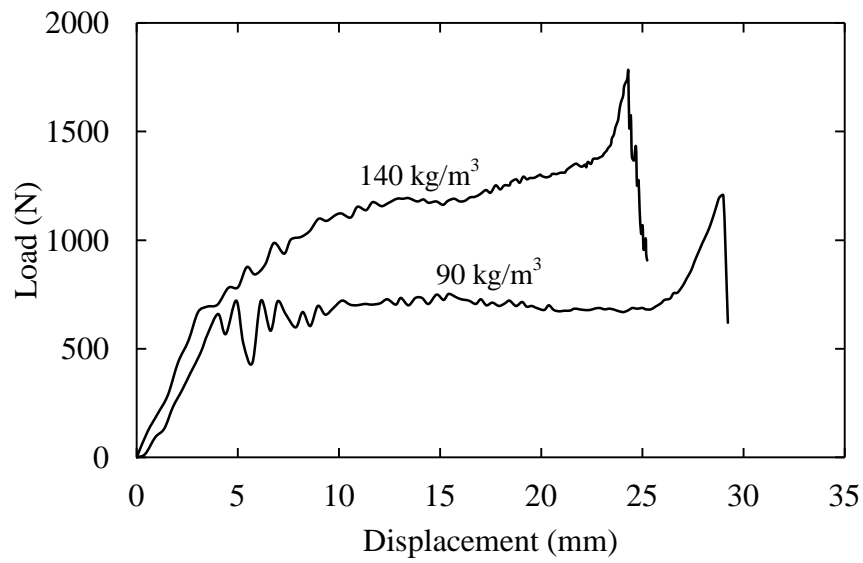
(a)



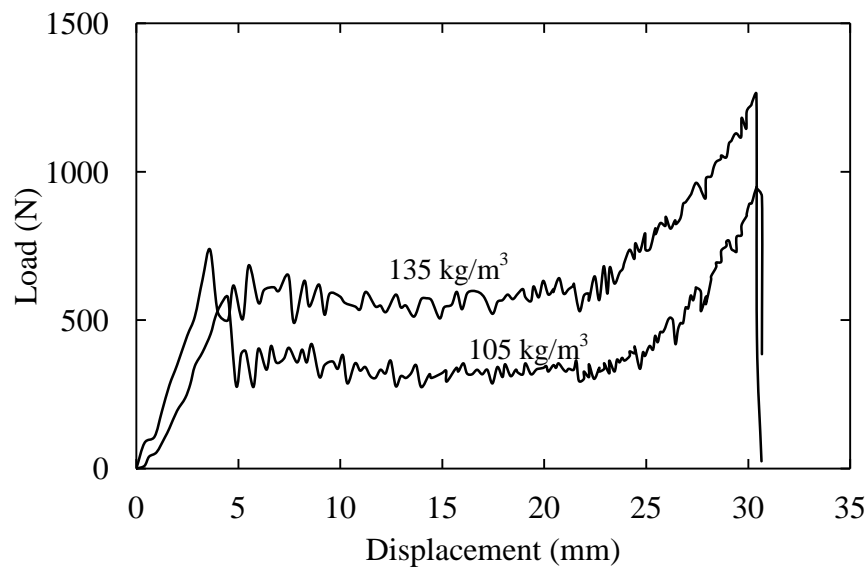
(b)

**Figure 5.17** Typical load displacement histories following drop-weight impact test on the sandwich structures based on crosslinked PVC (a) (C70.130) and (C70.200) (b) (C70.55), (C70.75) and (C70.90) foams.





(a)



(b)

**Figure 5.18** Typical load displacement histories following drop-weight impact test on the sandwich structures of (a) the linear PVC and (b) the PET foams.

**Figure 5.19** shows typical cross-sections of a number of the sandwich structures following perforation by the hemispherical projectile. The crosslinked PVC foams exhibit relatively well-defined cylindrically-shaped perforation zones of similar size to the impactor, suggesting that the foam fails predominantly in a shear mode. The perforation zone in the highest density crosslinked PVC foam also exhibits a clear shear zone, although the presence of a small conical-shaped crack is in evidence at the exit surface. It is likely that this cone-shaped cracked occurred as a result of locally-high tensile stresses close to the rear surface of the target (2). An examination of the linear PVC foam, **Figure 5.19(d)**, highlights the presence of a foam plug close to the rear surface of the sandwich structure. Closer examination of the cross-section indicates that the foam in this plug had been compressed by the projectile during the perforation process. **Figure 5.19(e)** shows the cross-section of the lowest density PET-based sandwich structure, where the presence of both a cylindrical shear zone and tensile cone crack is in evidence.

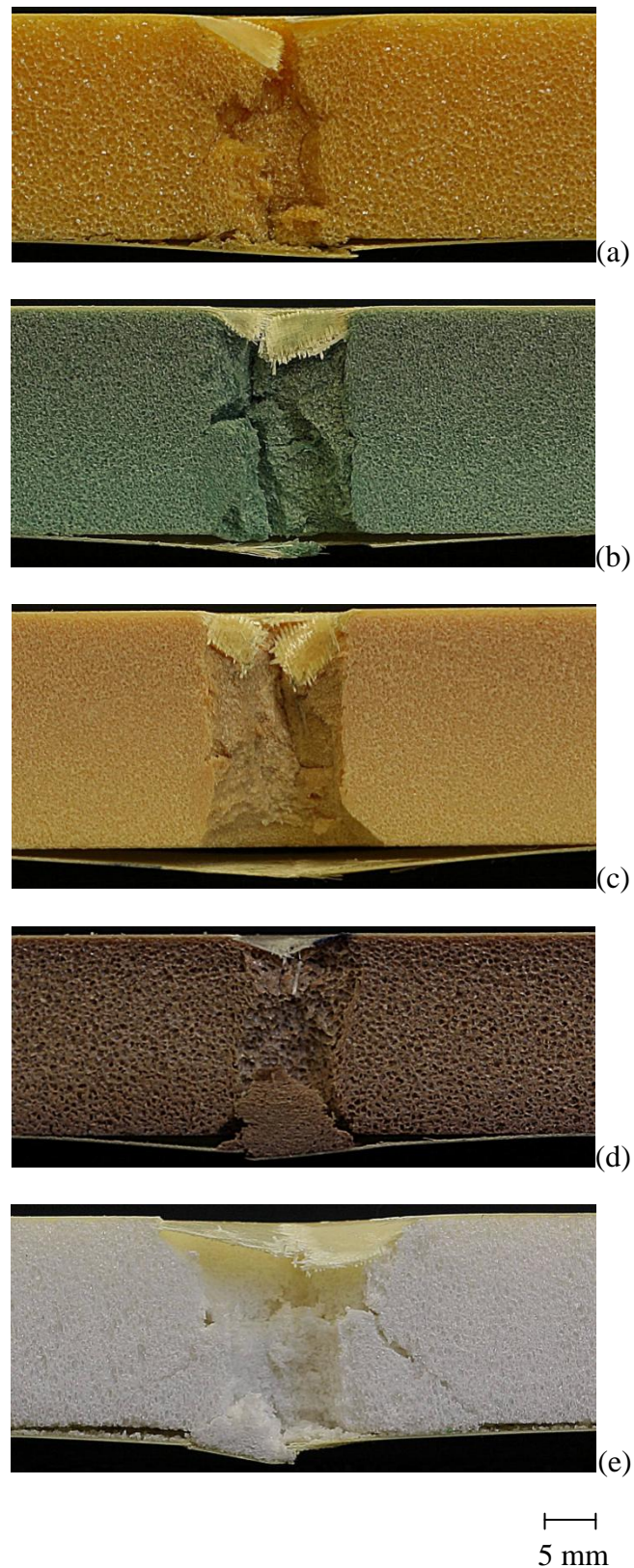


**Figure 5.19** Cross-sections of the perforated sandwich panels: (a) Crosslinked PVC (C70.55), (b) Crosslinked PVC (C70.130), (c) Crosslinked PVC (C70.200), (d) Linear PVC (R63.140), (e) PET (T92.100) foams.

The tensile failure model, developed by Fatt and Park (3) can be also used to predict the maximum impact force on a composite sandwich structures. A radial fracture pattern has been observed in carbon fibre skins subjected to impact by hemispherical-nose projectile (4) and this could be applied to the impact on the woven skin. The authors showed that the critical impact force for radial fracture in the composite skin of a sandwich structure is given by:

$$F_f = dA_{11}\varepsilon_{cr}(2\varepsilon_{cr})^{\frac{1}{2}} + K_c\pi R_e^2 q_d \quad [5.6]$$

where  $d$  is the length of damage,  $A_{11}$  is the laminate extension stiffness,  $\varepsilon_{cr}$  is the dynamic tensile fracture strain,  $K_c$  is a constraint factor for core crushing (set equal to 2.0 in the study by Hoo Fatt and Park (3)),  $q_d$  is the dynamic crushing strength of the foam and  $R_e$  is the effective radius of the projectile as defined in Ref. (3). The critical impact force for the radial fracture due to tensile failure is:

This equation suggests that the critical force for top skin failure should increase with the compressive strength of the polymer foam. Given that upper skin radial failure was observed in the sandwich structures tested here, the above equation was adopted in this study. The dynamic tensile fracture strain of this woven GFRP was taken as 1.5 %, the value of  $A_{11}$  was  $1.55 \times 10^7$  N/m, the value of  $d$  was assumed to be equal to the projectile diameter (i.e. 12.7 mm), the effective radius of the impactor was assumed to be equal to 0.7  $R$  where  $R$  is the true radius of the projectile and  $q_d$  was taken as the dynamic plastic collapse stress of the foam, as discussed in **Section 4.1.2**. **Figure 5.20** presents the average force associated with fracturing the upper skin as a function of the dynamic plastic collapse stress of the foam. The figure includes the force required to fracture the top skin peak of a core-less sandwich structure, prepared by removing a 100 mm diameter disc from the centre of a foam panel prior to bonding the composite skins. From the figure, it is clear that the measured peak force correlates reasonably well with the plastic collapse stress of the foam, highlighting the important role of the core in supporting the upper skin during the initial stages of the impact

event. The figure demonstrates that the Fatt and Park model predicts the trends in the experimental data quite successfully, highlighting the importance of the crushing properties of the foam in top surface damage initiation.

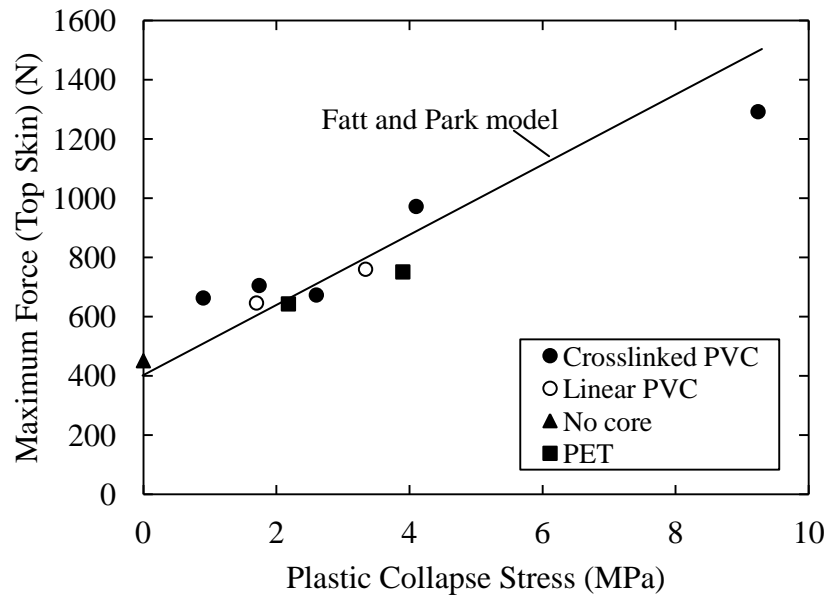


**Figure 5.20** *The variation of the force required to fracture the top skin as a function of dynamic plastic collapse stress of the foam core.*

Damage initiation in the sandwich panels was further investigated by placing the sandwich panels on a solid steel base and impacting the panels at energies above that required to initiate top surface skin failure. **Figure 5.21** shows the variation of the critical force for top skin failure as a function of the plastic collapse stress of the polymer foam. Interestingly, these values lie below those associated with impact on the clamped panels. Given that the fully-supported panels are stiffer than their clamped counterparts, one might intuitively expect the critical impact force in these structures to be equal to, or indeed greater than that measured on the plain clamped panels. Given the absence of any form of global flexural response in the fully-supported panels, it is possible that the effective projectile radius  $R_e$  featuring in Fatt

and Parks, model is lower. Applying their analysis to these new data points supports this conclusion, with a new (lower) value of  $R_e = 0.65R$  fitting the data reasonably well.

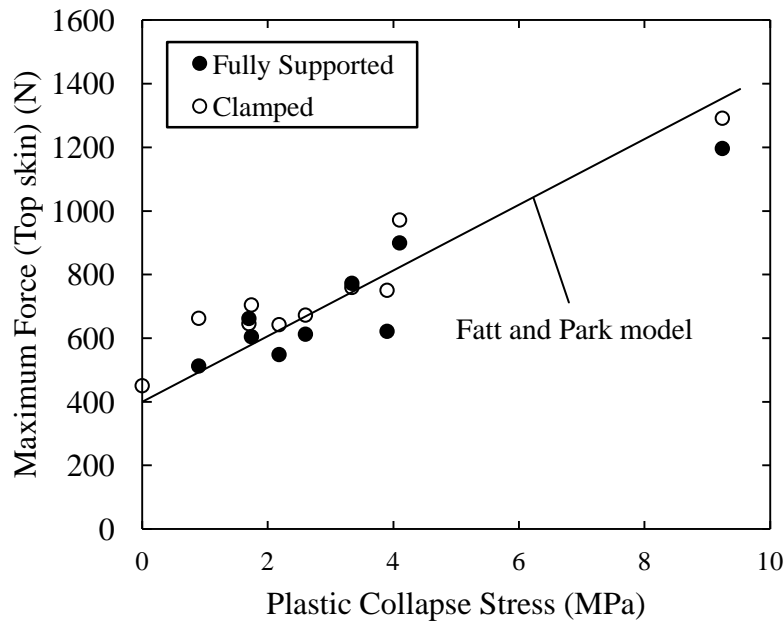


**Figure 5.21** The variation of the force required to fracture the top skin as a function of dynamic plastic collapse stress of the foam core for sandwich fully-supported on a steel base. The data from **Figure 5.20** are included for comparison.

### 5.2.2.2 Failure of the Core

As mentioned above, the core material plays an increasingly important role in the overall perforation process with increasing density. This is clearly evident in the load-displacement traces based on crosslinked PVC foams shown in **Figure 5.17**, where the average perforation force increases from approximately 400 N in the  $60 \text{ kg/m}^3$  system to over 2500 N in the highest density sandwich structure. The micrographs presented in **Figure 5.19** highlight the occurrence of significant core shear during the perforation process and such effects need to be

accounted for when modelling the perforation response of sandwich structures. Here, the average force required to perforate the core,  $P_c$ , was estimated using:

$$P_c = 2\pi Rh\tau \quad [5.7]$$

where  $R$  is the radius of the projectile,  $\tau$  is the shear strength of the foam, and  $h$  is the thickness of the foam core.

**Figure 5.22** presents a comparison of the experimental values of  $P_c$  with those predicted using the simple equation given above. Included in the figure are the four values associated with tests on the thicker, 0.5 mm thick GFRP skins. From the figure, it is clear that the simple model predicts the force required to perforate the foam core with reasonable accuracy. This is perhaps surprising given that quasi-static values of shear strength were used in this analysis. A closer inspection of the data indicates that the values associated with tests on the panels with thicker skins also follow the trends associated with the thinner skinned structures. This is to be expected, given that once the thicker skins have been fractured, the force required to perforate the core will be similar to that needed to shear the core in the thinner skinned structures. The greatest discrepancy occurs in the lowest density PET foam, where the simple model over-estimates the experimental value by approximately 50 %. However, an examination of the cross-section of such a sample highlighted a mixed-mode form of failure, with the upper section of the core failing in shear and the lower portion in a tensile cone crack, **Figure 5.19(e)**. Under such circumstances, equation [5.7] is not applicable.

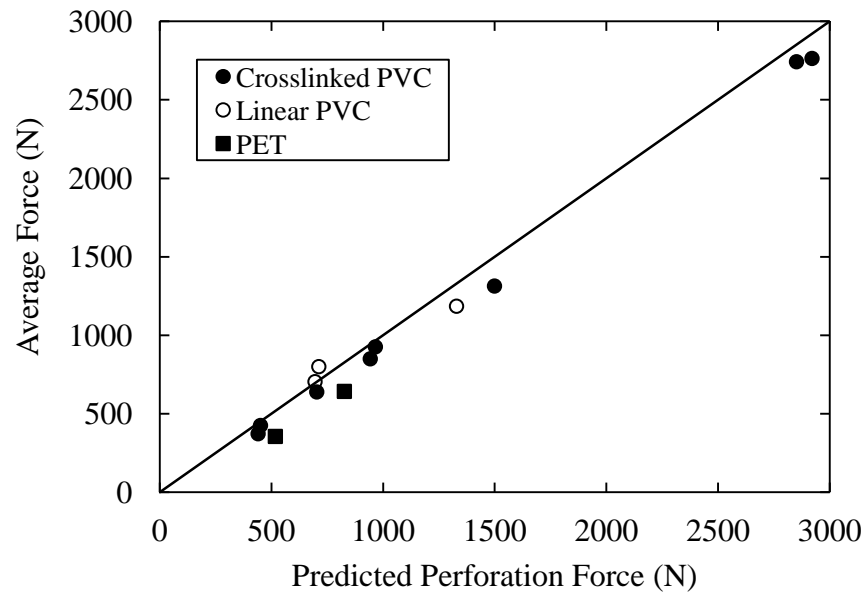


**Figure 5.22** Plot of the measured perforation force during core failure against the predicted value. The figure includes the data for the sandwich structures based on both 0.25 and 0.5 mm thick skins.

### 5.2.2.3 Failure of the Lower Skin

An examination of **Figure 5.23** indicates that the force associated with fracture of the rear surface skin increases significantly as the core density is increased. As can be seen from **Figure 5.23**, the average force associated with fracturing the lower skin in the lowest density crosslinked PVC core was 857 N, whereas that associated with the 200 kg/m<sup>3</sup> system was almost 3000 N. An inspection of the cross-section of the perforation zone of the linear PVC system, **Figure 5.19(d)** highlights the presence of a shear plug in which the foam has been heavily compressed during the impact event. This evidence indicates that the foam is compressed against the rearmost skin during the impact process. This suggests that the plastic collapse strength of the foam is likely to influence the maximum force achieved prior to fracture of the second composite layer. **Figure 5.23** shows a plot of the average force associated with fracture of the rear skin as a function of  $\sigma_{pl}$ . Once again, there is a reasonably



strong level of agreement between the crosslinked and the linear PVC systems. It is evident that, one of the PET foams lies away from the remaining data and this is likely to be a result of the mixed-mode (tension-shear) failure reported earlier.

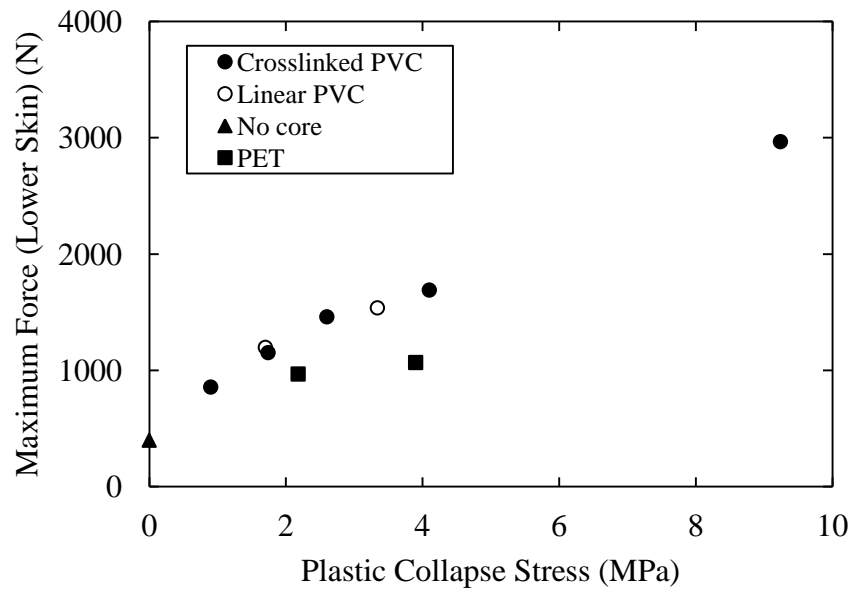


**Figure 5.23** *The variation of the force required to fracture the lower skin as a function of the plastic collapse stress of the foam core.*

#### **5.2.2.4 Perforation of the Sandwich Structures**

The energies absorbed in perforating the nine sandwich structures are summarised in **Table 5.1**. As expected, increasing the density of the foam, for a given type, results in an increase in the perforation resistance. For example, increasing the density of the crosslinked PVC foam from 60 to 200 kg/m<sup>3</sup> results in a 400 % increase in the perforation resistance of the associated sandwich structure. Rather surprisingly, the crosslinked PVC foams outperform their more ductile linear counterparts. For example, the perforation resistance of the crosslinked PVC 130 kg/m<sup>3</sup> foam is approximately 15 % higher than the 140 kg/m<sup>3</sup> linear PVC foam (**Figure 5.15**). Initially, this might appear surprising given that linear PVC foams are renowned for their intrinsic toughness and overall impact resistance. However, **Table 5.1** also indicates that the shear properties of the crosslinked foam exceed those of its linear counterpart.

Foam Type	Nominal Density (kg/m <sup>3</sup> )	Mode I Work of Fracture (kJ/m <sup>2</sup> )	Mode II Work of Fracture (kJ/m <sup>2</sup> )	Shear Strength (MPa)	Perforation energy of the sandwich structure (J)
CPVC (C70.55)	60	0.075	6.48	0.57	11.9
CPVC (C70.70)	80	0.15	12.6	0.91	15.3
CPVC (C70.90)	100	0.17	18.4	1.22	18.8
CPVC (C70.130)	130	0.4	27.6	1.94	28.3
CPVC (C70.200)	200	0.48	44.2	3.69	51.3
LPVC (R63.80)	90	2.18	21.2	0.9	19.8
LPVC (R63.140)	140	4.36	27.3	1.72	25.1
PET (T92.100)	105	0.83	7.38	0.67	10.2
PET (T92.130)	135	0.89	18.2	1.07	18.7

C = crosslinked, L = linear

**Table 5.1** *Summary of the fracture properties and perforation energies of the nine foams tested in this study.*

This was investigated further by plotting the perforation energies of the nine sandwich structures against the Mode II work of fracture properties of the associated core material, **Figure 5.24**. Included in the figure is the value corresponding to the tests on the coreless sandwich structure. Here, a unique relationship exists between the perforation resistance of the sandwich structure and the work of fracture properties under shear loading. Although not included in the figure (for purposes of clarity) the values for the panels based on 0.5 mm thick skins fall on a similar curve that is shifted vertically from that in the figure. The shift in the curve clearly reflects the added contribution of the thicker skin. The evidence in this figure suggests that the simple shear test presented above can be used to benchmark the perforation resistance of a foam for use in a sandwich structure.

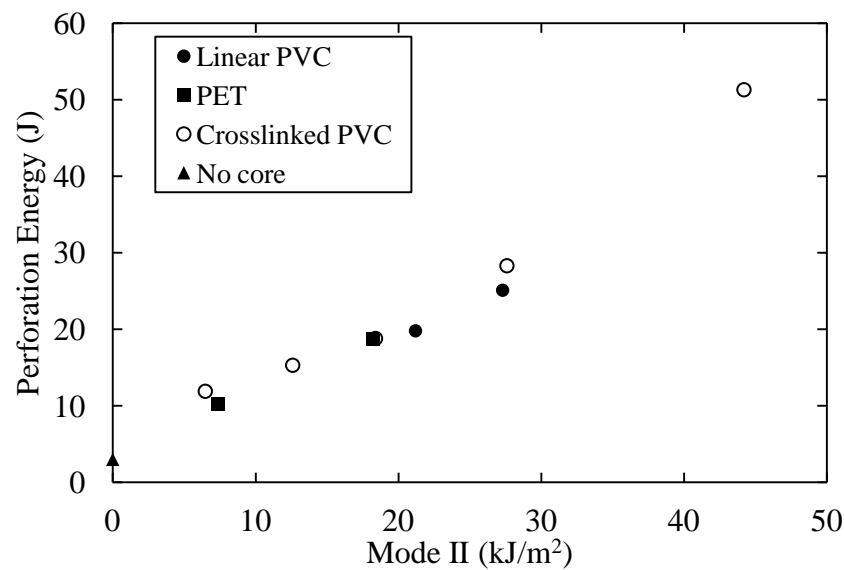


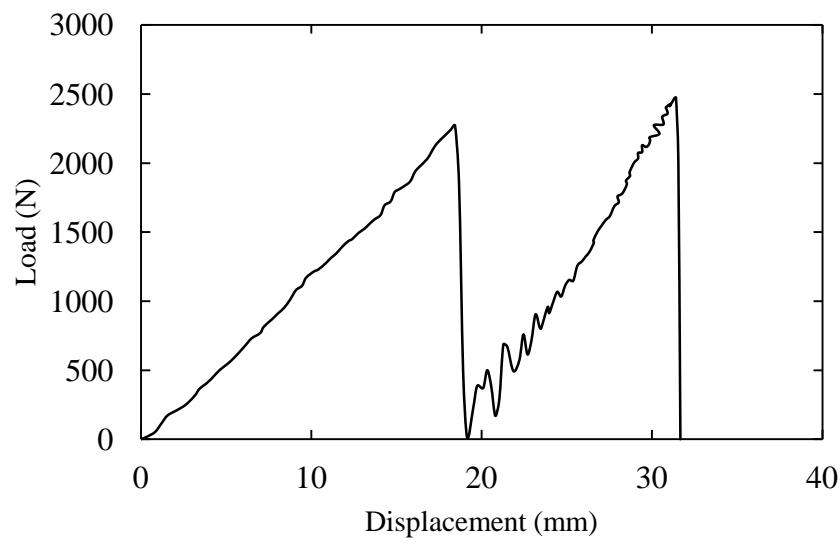
**Figure 5.24** *The variation of the perforation energy of the sandwich structure as a function of the Mode II (shear) work of fracture.*

### 5.3 Impact Response of the Fully Recyclable Sandwich Structures

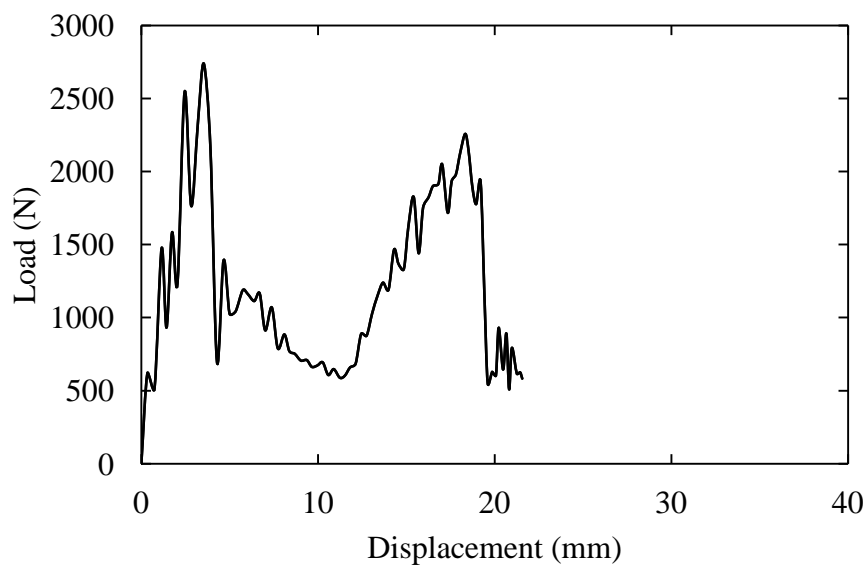
These sandwich structures were based on self-reinforced Polypropylene (SRPP) skins and Polypropylene honeycomb cores with densities of 40 and 80 kg/m<sup>3</sup>. A hot melt PP adhesive film (Xiro 23.601-40 from Collano) was used to join the skins to the core material. Here, the composite skins were fusion-bonded to the core at a temperature just above that required to melt the PP adhesive film. Two types of SRPP skin were used. The first was based on solid laminates of different thickness and the second was based on multiple thin layers (bonded using the hot melt adhesive), built up to give a skin thickness equivalent to the solid laminates. The second type of skin was evaluated in order to establish if there is any benefit to using multiple plies in place of a solid laminate. A limited number of tests were undertaken on a 10 mm thick aluminium honeycomb sandwich structures with GFRP skins.

The low velocity impact response of the sandwich structures was studied using the previously-mentioned falling-weight impact tower. Here, an impact rig with a 10 mm diameter hemispherical indenter was used for all tests. The impact energy was varied by increasing the drop-height of the impact carriage. The samples were clamped between two square supports with an inner edge length of 75 mm and impacted centrally. Load was measured using a piezoelectric load washer and displacement using a high speed video camera.

**Figure 5.25** shows typical load-displacement traces following impact tests on the SRPP-PP honeycomb sandwich structures and a GFRP/aluminium honeycomb structure. **Figure 5.25(a)** shows that the PP honeycomb exhibits two distinct peaks, each associated with fracturing one of the composite skins. The evidence suggests that more energy absorbing has been absorbed in fracturing the uppermost and lowermost skin. The aluminium honeycomb exhibits less defined peaks and the overall displacement is lower than that observed in the PP system.



(a)



(b)

**Figure 5.25** Load-displacement traces following impact on (a) the 0.66 mm multiple-layer SRPP-PP honeycomb sandwich structure and (b) the 0.6 mm GFRP/aluminium honeycomb structure.

**Figure 5.26** shows cross-sections of PP honeycomb and aluminium honeycomb samples subjected to differing energy levels. **Figure 5.26(a)** shows a PP honeycomb sample based on skins with two SRPP plies. Here, significant crushing is apparent in the core material under the point of impact. Damage in the core appears to extend some distance from the point of impact, suggesting that energy has been absorbed over a relatively large volume of core. **Figure 5.26(b)** shows the cross-section of a perforated PP honeycomb sandwich structure based on skins with three SRPP layers. A closer examination of the core material suggests that some of the incident energy has again been absorbed in plastically deforming the thermoplastic core material. **Figure 5.26(c)** illustrates the cross-section of a PP honeycomb structure based on a single 3.03 mm thick SRPP skin. Here, localised plastic-deformation in the top skin is apparent, as well as a fracture in the lowermost ply. Finally, **Figure 5.26(d)** presents the cross-section of a perforated aluminium honeycomb structure based on 0.6 mm thick GFRP skins. It is interesting to note that damage to the core is localised to the point of impact, suggesting that global energy absorption away from the point of impact does not occur in these samples.

**Figure 5.27** shows the variation of perforation energy of the PP honeycomb sandwich structures with skin thicknesses following low velocity impact tests. Included in the figure are the values associated with tests on the aluminium honeycomb. Clearly, there is a good degree of correlation between the perforation resistance of the sandwich structures and its skin thickness. Increasing the skin thickness increases the perforation resistance in a linear fashion. The effect of varying the core density on the perforation resistance of the sandwich panels is examined in **Figure 5.27**. It can be seen that the denser core offers a higher perforation resistance, increasing the density from 40 to 80 kg/m<sup>3</sup> serves to increase the perforation resistance by approximately 50 %. In addition, for the same skin thickness, the perforation energy for the honeycomb sandwich structure is similar to the PP sandwich structure (40 kg/m<sup>3</sup>).

Core buckling spreading outwards from  
the loading point



Extensive core buckling towards  
edge of panel

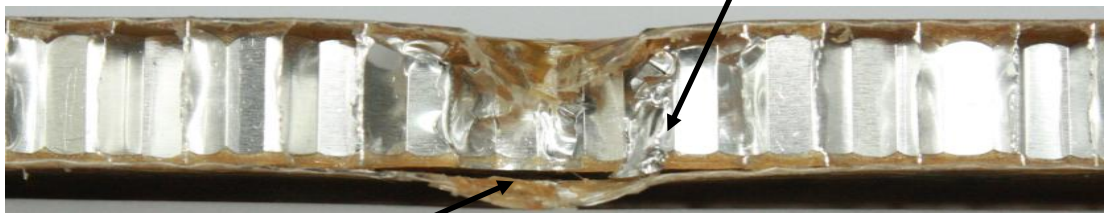
(a)



(b) Core crushing under the  
point of loading



(c) Core crushing in the area  
surrounding projectile



Delamination

(d)

5 mm

**Figure 5.26** Cross-section of the sandwich structures following impact (a) 0.66 mm multi-layers (b) 1.02 mm multi-layers (c) 3.03 mm monolithic SRPP skins-PP honeycomb sandwich structures (d) 0.6 mm GFRP/aluminium honeycomb structure.



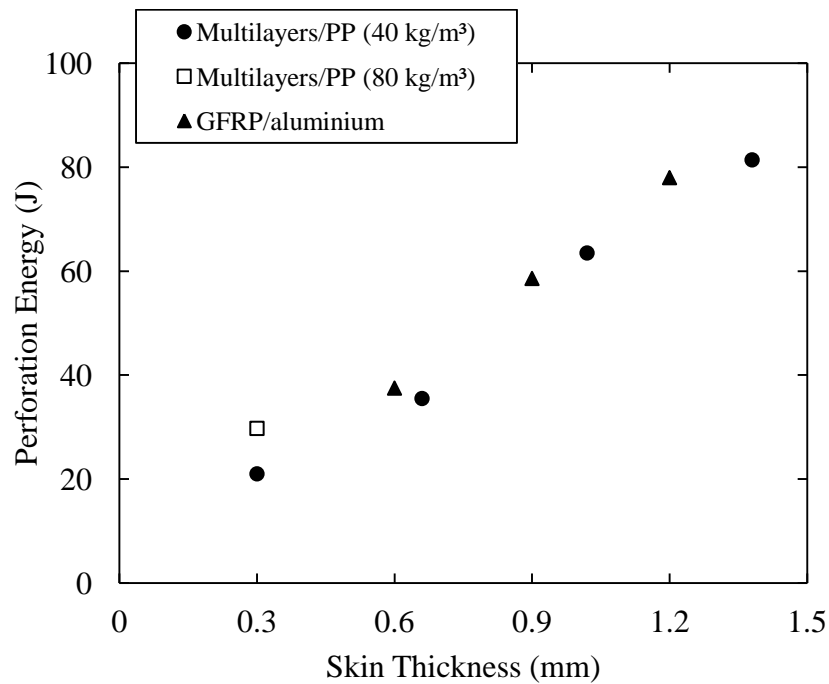


**Figure 5.27** The variation of perforation energy with skin thickness for PP sandwich structures based on multi-layer skins and cores of density 40 and 80 kg/m<sup>3</sup>. The figure includes the data point for the aluminium sandwich structure.

### 5.3.1 Skin Configuration and Thickness

**Figure 5.28** shows the variation of the perforation energy of the sandwich structures with thickness of the composite skins. The figure includes data for both the multi-layered skins and the monolithic skins. Clearly, an increase in skin thickness results in an increase in the perforation resistance of the sandwich panel. Zhou *et. al.* (5) reported that increasing the skin thickness significantly increases not only the peak load, but also the energy absorbed by a honeycomb sandwich structure. It is interesting to note that the impact resistance of the multi-layer sandwich structure is significantly higher than that of its monolithic counterparts (i.e. one single sheet of SRPP) suggesting that manufacturing skins based on many thin layers of composite bonded together leads to a vastly superior performance. It can be seen that for the same thickness of skin, 1.23 mm, the perforation resistance of the sandwich structure with

multi-layer skins is approximately 240 % greater than that of the monolithic skin. It is likely that the increased level of interfacial shear facilitated by the presence of the relatively low shear modulus PP interlayer enhances the energy-absorbing capacity of these materials.

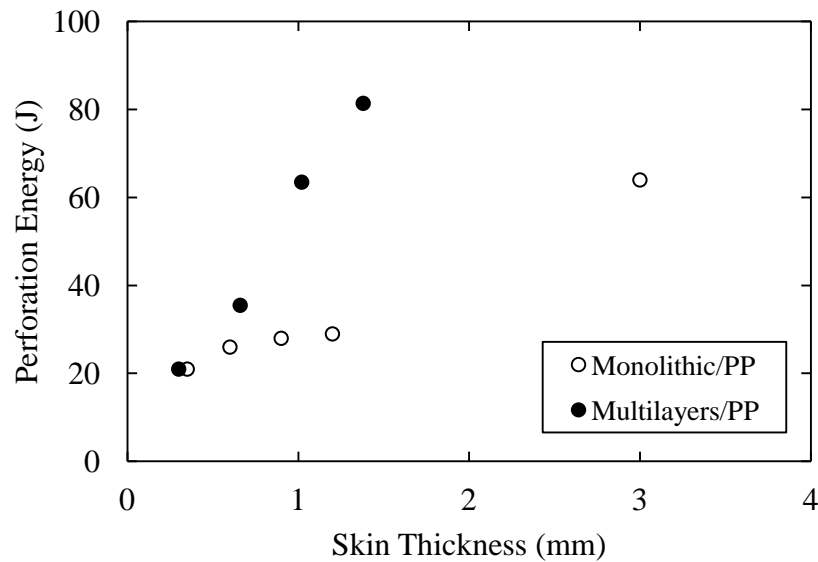
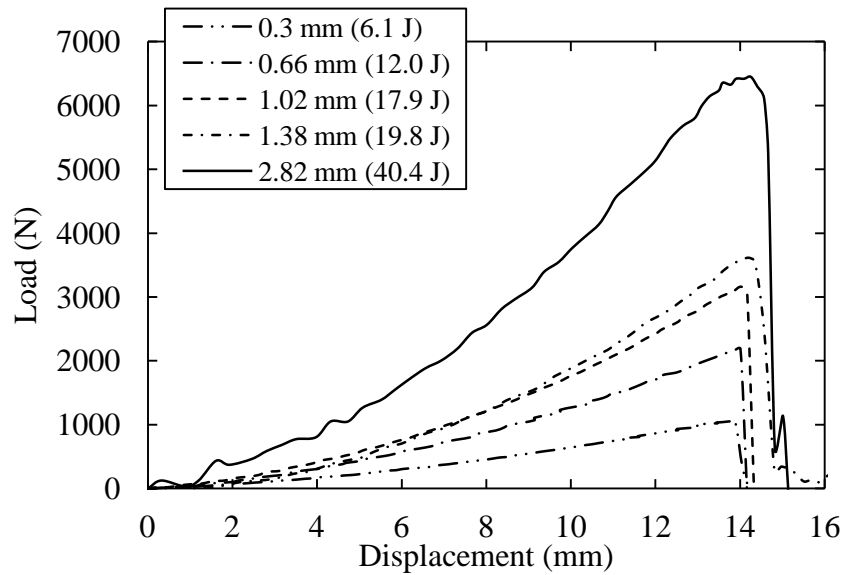


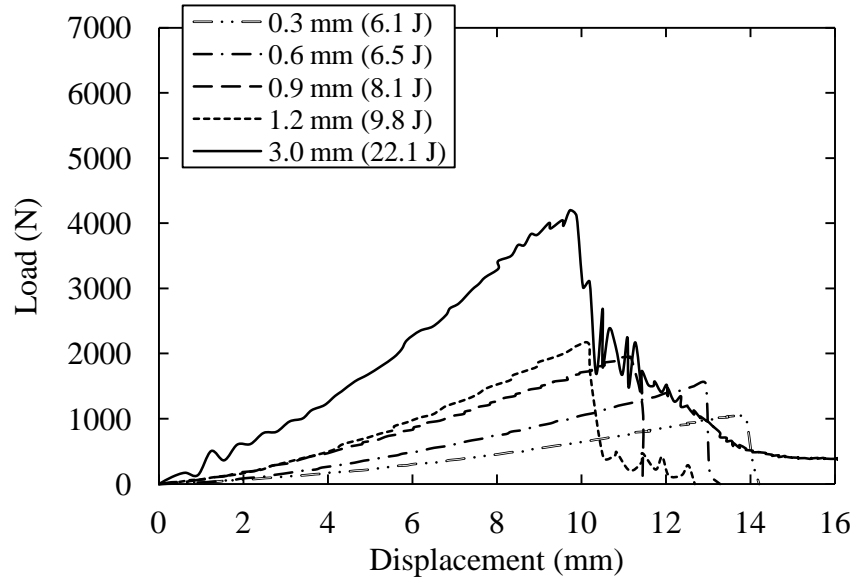
**Figure 5.28** The variation of perforation energy with skin thickness for sandwich structures based on both multi-layers and monolithic skins.

Increasing the skin thickness increases not only the perforation resistance of the sandwich structures but also the local contact stiffness. Nevertheless, varying the skin configuration has affected the perforation energy and the load transfer between the top skin and the core. This was investigated further by manufacturing and testing individual skins on their own, (i.e. not in a sandwich configuration). **Figure 5.29(a)** shows, load – displacement traces for five types of multi-layer SRPP skin and those as a single SRPP sheet. As shown in **Figure 5.29(a)**, the peak load increased with an increasing number of plies. It is interesting to note that, the maximum displacement for all types of skin configuration is very similar, **Figure 5.29(a)**. These impact tests were also performed on the monolithic skin materials. **Figure 5.29(b)**

shows that maximum load and displacement increases progressively with increasing skin thickness. The increased specimen deflection observed in the multilayer samples is again likely to be due to the greater level of interlaminar shear strain the PP interlayers.



(a)



(b)

**Figure 5.29** Typical load-displacement traces for panels based on (a) multi-layers and (b) monolithic skins.

**Figure 5.30** shows the effect of specimen thickness on the perforation resistance of laminates based on multi-layers and monolithic sheets. For the multi-layers, the perforation energy increased with increasing specimen thickness. For the monolithic laminates, there is clearly a non-linear relationship between specimen thickness and perforation energy. This trend is in agreement with that reported by Alcock *et. al.* (6) following perforation impact tests on a all-PP composite tape. **Figure 5.30** also highlights the advantages of using multi-layer materials. Here again, it was evident that the multi-layer systems outperformed than the single monolithic skin for a given thickness.

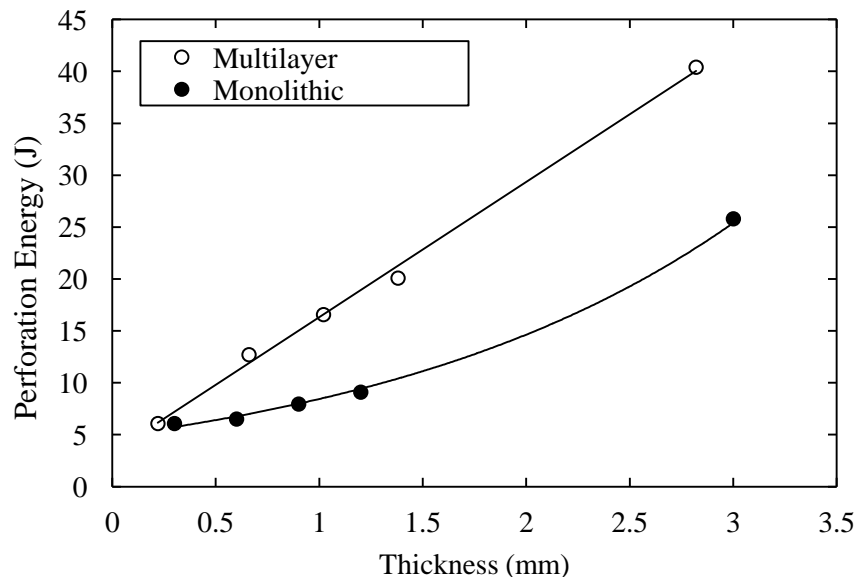


**Figure 5.30** The variation of perforation energy with composite thickness for panels based on multilayer and monolithic skins.

The shape of the damage zone in the perforated samples reflects the deformation mechanisms occurring within the panels. **Figure 5.31(a)** shows a characteristic cross-shaped penetration zone, formed by breaking and tearing the 0.9 mm monolithic skin. This typical mode of failure is in agreement with that reported by Aurrekoetxea *et. al.* (7). **Figure 5.31(b)** illustrates the perforation damage zone in 0.9 mm thick multiple skins-SRPP and shows the

large amount of fibre pull-out localised in projectile contact area. It has been suggested that the fibre pull-out mechanism absorbs the greatest amount of energy during the perforation process in multilayer skins. In contrast, fibre breakage which is a common mode of failure in solid laminate skins does not appear to be a significant energy-absorbing mechanism in these laminates.

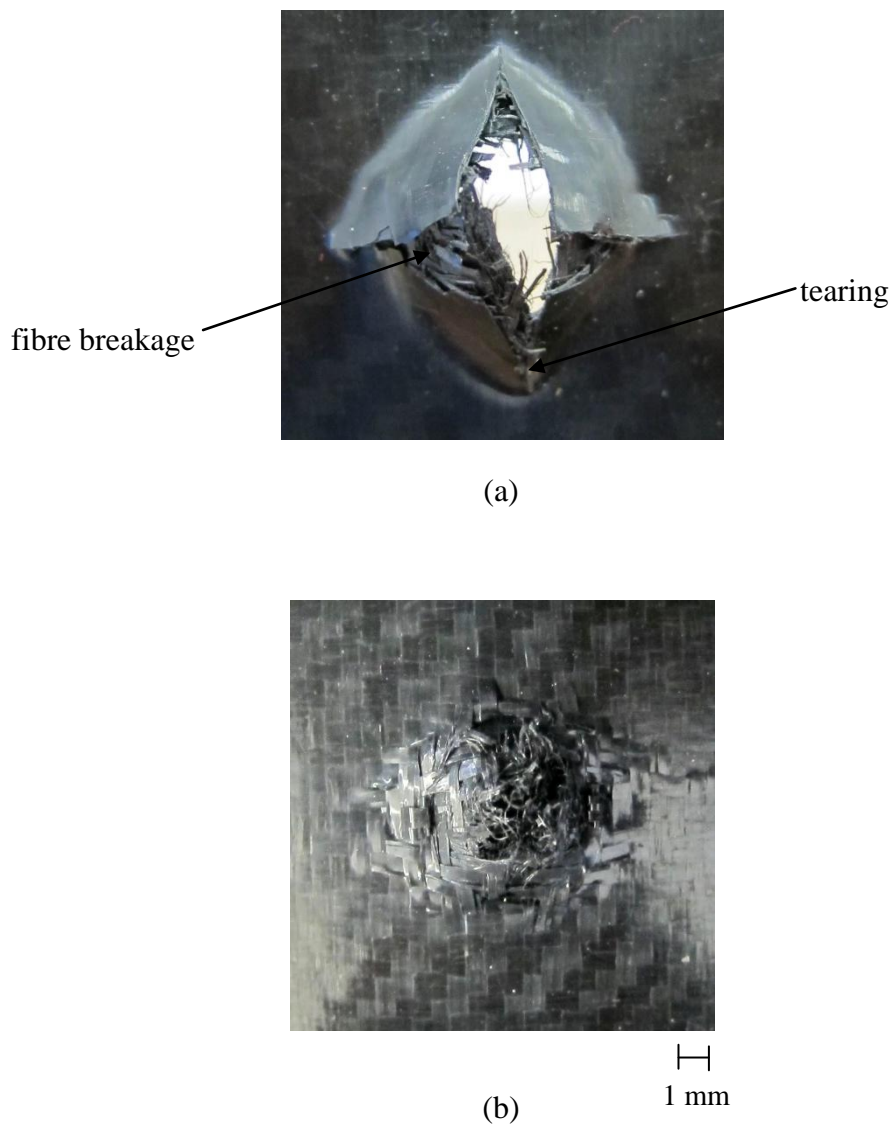


**Figure 5.31** Typical perforation zone in 0.9 mm thick (a) monolithic and (b) multilayer skins.

### 5.3.2 Effect of the Skin on the Impact Response of the Paperboard Core Sandwich Structures

**Figure 5.32** shows typical load-displacement plots for the paperboard sandwich structures based on 0.63 and 1.23 mm thick monolithic skins. Considering the load response during impact on the 0.63 mm skin structure, the force reaches a peak as the projectile fractures the uppermost skin. Following this, as the projectile reaches the weaker core material, the impact force drops to approximately 200 N. The load then rises again to a peak as the projectile contacts the back face, before finally reducing to zero as it fully perforates the sample. The load-displacement curve for the thicker sandwich structures is very similar, with two distinct peaks. However, the overall displacement is lower than that recorded in the 0.63 mm skin thickness system.

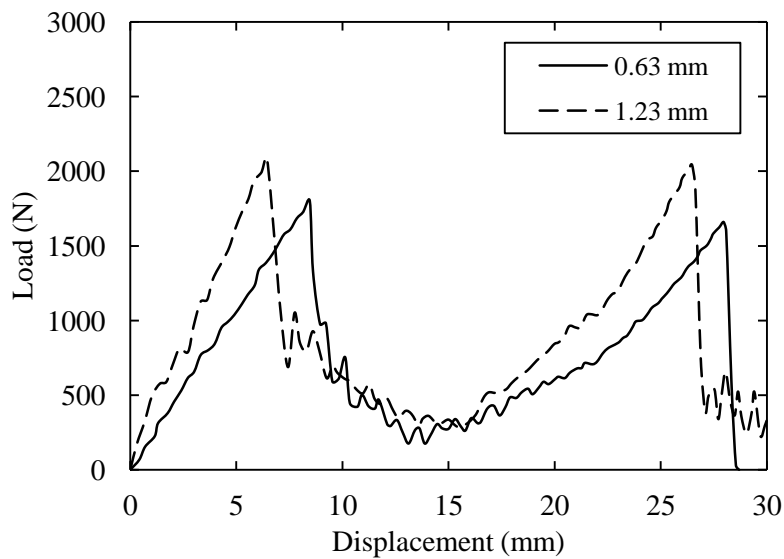


**Figure 5.32** Load-displacement traces following low velocity impact on the paperboard sandwich structures based on monolithic SRPP skins.

**Figure 5.33** summarises the perforation resistance of the PP honeycomb ( $40 \text{ kg/m}^3$ ) and the paperboard cores with monolithic SRPP skins thicknesses. From the figure, it can be seen that the PP honeycomb sandwich structures offer a markedly superior performance than the

paperboard core systems. For both panels, the perforation energy increases with increasing specimen thickness. Also included in the figure for comparison is the value for the GFRP/aluminium honeycomb sandwich panels.

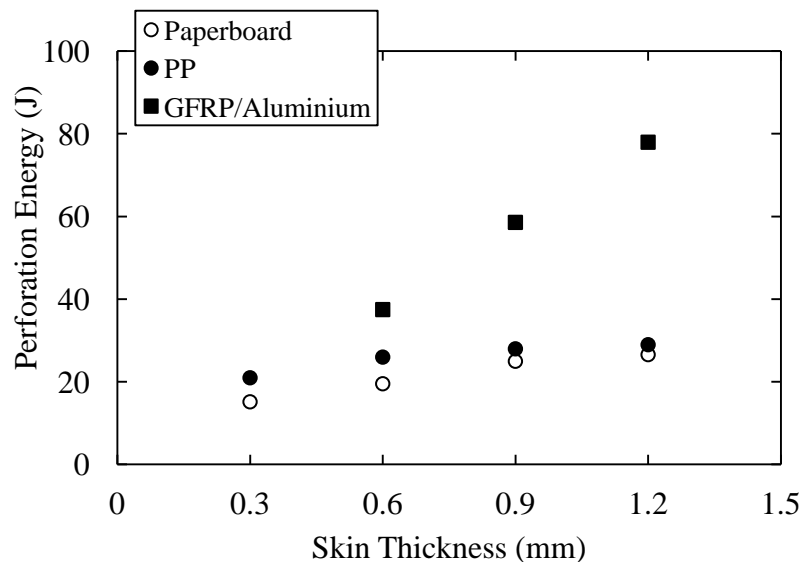


**Figure 5.33** The variation of perforation energy with skin thickness for PP honeycomb and paperboard sandwich structures based on monolithic skins. The figure includes the value for the aluminium sandwich structure.

**Figure 5.34(a)** shows a typical cross-section of the perforated surface of a PP honeycomb sandwich structure with a 0.93 mm thick monolithic SRPP skin. The uppermost skin has incurred the majority of the damage, which is localised to the area around the projectile. Again, damage in the core appears to extend some distance from the point of impact towards the edge of panel, suggesting that global deformation of the core occurred during impact, before penetration of the uppermost skin. Delamination is in evidence at the lowermost skin/core interface. Agarwall (8) reported that delamination has the ability to absorb a significant amount of energy during impact, being dependent on the bond strength between

the skin and core material. The progression of impact damage for the paperboard sandwich structure with a 0.93 mm monolithic SRPP skin can be seen in **Figure 5.34(b)**. Localised fibre breakage, with some fibre debonding and core crushing, are the primary failure mechanisms in the sample. In the lowermost skin, small amounts of the fibre breakage are in evidence around the perforation zone.

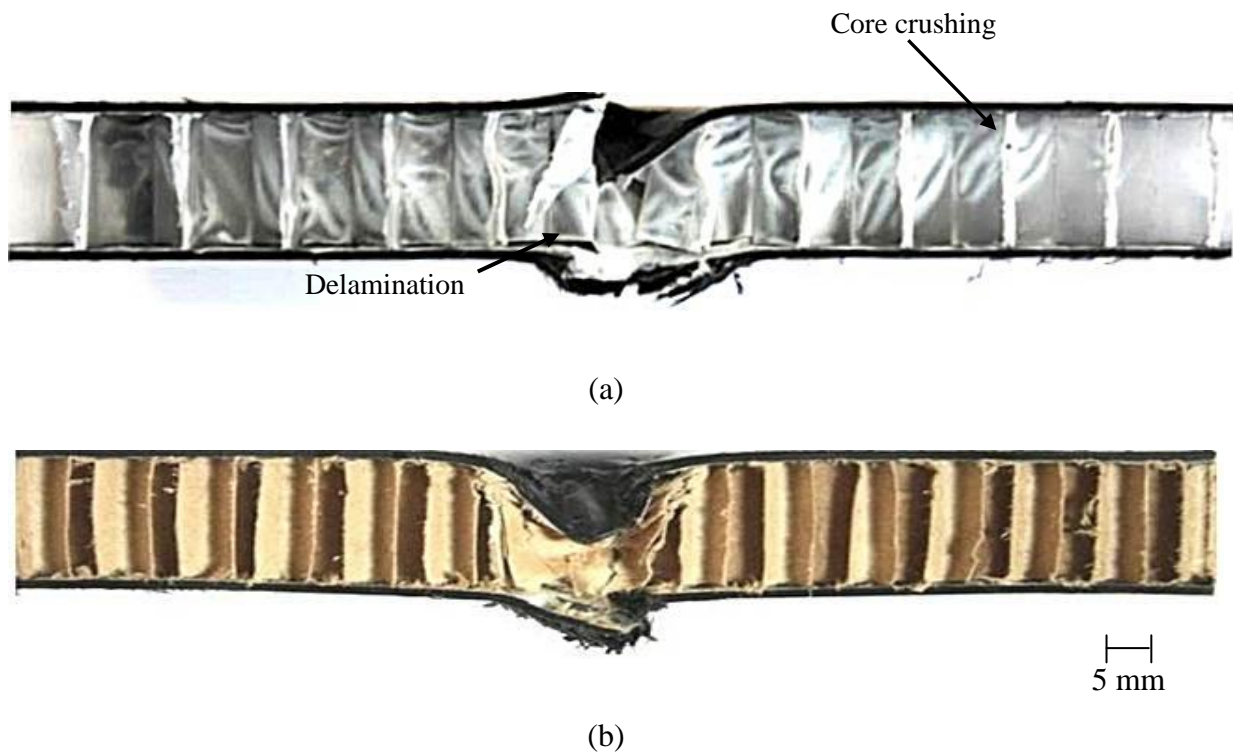


**Figure 5.34** Cross-sections of sandwich structures following impact on panels based on 0.93 mm monolithic SRPP skins with (a) a PP honeycomb and (b) a paperboard cores.



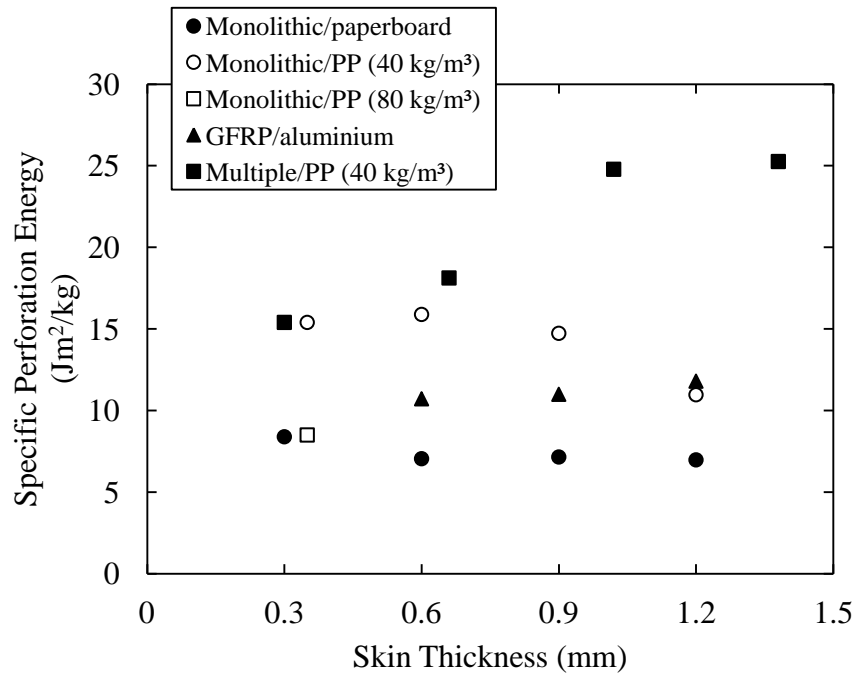


**Figure 5.35** Variation of the specific perforation energy with skin thickness for monolithic SRPP-(paperboard and PP honeycomb), multiple SRPP-PP honeycomb (40 and 80 kg/m<sup>3</sup>) and GFRP/aluminium honeycomb sandwich structures.

### 5.3.3 Specific Perforation Energy of Sandwich Structures

As the paperboard and aluminium honeycomb are significantly denser than the PP honeycomb, the specific perforation energy was employed as a key performance indicator. Here, the specific perforation energy was calculated by normalising the perforation energy by the areal density of the sandwich structure. The values of the specific perforation energy for five types of sandwich structures as a function of skin thickness is shown in **Figure 5.35**. As can be seen, the value of specific perforation energy for the monolithic SRPP-PP honeycomb and the paperboard sandwich structures decreases with increasing skin thickness. In addition, the value of the specific perforation energy of monolithic SRPP-PP honeycomb was slightly greater than that of the paperboard system. The figure also clearly shows that, for a given skin thickness, the multi-layer SRPP-PP honeycomb offers a far superior performance to those of

the other systems. It is interesting to note that the value of specific perforation energy of the multi-layer SRPP-PP honeycomb ( $80 \text{ kg/m}^3$ ) is similar to that of the multilayer SRPP-PP honeycomb ( $40 \text{ kg/m}^3$ ) system, **Figure 5.35**. When the data are presented in terms of perforation energy rather than specific perforation energy, the multilayer SRPP-PP honeycomb ( $80 \text{ kg/m}^3$ ) system continues to exhibit an excellent resistance to perforation, although the improvements relative to the other systems are somewhat reduced, due to the fact the multilayer SRPP-PP honeycomb ( $40 \text{ kg/m}^3$ ) offers a lower density. The GFRP/aluminium sandwich structure offers a lower value of specific perforation energy to the two comparable systems. The evidence in **Figure 5.35** suggests that multilayer SRPP-PP honeycomb offers significant potential for use in the design of impact resistant structures. In addition, the multilayer SRPP-PP honeycomb is a fully recyclable sandwich structure.

## 5.4 Conclusions

Quasi-static and impact tests on sandwich structures based on six different polymer foams have shown that properties of the core material have a significant influence on the indentation behaviour of a sandwich structure. It has been shown that a simple Meyer indentation law can be successfully employed to characterise the properties of the sandwich structure. The evident suggest that it is important that the correct contact properties are employed when modelling the impact response of sandwich structures. It has been shown that the indentation exponent of the polymer foams lies between 1.0 and 2.0 and does not show any significant dependency on many key impact parameters. In contrast, the contact stiffness,  $C$ , varies with strain rate and indenter radius and needs to be accurately determined prior to modelling.

The perforation resistance of sandwich structures based on nine different types of polymer foam has been investigated. Initially, the importance of the plastic collapse stress of the foam has been highlighted, with the maximum forces associated with fracture of the front and

rearmost plies being dependent on this parameter. Similarly, the average impact force between these peaks i.e. that associated with perforating the core has been shown to depend on the shear strength of the foam. Finally, a clear link between the perforation resistance of a foam-based sandwich panel and the Mode II work of fracture of the core has been established. It is suggested that the simple shear test outlined in this thesis can be used a simple means to benchmark the perforation behaviour of foam materials and their associated sandwich structures.

The low velocity impact properties of a range of all-polypropylene sandwich structures have been investigated. Particular attention has focused on assessing the influence of the design of the self-reinforced polypropylene skins on the perforation resistance of the sandwich plates. It has been shown that the use of multilayer SRPP skins, based on thin plies of composite bonded using a thin hot-melt thermoplastic interlayer, results in a significant improvement in the perforation resistance of the structure relative to similar panels constructed using monolithic skins. It is believed that the incorporation of multilayer skins facilitates significant interlaminar slip between the individual layers, a mechanism that absorbs significant energy during deformation of the target. In addition, separating the plies in this manner facilitates gross membrane stretching within the individual composite plies during the penetration process. Similar effects have been observed following drop-weight impact tests on plain all-polypropylene laminates, where the incorporation of a thin thermoplastic interlayer has been shown to greatly enhance the impact response of the laminates. Finally, the specific perforation energies of sandwich structures based on multi-layered skins has been shown to greatly exceed that associated with a GFRP/aluminium honeycomb system.

## 5.5 References

1. Reid SR, Wen HM. Perforation of FRP laminates and sandwich panels subjected to missile impact. *Impact behaviour of fibre-reinforced composite materials and structures*: Woodhead Publishing Limited, Cambridge; 2000. p. 239-78.
2. Chen SY, Farris TN, Chandrasekari S. Contact mechanics of Hertzian cone cracking. *International Journal of Solids and Structures*. 1995;32(3):329-40.
3. Hoo Fatt MS, Park KS. Dynamic models for low-velocity impact damage of composite sandwich panels–Part B: Damage initiation. *Composite Structures*. 2001;52(3):353-64.
4. Williamson JE, Lagace PA, editors. Response mechanisms in the impact of graphite/epoxy honeycomb sandwich panels. *Proceedings - American Society for Composites*, Technomic Publishing Ag, ISSN 1084-7243, ; 1993.
5. Zhou G, Hill M, Hookham N. Investigation of parameters governing the damage and energy absorption characteristics of honeycomb sandwich panels. *Journal of Sandwich Structures and Materials*. 2007;9(4):309-42.
6. Alcock B, Cabrera NO, Barkoula NM, Peijs T. Low velocity impact performance of recyclable all-polypropylene composites. *Composites Science and Technology*. 2006;66(11):1724-37.
7. Aurrekoetxea J, Sarrionandia M, Mateos M, Aretxabaleta L. Repeated low energy impact behaviour of self-reinforced polypropylene composites. *Polymer Testing*. 2011;30(2):216-21.
8. Agarwal BD, Broutman LJ, Chandrashekhara K. Analysis and performance of fiber composites: Wiley; 2006.
9. Akil Hazizan, The impact response of composite sandwich structures (Ph.D Thesis): The University of Liverpool; 2002.

10. Anderson T, Madenci E. Experimental investigation of low-velocity impact characteristics of sandwich composites. *Composite Structures*. 2000;50(3):239-47.

## **CHAPTER VI**

### **CONCLUSIONS**

---

The following section summarises the major findings of this research work. In addition, some recommendations for further work are suggested.

## 6.1 Mechanical Properties of Polymer Foams

This study presents a detailed investigation of the quasi-static and dynamic response of polymer foams under compression, Mode I and Mode II loading, in order to address the rate sensitivity of the foams. A number of conclusions can be drawn, as follows:

- From the compression tests on the polymer foam, it has been shown that the plastic collapse stress, steady state stress and densification stress are very sensitive to both foam density and strain-rate, tending to increase with increasing strain rate.
- A series of Mode I fracture tests, using the single-end notch bend specimen geometry, have shown that the work of fracture increases with foam density and decreases with strain-rate. In addition, the linear PVC foams have been shown to offer extremely high toughness characteristics
- From the Mode I fracture tests, loading at higher strain rates reduces local plasticity at the crack tip, leading to a lower toughness of the material.
- Simple test geometry has been developed to characterise the Mode II (shear) fracture toughness of the foams. It has been shown that the work of fracture in Mode II increases with foam density. Both linear and crosslinked PVC foams offer higher values of work of fracture than their PET counterparts.
- The work of fracture in shear is significantly higher than in tension. This is more pronounced in the crosslinked PVC systems. For example, it has been shown that for the Mode II values were up to thirty times higher than the corresponding Mode I data.

## 6.2 Indentation Behaviour of Foam-based Sandwich Structures

This part of the study investigated rate effects in the indentation behaviour of foam-based sandwich structures. A number of findings can be drawn as follows:

- Following a large number of indentation tests, the indentation exponent,  $n$ , in the Meyer law remains unchanged in passing from quasi-static to dynamic rates of loading. In contrast, the contact stiffness,  $C$ , increases significantly with strain-rate.
- In addition, the contact stiffness is directly related to the plastic collapse properties of the foam. A plot of the contact stiffness with plastic collapse strength yields a unique trace with both the quasi-static and dynamic data falling on one curve.
- Under dynamic conditions, the indentation exponent does not vary significantly with impact energy or with indenter diameter. In contrast, the contact stiffness increased with indenter diameter, with the relative increase depending on the stiffness of the foam core.
- The value of contact stiffness increases with the thickness of the skin. An increase in the thickness of the skin from 0.6 to 4.8 mm resulted in a 300 – 400 % increase in the indentation constant.
- Following indentation tests on the sandwich structures, it has been shown that the indentation exponent for a polymer foam lies between 1.0 and 1.2 and does not show any significant dependency on many contact key impact parameters. In contrast, the contact stiffness,  $C$ , varies with strain-rate, skin thickness and indenter radius. The findings of this study suggest that it is important to use the correct contact properties when modelling the impact response of sandwich structure.



### 6.3 Perforation Resistance of the Composite Structures

The perforation resistance of sandwich structures based of polymer composites has been investigated in detail. In this study, the relationship between perforation resistance and a series of mechanical tests have been undertaken to characterise the properties of the foams in compression, Mode I (opening) fracture and Mode II (shear). The following findings are made.

- Tests have shown that Mode II shear is an important energy-absorbing failure mode in perforated sandwich panels.
- The importance of the plastic collapse stress of the foam has been highlighted, with the maximum force associated with fracture of the front and rearmost plies being dependent on this parameter.
- Similarly, the average impact force between these peaks, i.e. that associated with perforating the core has been shown to depend on the shear strength of the foam. In addition, an examination of core damage of the sandwich structure highlighted the fact that the foam fails predominantly in a shear mode.
- Finally, a clear link between the perforation resistance of a foam-based sandwich panel and the Mode II work of fracture of the core has been established. It is suggested that the simple shear test outlined in this thesis can be used as a simple means to benchmark the perforation behaviour of foam materials and their associated sandwich structures.

Following this, perforation tests have been undertaken on fully-recyclable sandwich structures. The following conclusions can be drawn:

- Testing has shown that the multilayer SRPP-PP sandwich structures offered a superior perforation resistance to the solid laminate systems.
- An examination of the damage in the multilayer and solid laminates showed that fibre failure absorbs the greatest amount of energy during the perforation process. In contrast, delamination does not appear to be a significant energy-absorbing mechanism in these panels.
- The multilayer SRPP-PP laminates offered a greater energy-absorbing ability than the solid laminate plates, due to greater level of interlaminar shear in the PP interlayers.
- A comparison of the perforation response of the corrugated paperboard and PP honeycomb sandwich structures has shown that the latter offered a superior perforation resistance when the data are normalised by the specific perforation energy of the panel.

#### **6.4 Suggestions for Further Work**

Based on the conclusions made, above the following recommendations are drawn.

- The indentation and perforation resistance of sandwich structures should be investigated using finite element modelling.
- It would be interesting to study the perforation resistance of a graded foam in order to investigate the effect of impact on a variable stiffness core.
- It would be interesting to investigate the perforation resistance under high velocity impact loading.